Since 1955

Strojniški vestnik
Journal of Mechanical Engineering

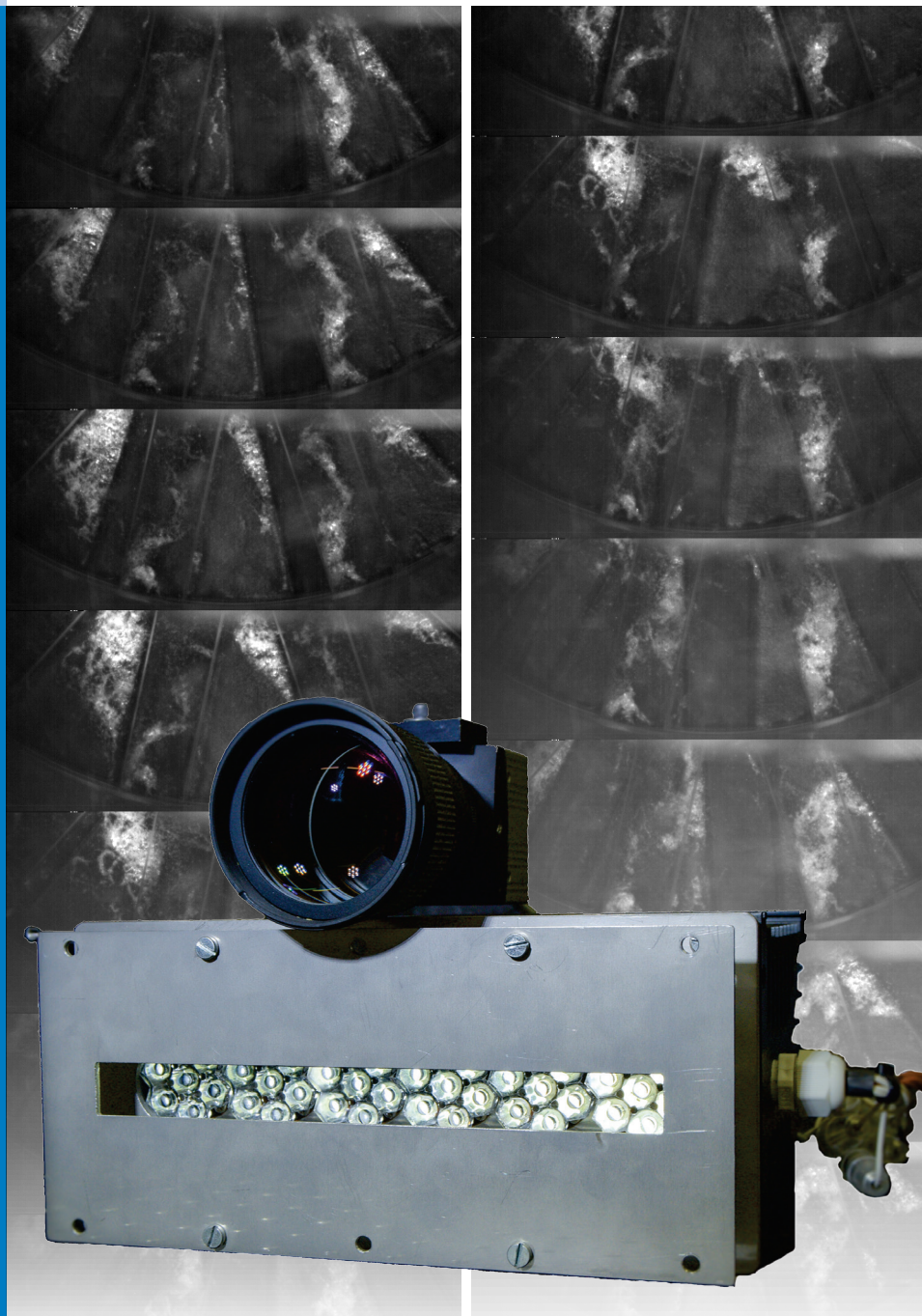

no. 2
year 2017
volume 63

Strojniški vestnik – Journal of Mechanical Engineering (SV-JME)

Aim and Scope
The international journal publishes original and (mini)review articles covering the concepts of materials science, mechanics, kinematics, thermodynamics, energy and environment, mechatronics and robotics, fluid mechanics, tribology, cybernetics, industrial engineering and structural analysis.
The journal follows new trends and progress proven practice in the mechanical engineering and also in the closely related sciences as are electrical, civil and process engineering, medicine, microbiology, ecology, agriculture, transport systems, aviation, and others, thus creating a unique forum for interdisciplinary or multidisciplinary dialogue.
The international conferences selected papers are welcome for publishing as a special issue of SV-JME with invited co-editor(s).

Editorial Office
University of Ljubljana, Faculty of Mechanical Engineering
SV-JME, Aškerčeva 6, SI-1000 Ljubljana, Slovenia
Phone: 386 (0)1 4771 137
Fax: 386 (0)1 2518 567
info@sv-jme.eu, http://www.sv-jme.eu

Print: Grafex, d.o.o., printed in 310 copies

Founders and Publishers
University of Ljubljana, Faculty of Mechanical Engineering, Slovenia
University of Maribor, Faculty of Mechanical Engineering, Slovenia
Association of Mechanical Engineers of Slovenia
Chamber of Commerce and Industry of Slovenia, Metal Processing Industry Association

President of Publishing Council
Branko Širok
University of Ljubljana, Faculty of Mechanical Engineering, Slovenia

Vice-President of Publishing Council
Jože Balič
University of Maribor, Faculty of Mechanical Engineering, Slovenia

Cover:
Image presents visualization setup for cavitation monitoring. High-speed camera Fastec with Samyang manual lense was used. In-house build LED setup provided the necessary illumination. The sequence of frames captured during the experiment is visible in the back. It shows how cavitation is generated on the fast rotating rotor. Cavitation is visible in white on black rotor background.

Image Courtesy:
Tadej Stepišnik Perdih, Laboratory for Water and Turbine Machines, Faculty of Mechanical Engineering, University of Ljubljana

ISSN 0039-2480

General information
Strojniški vestnik – Journal of Mechanical Engineering is published in 11 issues per year (July and August is a double issue).

Institutional prices include print & online access: institutional subscription price and foreign subscription €100,00 (the price of a single issue is €10,00); general public subscription and student subscription €50,00 (the price of a single issue is €5,00). Prices are exclusive of tax. Delivery is included in the price. The recipient is responsible for paying any import duties or taxes. Legal title passes to the customer on dispatch by our distributor.

Single issues from current and recent volumes are available at the current single-issue price. To order the journal, please complete the form on our website. For submissions, subscriptions and all other information please visit: *http://en.sv-jme.eu/.*

You can advertise on the inner and outer side of the back cover of the journal. The authors of the published papers are invited to send photos or pictures with short explanation for cover content.

We would like to thank the reviewers who have taken part in the peer-review process.

The journal is subsidized by Slovenian Research Agency.

Strojniški vestnik - Journal of Mechanical Engineering is available on http://www.sv-jme.eu, where you access also to papers' supplements, such as simulations, etc.

Contents

Strojniški vestnik - Journal of Mechanical Engineering
volume 63, (2017), number 2
Ljubljana, February 2017
ISSN 0039-2480

Published monthly

Papers

Strojniški vestnik - Journal of Mechanical Engineering 63(2017)2, 83-91

DOI:10.5545/sv-jme.2016.3970 Original Scientific Paper
Received for review: 2016-08-19
Received revised form: 2016-11-28
Accepted for publication: 2016-12-07

Influence of Hydrodynamic Cavitation on Intensification of Laundry Aqueous Detergent Solution Preparation

Tadej Stepišnik Perdih* – Brane Širok – Matevž Dular
University of Ljubljana, Faculty of Mechanical Engineering, Slovenia

Washing machines are one of the most energy and water demanding domestic appliances. Over years, a significant effort of the scientific community has been invested into making laundry more "sustainable". Nevertheless, the preparation of detergent solution has been entirely overlooked step of laundering. The preparation of aqueous detergent solutions in the currently available washing machines takes up to 10 minutes. In this work, we propose a design of a special rotary hydrodynamic cavitation generator, which would impact this process. New detergent dissolution rates have been experimentally tested on the laboratory model washing machine using the designed cavitation generator. The dissolution rates have been determined from the measurements of the undissolved detergent after the specific time of treatment. Additionally, the influence of hydrodynamic cavitation on that process has been isolated and investigated. To do so, two flow regimes have been established: the regime with cavitation present and the regime where cavitation was not present. In order to evaluate cavitational intensity, pressure oscillations inside cavitation generator have been recorded. Results indicate that cavitation significantly increases the detergent dissolution rates. In the cavitation flow regime, more than 80 % of the detergent is dissolved in approximately 10 seconds. With no cavitation present, about 150 seconds are needed to dissolve the same amount of the detergent. Intensification of the process can be attributed to mechanical effects of cavitation. This research shows that use of the cavitation generators in the washing machines could lead to shorter washing programs and henceforth potential water and energy savings.

Keywords: hydrodynamic cavitation, rotary cavitation generator, cavitational intensity, washing machines, aqueous detergent solution

Highlights

- *Hydrodynamic cavitation was used to prepare aqueous detergent solution.*
- *Special rotary hydrodynamic cavitation generator was designed.*
- *Cavitation significantly improves detergent dissolution rates.*
- *Cavitation generators could improve water and energy efficiency of washing machines.*

0 INTRODUCTION

Washing machines are among most common devices worldwide and at the same time one of biggest consumers of household energy [1]. One can assume that already a minor improvement in a laundry process or a washing machine production will have a globally non-negligible effect.

Many advances in laundry technology and washing machines design are already reported in the literature. Teschler suggests the use of a variable-speed inverter electromotor [2]. Ivarsson et al. proposed sensors for fill and rinse control [3], which would reduce water and detergent consumption. Most of the energy in washing machine is used for water heating, therefore Persson investigated the use of hot-water circulation loop [4]. Drinking water consumption could be significantly reduced with use of recycled water [5] or rainwater [6] and lastly, improved detergent composition would make laundry less of an environmental threat, while maintaining washing performance [7].

Surprisingly, preparation of wash bath (aqueous detergent solution) is completely neglected by researchers. Our team aims to intensify the preparation of wash bath by utilizing cavitation and to our knowledge, this is the first research where cavitation is used for detergent solutions preparation.

The use of cavitation is drawing great attention of researchers from various fields. Cavitation is a physical phenomenon characterized by formation, growth and subsequent collapse of bubbles in a bulk liquid. The collapses of bubbles create local "hot spots", releasing extreme amounts of energy [8]. If the bubble collapse occurs symmetrically, pressure shock waves are created, which propagate microscopic turbulence – a phenomenon known as microstreaming [9]. Moreover, when cavitation bubble is in a proximity of a solid surface, asymmetric bubble implosion takes place, which results in a formation of microjets [10]. These violent circumstances are being widely utilised to clean solid surfaces in different industries and medical and scientific laboratories for over 40 years [11] and [12]. On the other hand, the use of cavitation in textile engineering gained scientific attention only in recent years. Nevertheless, cavitation shows great potential for textile finishing and textile washing purposes. Vouters et al. [13] report, that with the use

*Corr. Author's Address: University of Ljubljana, Faculty of Mechanical Engineering, Aškerčeva 6, 1000 Ljubljana, Slovenia, tadej.stepisnik@fs.uni-lj.si

of cavitation, water consumption can be reduced by 20 % and energy consumption for 30 % with a rise of the quality of products by the same textile finishing treatment. In work of Gogate [14] one can additionally find an in-depth overview of other applications of cavitation phenomena for process intensification and reactor designs.

Cavitation is also recognised as an efficient method to prepare solutions and emulsions for various purposes. Depending on the application, either chemical effects (such as temperature and pressure hot spots, free radical formation) or mechanical effects (such as high shear stress and turbulence, microjets and microstreaming) are harnessed [15]. Kentish et al. [16] used cavitation to prepare range of food grade emulsions, Sivakumar et al. [17] proposed cavitation as green technology for preparation of poorly water-soluble drugs in pharmacy and Hasanbeigi and Price [18] investigated how use of cavitation can optimise costs and reduce pollution in production of dyeing solutions in textile industry. Additionally, Patil and Pandit [19] showed that cavitation is energy efficient method to produce nano-suspensions and Sharma et al. [20] was investigating operating parameters of cavitation setup on the intensification of hydrogenation reactions.

This paper is focused on basic research that aims to improve the efficiency of commercial washing machines by utilizing cavitation. More precisely, we have investigated the use of cavitation for aqueous detergent solution preparation in washing machines. Washing machines currently available on the market prepare the washing dissolution in the drum. Water from the supply network enters the machine and is led through the detergent tray to carry the detergent into the drum. There the detergent is mixed with clothes and the dissolution starts due to the rotation of the drum. The dissolution process consists of two steps: i) the interaction between the solute and the solvent molecules at the solid–liquid interface and ii) the diffusion of the solute molecules away from the interface to the bulk [21]. Since the dissolution is sequential it can take up to 10 minutes or even more, to prepare an adequate aqueous detergent solution in a washing machine. We assume this process would be accelerated if the detergent would be washed into a special bath, where it would be exposed to cavitation before it enters the drum. This could be a major improvement of washing machines operation by shortening laundry duration and potentially saving energy. Our goal was to determine to what extent hydrodynamic cavitation contributes to the dissolution time.

1 EXPERIMENTAL

The experiments were conducted at the University of Ljubljana in the Laboratory for Water and Turbine Machines. For this purpose, special rotary hydrodynamic cavitation generator (RHCG) has been designed. The detergent dissolution rates were experimentally evaluated, for both cavitation and non-cavitation flow regime, on a model washing machine. In addition, standardised tests with a magnetic stirrer were performed as a reference.

1.1 Set-Up and Materials

The experimental set-up (Fig. 1) was designed in a way to simulate an actual washing machine. Together with the rotary hydrodynamic cavitation generator, the experimental set-up consisted of a closed pressure tank, connection pipes and pressure (ABB 266 ast), flow (Bio-Tech: FCH-C-Ms-N) and temperature sensors (Fluke 51 II). Ports seen in Fig. 1 on the top of pressure vessel are used to fill the set-up with water and detergent. When operating, the mixture exits the vessel at the bottom, then it is led through RHCG, where it is exposed to cavitation. RHCG also serves as a pump. Water and detergent than flow through control valve and back to the pressure vessel. The RHCG was driven with a single-phase electromotor, which is already present in the most of the washing machines.

Two sets of experiments have been conducted – one with cavitation present and one in non-cavitating flow regime (this was achieved by increasing the system pressure while the rotational frequency and

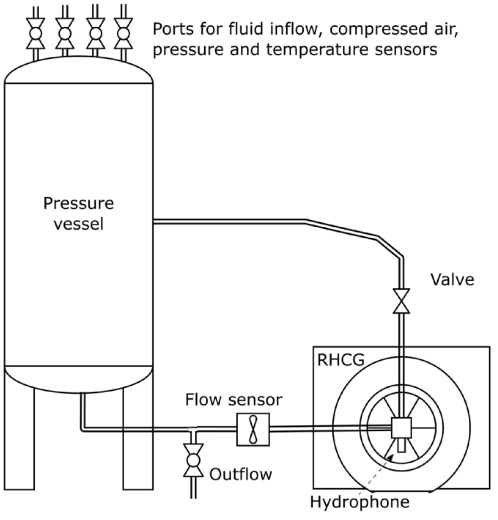

Fig. 1. *Experimental set-up*

the flow rate were not altered). The dissolution rate experiments have been performed in alignment to the standard IEC 60456: Clothes washing machines for household use – Methods for measuring the performance. The tank was filled with 2 litres of water at 23.5 °C. 11 grams of standard IEC-A detergent purchased from WFK Institute, Germany, was added to water and left to be treated by the generator for a specified time. The RHCG rotational speed was set to 7000 rpm, which established a flow rate of 11.3 l/min. In the cavitation regime, the tank was open to atmospheric pressure (101 kPa). In an actual washing machine with implemented RHCG, this regime would correspond to the washing machine operation. The non-cavitating flow regime was achieved by closing the tank air valves and raising the static pressure (in the tank) to 253 kPa. Operating conditions are collected in Table 1. We used same method as Biluš et al. [22] for cavitation monitoring. A high-speed camera (Fastec HiSpec4 2G mono) was used in order to monitor cavitation presence. To evaluate cavitation intensity, pressure oscillations were recorded using hydrophone Reson TC4014. After treating the sample for the specified time (between 10 and 300 seconds – from approximately 1 to 30 sample passages through the RHCG), the detergent solution was poured through the textile filter, so that the undissolved detergent remained on the filter. Filter textile (100 % cotton, swiss pique knit, yarn count 17 tex, double threaded) complied with the IEC 60456 standard requirements.

After the experiments, the filters were left to dry at ambient air for 24 h. The filters were weighed on the precision scale (Tehtnica Exacta EB 3600), prior and after the experiment and the percentage of detergent residues were recorded.

We achieved the following uncertainties of the measured values: ±1 % for the flow rate, ±0.5 % for the system pressure and ±0.8 % for the medium temperature. Mass of the detergent was measured to ±0.01 g and dynamic pressure oscillations to ±2.6 %.

1.2 Test Section – Rotary Hydrodynamic Cavitation Generator (RHCG)

The design of the rotary hydrodynamic cavitation generator follows the basic principles of high shear mixing devices [23], adjusted so that it also generates cavitation. The RHCG is an assembly of rotor and stator discs (Fig. 2) with special geometry inside the closed chamber. Both the rotor and the stator diameters have diameter 50 mm. They have 12 radial indentations, 3 mm deep (u) and 4 mm wide. Unindented area of the rotor disc has been machined in a way that the surfaces are angled at 8° (α), giving them a sharp edge. The stator surface has not been modified. The distance between the rotor and the stator was set to 1 mm (g). The whole assembly is illustrated in Fig. 3 and the details are given in Table 1.

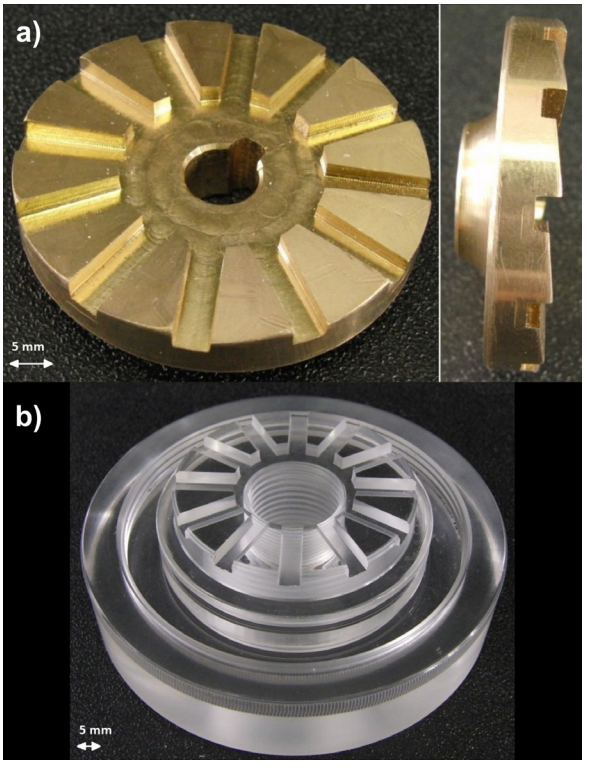

Fig. 2. *a) Rotor and b) the stator of cavitation generator*

Water and the detergent enter the RHCG in the axial direction through the stator. The RHCG operation causes periodically repeating pressure drops inside the chamber, due to relative movement of the two shear layers that form between the rotor and the stator. These conditions are favourable for hydrodynamic cavitation, hence before exiting in the radial direction, the mixture passes cavitation zones. Due to the rotation of the rotor, also centrifugal force is exerted on the fluid, which maintains the flow through the reactor. Because of that design, the cavitation generator can also replace a water recirculation pump in a washing machine.

Although acoustic cavitation is used in most of the aforementioned researches [13], [17], [18], [20], our device generates hydrodynamic cavitation. Its main advantages over acoustic cavitation are better potential for industrial and commercial scale applications, robust operation as well as improved energy efficiency [19] and [24] to [26]. In particular, the shear-induced

cavitation generated with our device has proven to be even more effective than hydrodynamic cavitation generated on Venturi section, as it was showed by Zupanc et al. [27].

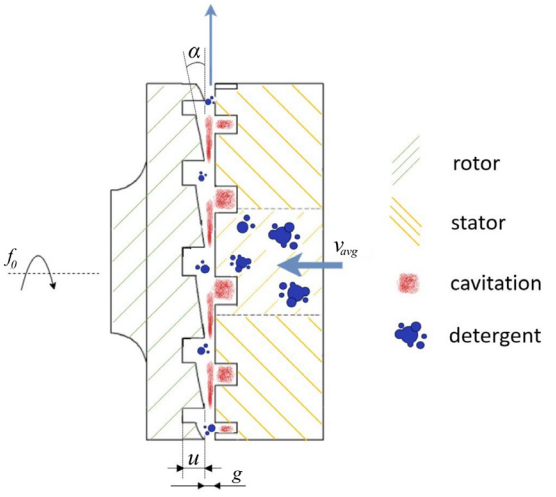

Fig. 3. *Scheme of the cavitation generator assembly; water and detergent enter the RHCG in the axial direction through the stator; before exiting in the radial direction, the mixture passes cavitation zones*

Table 1. *Operating conditions and cavitation generator geometry details*

Operating parameters	Cavitating regime	Non-cavitating regime
p [kPa]	101	253
g [mm]	1	
u [mm]	3	
α [°]	8	
f_0 [min^{-1}]	7000	

2 RESULTS

24 experiments in the RHCG were performed in order to determine the detergent dissolution rate - at cavitating (p = 1.01 bar) and non-cavitating (p = 2.53 bar) flow regimes, both at the rotating frequency of 7000 rpm (f_0). The lengths of exposure of the detergent to the RHCG were 10 s, 40 s, 70 s, 130 s and 300 s (this corresponds to approximately 1, 4, 7, 12 and 30 sample passages through the RHCG).

2.1 Cavitation Monitoring

Fig. 4 represents the sequences of images captured with the high-speed camera. In Fig. 4a, the RHCG front view is presented with indicated (the dashed rectangle) the high-speed camera observation window. Fig. 4b shows images of the cavitating regime with

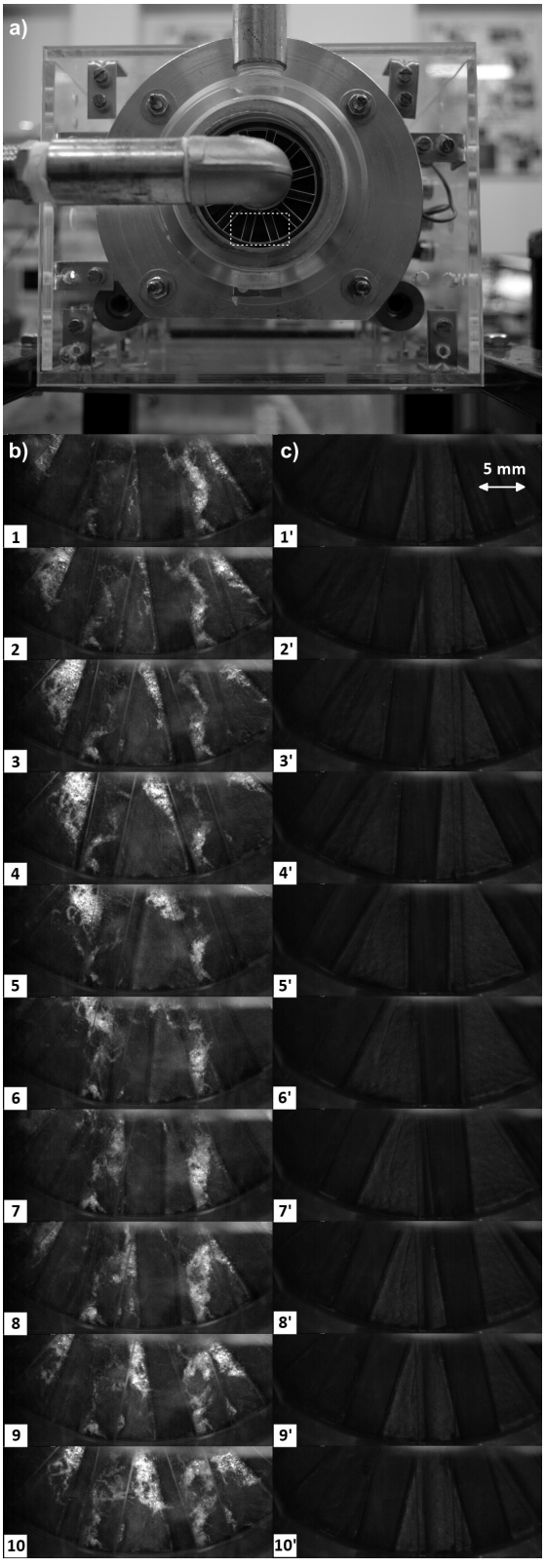

Fig. 4. *a) Top image shows RHCG frontal view with marked camera observation window; b) cavitating regime and c) the non-cavitating operation of the RHCG*

the system pressure 101 kPa. Fig. 4c was recorded at elevated pressure (253 kPa) and shows no presence of cavitation bubbles. The time difference between two frames is 0.1 ms.

At atmospheric pressure, cavitation, which is seen as white clouds, can be clearly distinguished from the black painted rotor. We can notice, that cavitation is generated in two regions: the attached cavitation on the sharp edge of the rotor and the cavitation in stator indentations. This means that the most of the fluid flow is uniformly exposed to cavitation. When the system pressure is raised to 253 kPa (Fig. 4b), no cavitation is present. The high-speed camera images confirm, that we have successfully established the two flow regimes (cavitating and non-cavitating one), by only changing the system pressure (the rotating frequency, the fluid temperature, the geometry and the flow rate were not altered) - this is important as we are not allowed to alter the rotating frequency of the rotor, to achieve comparable measurements.

The intensity of cavitation was evaluated by means of pressure oscillations. Bigger pressure amplitudes at bubble collapses represent higher cavitational intensity, **[12]**, **[15]** and **[22]**. Fig. 5 shows pressure evolution recorded with the hydrophone, which was mounted exactly between the rotor and the stator. One can see that both amplitudes and gradients are higher for the cavitating regime in comparison to the non-cavitating regime. This means that detergent is exposed to much higher stresses when cavitation is generated in RHCG.

2.2 Detergent Dissolution Rate

The results are shown in Fig. 6. Triangles mark results obtained under the cavitating regime and diamonds to the tests under the non-cavitating regime. For comparison also dissolution rates using magnetic stirrer were performed (circles in Fig. 6): the tests complied with the IEC-A detergent solubility test acquired from IEC 60456 standard. Power trend lines are added for easier interpretation.

As expected, the dissolution rate is significantly improved when the RHCG is used in comparison to the magnetic stirrer. For the case when the solution is prepared with the magnetic stirrer, more than 35 % of the detergent remains undissolved after 300 seconds of operation. In the same time, with using the RHCG in the non-cavitating regime, only about 15 % of the detergent remains undissolved. The amount of the undissolved detergent after 300 seconds of the RHCG operation in cavitation regime is less than 5 %.

The improved dissolution rate when using the RHCG can be attributed to intensified mixing. Similar to other rotating reactors used for mixing purposes **[23]** and **[28]** the RHCG operation establishes high

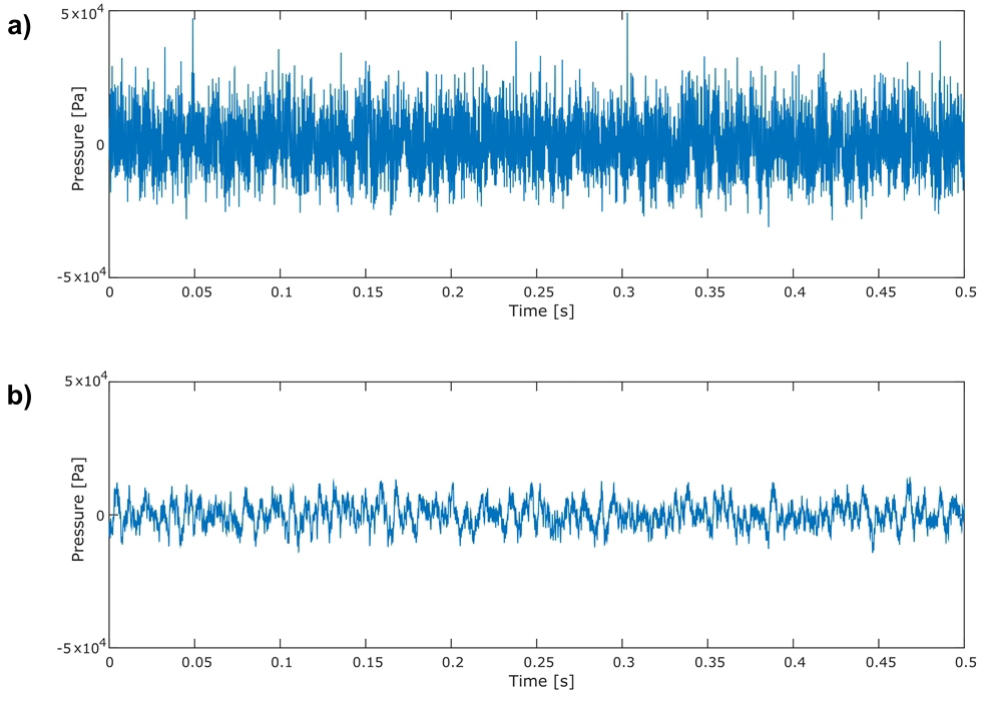

Fig. 5. *Pressure evolution in case of the a) cavitating regime and b) the non-cavitating regime*

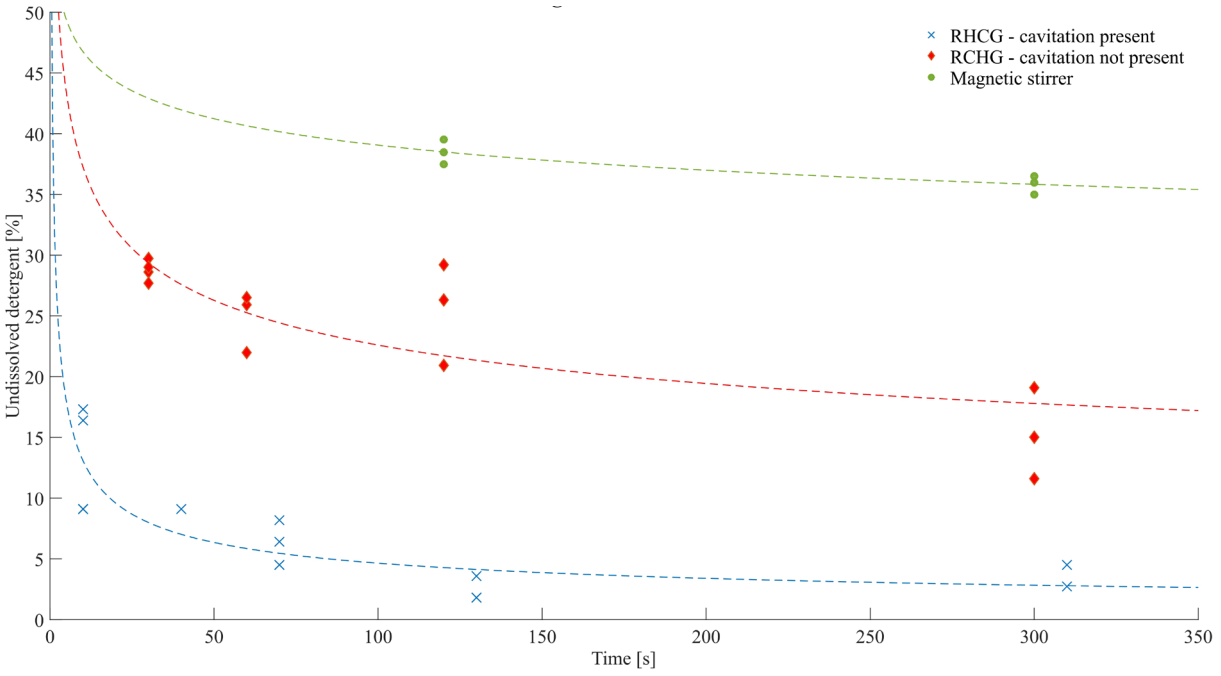

Fig. 6. *The measurements of the detergent dissolution rate; significant difference in the amount of undissolved detergent is observed between operation in cavitating regime versus non-cavitating and furthermore the measurements with magnetic stirrer according to IEC 60456 standard*

local turbulence levels inside the reactor chamber and enhances the solid-liquid mass transfer. This improves both steps of the dissolution process: the interactions between the solute (detergent) and the solvent (water) at the solid-liquid interface (first step), and especially the diffusion of the detergent to the bulk water (second step). Comparison of the results of the RHCG in cavitating and non-cavitating regimes furthermore indicates that cavitation has a substantial impact on the dissolution process. For objective assessment, ANOVA analysis of variance of the experiments was performed. The test confirms, that statistically significant difference with confidence level higher than 96 % exists between the cavitating and the non-cavitating regime ($\alpha < 0.04$).

Effect of cavitation on the dissolution process can be attributed to the violent collapses of cavitation bubbles. As evident from comparison of pressure evolution in Fig. 5, pressure pulsations in the cavitation regime increase for factor 2 in comparison to operation with no cavitation present. Henceforth high pressure pulsations and microjets due to cavitation [29] additionally increase the local turbulence and the detergent-water interaction and raising the dissolution rate. The difference in the amount of dissolved detergent is clearly demonstrated in Fig. 7. Images show two textile filters with detergent residues. The filter on the left belongs to the test where the detergent was exposed to the cavitation regime for 40 seconds, and the filter on the right corresponds to the test after the exposure to the non-cavitating regime for the same period of time (40 seconds).

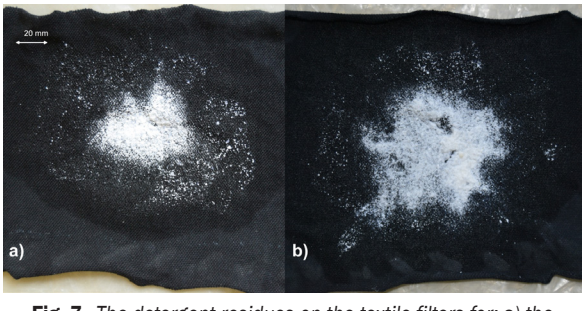

Fig. 7. *The detergent residues on the textile filters for: a) the cavitation regime with 1.0 g of the detergent remained on the filter and b) the non-cavitation regime with 3.2 g of the detergent remained on the filter*

The difference in dissolution rates is especially evident in the initial stages of experiments. With the cavitation regime, approximately 80 % of the detergent is dissolved within the first few seconds of the RHCG operation. When the RHCG operates at the same rotation frequency but without cavitation, 150 seconds are required to dissolve the same amount of

the detergent. The dissolution rates decrease with the passing time for both flow regimes. The trend can be described by a power law. A similar trend can also be recognised for dispersion kinetics of other dispersing machines such as a dissolver, a high-pressure homogenizer or a stirred media mill **[30]**. This is because the probability of successful solute-solvent interactions in the reactor is gradually decreasing.

3 CONCLUSIONS AND DISCUSSION

Our work indicates, that the rotary hydrodynamic cavitation generator substantially improves the preparation of the detergent washing dissolution and thus the washing machine performance. Implementation of such a device would shorten the washing program in general. In addition, the RHCG could tackle other identified issues related to detergent solution, such as: i) improved mixture homogeneity, which would result in improved washing effect and in decrease water consumption, ii) improved detergent solution rinsing, due to break up of detergent agglomerates - Sauter et al. **[31]** used cavitation for de-agglomeration of nanoparticles and Parivnzadeh et al. **[32]** studied cavitation assisted cotton processing with softener. They argued, that the reason for enhanced treatment is cavitation de-agglomeration of softener. We predict that cavitation has a similar effect to detergent agglomerates and therefore a lower volume of water is required to rinse smaller detergent particles.

Furthermore we assume that the implementation of the RHCG would have negligible if not beneficial effect on the energy consumption of the washing machines because: i) cavitation would assist the dissolution process and reduce the operating time for roughly 10 minutes, ii) the RHCG also operates as a pump and would replace the existing water circulation pump and iii) most of the energy required to generate cavitation is eventually transformed into heat, which, in case of washing machine, could be balanced by the reduction of the power consumption of electric water heaters.

In addition to the detergent solution preparation, the RHCG or similar cavitation generators, could enhance other aspects of a washing machine operation. One example is a washing performance. Several research groups worldwide are studying ultrasonic textile cleaning. Leading mechanism of ultrasonic cleaning is in fact acoustically generated cavitation. Gallego-Juarez et al. **[33]** developed semi-industrial system for textile washing in liquid layers, where Gotoh et al. **[34]** and Uzun and Patel **[35]** used ultrasonic cavitation bath. They achieved comparable or better washing results than the horizontal-axis washing machine, causing less damage to the textile.

Another important subject related to current development trends of laundering is microbial deactivation. High washing temperatures and aggressive detergents from the past are nowadays replaced by milder conditions: low temperatures and biodegradable detergents. Studies show, that various bacteria and fungi species are capable of surviving inside washing machines **[36]** and **[37]** under such circumstances. This could present a health risk **[36]**, or development of malodour **[37]**. Researchers will be forced to find solutions for those problems. One more time harnessing cavitation may bring desired results. Use of cavitation for pathogen deactivation **[38]** and **[39]** and wastewater treatment is well developed **[26]** and **[27]**.

Lastly, cavitation may have a potential to mitigate limescale. Limescale can cause serious issues to washing machine heat exchangers. Already a thin layer of scale reduces a heat exchanger efficiency and can lead to component failure. Review paper of Heath et al. **[40]** shows that cavitation/scale interaction is complex, but a lot of effort is invested in its research.

In previous paragraphs, we pointed out what aspects of washing machines may be improved with cavitation in addition to wash bath preparation. Extensive research is still needed in order to determine if also RHCG, or any other small scale cavitation generator, can achieve such results. However, use of cavitation may be the answer for sustainable and effective laundry.

4 ACKNOWLEDGEMENTS

The authors gratefully acknowledge the support by Slovenian Research Agency.

5 REFERENCES

[1] Bansal, P., Vineyard, E., Abdelaziz, O. (2011). Advances in household appliances – a review. *Applied Thermal Engineering*, vol. 31, no. 17-18, p. 3748-3760, **DOI:10.1016/j.applthermaleng.2011.07.023**.

[2] Teschler, L. (2008). Motors move toward more efficiency, *Machine Design*, vol. 7, p. 74-78.

[3] Ivarsson, P., Johansson, M., Höjer, N.E., Krantz-Rülcker, C., Winquist, F., Lundström, I. (2005). Supervision of rinses in a washing machine by a voltammetric electronic tongue. *Sensors and Actuators B: Chemical*, vol. 108, no. 1-2, p. 851-857, **DOI:10.1016/j.snb.2004.12.088**.

[4] Persson, T. (2007). Dishwasher and washing machine heated by a hot water circulation loop. *Applied Thermal*

Engineering, vol. 27, no. 1, p. 120-128, **DOI:10.1016/j.applthermaleng.2006.05.005**.

[5] Chen, Z., Ngo, H.H., Guo, W.S., Listowski, A., O'Halloran, K., Thompson, M., Muthukaruppan, M. (2012). Multi-criteria analysis towards the new end use of recycled water for household laundry: A case study in Sydney. *Science of the Total Environment*, vol. 438, p. 59-65, **DOI:10.1016/j.scitotenv.2012.08.019**.

[6] Morales-Pinzón, T., Lurue-a, R., Gabarrell, X., Gasol, C.M., Rieradevall, J. (2014). Financial and environmental modelling of water hardness - Implications for utilising harvested rainwater in washing machines. *Science of the Total Environment*, vol. 470-471, p. 1257-1271, **DOI:10.1016/j.scitotenv.2013.10.101**.

[7] Vojcic, L., Pitzler, C., Körfer, G., Jakob, F., Ronny, M., Maurer, K.H., Schwaneberg, U. (2015). Advances in protease engineering for laundry detergents. *New Biotechnology*, vol. 32, no, 6, p. 629-6346, **DOI:10.1016/j.nbt.2014.12.010**.

[8] Suslick, K.S., Eddingaas, N.C., Flannigan, D.J., Hopkins, S.D., Xu, H. (2011). Extreme conditions during multibubble cavitation: Sonoluminescence as a spectroscopic probe. *Ultrasonics Sonochemistry*, vol. 18, no. 4, p. 842-846, **DOI:10.1016/j.ultsonch.2010.12.012**.

[9] Davidson, B.J., Riley, N. (1971). Cavitation microstreaming. *Journal of Sound and Vibration*, vol. 15, p. 217-233, **DOI:10.1016/0022-460X(71)90536-0**.

[10] Gogate, P.R., Pandit, A.B. (2000). Engineering design methods for cavitation reactors II: Hydrodynamic cavitation. AIChE Journal, vol. 46, no. 8, p. 1641-1649, **DOI:10.1002/aic.690460815**.

[11] Mason, T.J. (2016). Ultrasonic cleaning: An historical perspective. *Ultrasonics Sonochemistry*, vol. 29, p. 519-523, **DOI:10.1016/j.ultsonch.2015.05.004**.

[12] Verhaagen, B., Fernández Rivas, D. (2016). Measuring cavitation and its cleaning effect. *Ultrasonics Sonochemistry*, vol. 29, p. 619-628, **DOI:10.1016/j.ultsonch.2015.03.009**.

[13] Vouters, M., Rumeau, P., Tierce, P., Costes, S. (2004). Ultrasounds: an industrial solution to optimise costs, environmental requests and quality for textile finishing. *Ultrasonics Sonochemistry,* vol. 11, no. 1, p. 33-38, **DOI:10.1016/S1350-4177(03)00113-5**.

[14] Gogate, P.R. (2008). Cavitational reactors for process intensification of chemical processing applications: A critical review. Chemical Engineering and Processing: *Process Intensification*, vol. 47, no. 4, p. 515-527, **DOI:10.1016/j.cep.2007.09.014**.

[15] Gogate, P.R., Sutkar, V.S., Pandit, A.B. (2011). Sonochemical reactors: Important design and scale up considerations with a special emphasis on heterogeneous systems. *Chemical Engineering Journal*, vol. 166, no. 3, p. 1066-1082, **DOI:10.1016/j.cej.2010.11.069**.

[16] Kentish, S., Wooster, T.J., Ashokkumar, M., Balachandran, S., Mawson, R., Simons, L. (2008). The use of ultrasonics for nanoemulsion preparation. *Innovative Food Science and Emerging Technologies*, vol. 9, no. 2, p. 170-175, **DOI:10.1016/j.ifset.2007.07.005**.

[17] Sivakumar, M., Tang, S.Y., Tan, K.W. (2014). Cavitation technology - a greener processing technique for the generation of pharmaceutical nanoemulsions. *Ultrasonics Sonochemistry*, vol. 21, no. 6, p. 2069-2083, **DOI:10.1016/j.ultsonch.2014.03.025**.

[18] Hasanbeigi, A., Price, L. (2015). A technical review of emerging technologies for energy and water efficiency and pollution reduction in the textile industry. *Journal of Cleaner Production,* vol. 95, p. 30-44, **DOI:10.1016/j.jclepro.2015.02.079**.

[19] Patil, M.N., Pandit, A.B. (2007). Cavitation - A novel technique for making stable nano-suspensions. Ultrasonics *Sonochemistry*, vol. 14, no. 15, p. 519-530, **DOI:10.1016/j.ultsonch.2006.10.007**.

[20] Sharma, A., Bapat, P.S., Gogate, P.R., Gastgar, S.N., Pandit, A.B. (2009). Process intensification of hydrogenation reactions using cavitation: Modelling the effect of solvent and catalyst. Chemical Engineering and Processing: *Process Intensification*, vol. 48, no. 1, p. 432-437, **DOI:10.1016/j.cep.2008.05.008**.

[21] Allaboun, H., Alkhamis, K.A., Al Jbour, N.D. (2007). Effect of surfactant on dissolution of spherical particles in micellar systems. *European Journal of Pharmaceutics and Biopharmaceutics*, vol. 65, no. 2, p. 188-197, **DOI:10.1016/j.ejpb.2006.07.017**.

[22] Biluš, I., Bombek, G., Hočevar, M., Širok, B., Cencič, T., Petkovšek, M. (2014). The experimental analysis of cavitationg structure fluctuations and pressure pulsations in the cavitation station. *Strojniški vestnik - Journal of Mechanical Engineering,* vol. 60, no. 3, p. 147-157, **DOI:10.5545/sv-jme.2013.1462**.

[23] Zhang, J., Xu, S., Li, W. (2012). High shear mixers: A review of typical applications and studies on power draw, flow pattern, energy dissipation and transfer properties. *Chemical Engineering and Processing: Process Intensification*, vol. 57-58, p. 25-41, **DOI:10.1016/j.cep.2012.04.004**.

[24] Arrojo, S., Benito, Y. (2008). A theoretical study of hydrodynamic cavitation. *Ultrasonics Sonochemistry*, vol. 15, no. 3, p. 203-211, **DOI:10.1016/j.ultsonch.2007.03.007**.

[25] Bagal, M.V., Gogate, P.R. (2014). Wastewater treatment using hybrid treatment schemes based on cavitation and Fenton chemistry: A review. *Ultrasonics Sonochemistry*, vol. 21, no. 1, p. 1-14, **DOI:10.1016/j.ultsonch.2013.07.009**.

[26] Sivakumar, M., Pandit, A.B. (2002). Wastewater treatment: A novel energy efficient hydrodynamic cavitational technique. *Ultrasonics Sonochemistry*, vol. 9, no. 3, p. 123-131, **DOI:10.1016/S1350-4177(01)00122-5**.

[27] Zupanc, M., Kosjek, T., Petkovšek, M., Dular, M., Kompare, B., Širok, B., Stražar, M., Heath, E. (2014). Shear-induced hydrodynamic cavitation as a tool for pharmaceutical micropollutants removal from urban wastewater. *Ultrasonics Sonochemistry*, vol. 21, no. 3, p. 1213-1221, **DOI:10.1016/j.ultsonch.2013.10.025**.

[28] Visscher, F., van der Schaaf, J., Nijhuis, T.A., Schouten, J.C. (2013). Rotating reactors - A review. *Chemical Engineering Research and Design*, vol. 91, no. 10, p. 1923-1940, **DOI:10.1016/j.cherd.2013.07.021**.

[29] Dular, M., Bachert, B., Stoffel, B., Širok, B. (2004). Relationship between cavitation structures and cavitation damage. *Wear*, vol. 257, no. 11, p. 1176-1184, **DOI:10.1016/j.wear.2004.08.004**.

[30] Schilde, C., Kampen, I., Kwade, A. (2010). Dispersion kinetics of nano-sized particles for different dispersing machines.

Chemical Engineering Science, vol. 65, no. 11, p. 3518-3527, **DOI:10.1016/j.ces.2010.02.043**.

[31] Sauter, C., Emin, M.A., Schuchmann, H.P., Tavman, S. (2008). Influence of hydrostatic pressure and sound amplitude on the ultrasound induced dispersion and de-agglomeration of nanoparticles. *Ultrasonics Sonochemistry*, vol. 15, no. 4, p. 517-523, **DOI:10.1016/j.ultsonch.2007.08.010**.

[32] Parvinzadeh, M., Memari, N., Shaver, M., Katozian, B., Ahmadi, S., Ziadi, I. (2010). Influence of ultrasonic waves on the processing of cotton with cationic softener. *Journal of Surfactants and Detergents*, vol. 13, no. 2, p. 135-141, **DOI:10.1007/s11743-009-1158-y**.

[33] Gallego-Juarez, J.A., Riera, E., Acosta, V., Rodríguez, G., Blanco, A. (2010). Ultrasonic system for continuous washing of textiles in liquid layers. *Ultrasonics Sonochemistry*, vol. 17, no. 1, p. 234-238, **DOI:10.1016/j.ultsonch.2009.06.005**.

[34] Gotoh, K., Harayama, K., Handa, K. (2015). Combination effect of ultrasound and shake as a mechanical action for textile cleaning. *Ultrasonics Sonochemistry*, vol. 22, p. 412–421, **DOI:10.1016/j.ultsonch.2014.05.005**.

[35] Uzun, M., Patel, I. (2010). Mechanical properties of ultrasonic washed organic and traditional cotton yarns. *Journal of Achievements in Materials and Manufacturing Engineering*, vol. 43, no. 2, p. 608-612.

[36] Novak Babič, M., Zalar, P., Ženko, B., Schroers, H.J., Džeroski, S., Gunde-Cimerman, N. (2015). Candida and Fusarium species known as opportunistic human pathogens from customer-accessible parts of residential washing machines. *Fungal Biology*, vol. 119, no. 2-3, p. 95-113, **DOI:10.1016/j.funbio.2014.10.007**.

[37] Munk, S., Johansen, C., Stahnke, L.H., Adler-Nissen, J. (2001). Microbial survival and odor in laundry. *Journal of Surfactants and Detergents*, vol. 4, no. 4, p. 385-394, **DOI:10.1007/s11743-001-0192-2**.

[38] Yusof, N.S.M., Babgi, B., Alghamdi, Y., Aksu, M., Madhavan, J., Ashokkumar, M. (2016). Physical and chemical effects of acoustic cavitation in selected ultrasonic cleaning applications. *Ultrasonics Sonochemistry*, vol. 29, p. 568-576, **DOI:10.1016/j.ultsonch.2015.06.013**.

[39] Šarc, A., Oder, M., Dular, M. (2014). Can rapid pressure decrease induced by supercavitation efficiently eradicate Legionella pneumophilabacteria?. *Desalination and Water Treatment*, vol. 57, no. 5, p. 2184-2194, **DOI:10.1080/19443994.2014.979240**.

[40] Heath, D., Širok, B., Hočevar, M., Širok, B., Pečnik, B. (2013). The use of the cavitation effect in the mitigation of CaCO3 deposits. *Strojniški vestnik - Journal of Mechanical Engineering*, vol. 59, no. 4, p. 203-215, **DOI:10.5545/sv-jme.2012.732**.

Strojniški vestnik - Journal of Mechanical Engineering 63(2017)2, 92-102
DOI:10.5545/sv-jme.2016.3563
Original Scientific Paper
Received for review: 2016-03-10
Received revised form: 2016-11-21
Accepted for publication: 2016-12-16

Effects of Nozzle Inner Surface Roughness on the Performance of Self-Resonating Cavitating Waterjets under Different Ambient Pressures

Deng Li[1,2,3] – Yong Kang[1,2,*] – Xiaolong Ding[1,2] – Xiaochuan Wang[1,2] – Zhenlong Fang[1,2]

[1] Wuhan University, School of Power and Mechanical Engineering, China
[2] Wuhan University, Hubei Key Laboratory of Waterjet Theory and New Technology, China
[3] University of Illinois at Urbana-Champaign, Department of Mechanical Science and Engineering, United States

The self-resonating cavitating waterjet (SRCW) has been widely used for many practical and industrial applications since the first recognition of its strong cavitation ability. To further improve the performance of SRCW under ambient pressures, the effects of nozzle inner surface roughness were experimentally studied by impinging the jets on pure aluminium specimens (1070A) at various standoff distances. The typical macroscopic appearances and mass losses of the eroded specimens were used to evaluate the performances of the jets issuing from six organ-pipe nozzles of different inner surface roughness values (0.8 μm, 1.6 μm, 3.2 μm, 6.3 μm, 12.5 μm, and 25 μm). The results show that nozzle inner surface roughness significantly influences the optimum standoff distance and the cavitation intensity, which greatly depends on the ambient pressure. Moreover, it is found that there is always an optimum surface roughness that can remarkably enhance the cavitation erosion capability under each ambient pressure. Specifically, at ambient pressures of 2 MPa and 4 MPa, the surface roughness of 6.3 μm causes the strongest cavitation intensity at standoff distances of 42 mm and 50 mm, respectively. While at ambient pressures of 6 MPa, 8 MPa, and 10 MPa, the surface roughness of 12.5 μm is the one that maximally enhances the intensity at standoff distances of 45 mm, 40 mm, and 35 mm, respectively. Furthermore, the enhanced cavitation intensity is found to improve the impingement power of the high-speed waterjet as well. The present study also helps to provide a guideline for determining the finishing accuracy of inner surface required in the fabrication of organ-pipe nozzles.

Keywords: self-resonating cavitating waterjet, surface roughness, cavitation erosion, ambient pressure, organ-pipe nozzle

Highlights

- *Erosion tests under ambient pressures were performed to study the effects of nozzle inner surface roughness on cavitation.*
- *The macroscopic appearances and mass losses of eroded specimens were analysed.*
- *Nozzle inner surface roughness affects the optimum standoff distance and the impingement power of the jet.*
- *There is a preferred nozzle inner surface roughness value under each ambient pressure.*

0 INTRODUCTION

Cavitation is the formation of vapor bubbles in a liquid and happens when the local pressure is lower than the vapor pressure of the liquid [1]. It can be easily generated with high-speed waterjets. The collapse of cavitation bubbles near a solid boundary can cause very high amplitude and small duration impulsive loads and emits a large amplitude pressure wave, which subsequently leads to serious local damage [2]. Based on this feature, cavitating waterjet, which can be produced by creating a large number of bubbles in the periphery of the jet, has been proposed and is now being used in a wide spectrum of applications, such as cavitation peening, removal coating [3], cleaning [4], cutting [5], deep-hole drilling [6], and killing bacteria [7].

To enhance the cavitation intensity of the cavitating waterjet for better utilization, a considerable number of investigations related to the mechanism of cavitation and methods for promoting it have been conducted. In more specific terms, Biluš et al. [8] performed an experimental analysis of the structure dynamics of cavitation cloud and corresponding pressure fluctuations. They concluded that there is a strong interaction between pressure and cavitation cloud with two dominant frequency bands. Soyama [9] experimentally studied the effect of various types of nozzle geometries on the aggressive intensity of cavitation erosion. Based on a control volume concept, Zhou et al. [10] developed a novel lumped parameter model of cavitating orifice flow by using the computational fluid dynamic method. Furthermore, several self-resonating cavitating nozzles, named "Pulser", "Pulser-Fed", "Laid-back Pulser", and "Organ-pipe", have been proposed and investigated by Johnson et al. [11]. Waterjets issuing from these nozzles have large-scale coherent structures and vortex rings in the shear layer, which can dramatically increase the cavitation intensity.

A schematic diagram of the generation and working principles of SRCW is shown in Fig. 1 with the use of an organ-pipe nozzle, which is one of the

*Corr. Author's Address: Wuhan University, School of Power and Mechanical Engineering, Wuhan, China, kangyong@whu.edu.cn

most promising nozzles in applications due to its simple structure and strong cavitation ability [12].

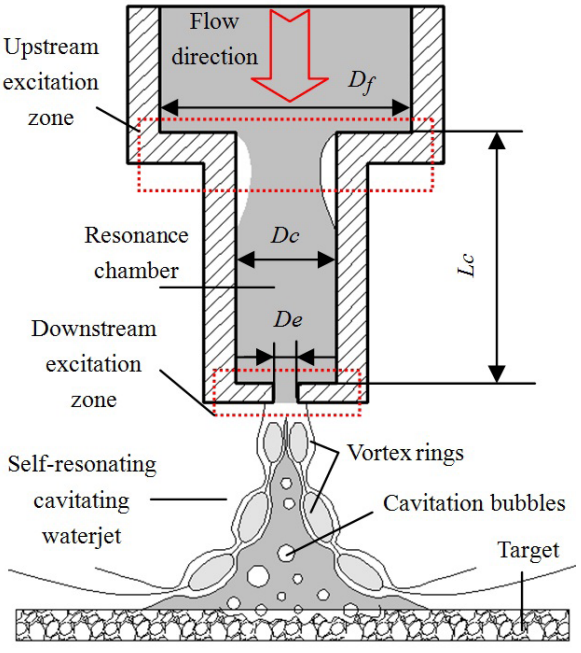

Fig. 1. *Schematic diagram of the operating principles of an SRCW issuing from an organ-pipe nozzle*

As is shown in the figure, an organ-pipe nozzle consists of an upstream area contraction (D_f/D_c), a downstream area contraction (D_c/D_e), and a resonant chamber with a length of L_c and a diameter of D_c. When a high-speed flow is passing through the nozzle, pressure waves will be formed at the downstream area contraction because of the sudden changes of the flow velocity. These waves propagate upwards and then are reflected at the upstream contraction due to the change of impedance. At this time, the upstream and downstream contractions are excitation zones, which are the geometrical foundation for producing SRCWs. Then, the incident waves are superimposed on the reflected waves, and an acoustic resonance will finally be formed if the length of the chamber is designed to shape a standing wave [11] to [14]. The peak resonance can be achieved by matching the fundamental frequency of the organ-pipe nozzle with the critical jet structuring frequency. Moreover, the exact frequency of peak resonance depends on the end impedances; for instance, if both $(D_f/D_c)^2$ and $(D_c/D_e)^2$ are large, the first model natural frequency of the chamber will occur when the wavelength in the fluid is approximately four times the chamber length L_c [13].

When an SRCW is produced, the energy content of the jet can be dramatically amplified, because the shear layer of the jet can be organized into large ring vortices emitted from the nozzle at a discrete frequency and could cavitate to form toroidal bubbles [14]. The formation, growth, and collapse of these bubbles could cause very high-pressure fluctuations that can be further enhanced by the self-resonance to several orders of magnitude higher, resulting in the greatly improved cavitation erosion capability of the jet [15]. These features make SRCWs especially suitable for deep-hole drilling, where high ambient pressures can prevent the formation of cavitation bubbles in conventional cavitating jets because of the low incipient cavitation numbers [16]. Furthermore, it has already been proven that SRCW has stronger cavitation erosion ability at relatively greater ambient pressures. To be more specific, Johnson et al. [17] experimentally claimed that the incipient cavitation numbers for SRCWs were generally two to six times higher than conventional cavitating waterjets under the same ambient pressure. Results of field trials conducted by Li et al. [18] revealed that the drilling rate in deep oil wells of high ambient pressures could be considerably improved from 10.1% to 31.5% with the use of SRCWs.

Even though SRCW has many advantages over conventional cavitating jets under ambient pressure conditions, to the best of our knowledge, few investigations have been performed to understand the influence of nozzle inner surface roughness on the cavitation erosion capabilities of the jets. However, nozzle inner surface roughness is expected to affect the cavitation characteristics significantly. Based on a numerical investigation on the effects of wall roughness on cavitating flow, Echouchene et al. [19] concluded that wall roughness leads to higher shear stresses in the liquid and produces additional disturbance of the velocity and pressure. In addition, Chang et al. [20] experimentally found that the nozzle inlet surface roughness can affect the occurrence of cavitation much more than it affects hydraulic flip. Most importantly, in our most recent studies [21] and [22], it has been shown that the nozzle inner surface roughness can have dramatic effects on the axial pressure oscillations as well as the cavitation erosion intensity and efficiency of SRCW.

As the strong cavitation ability under ambient pressures is one of the greatest advantages of SRCW, the purpose of this study is to further improve the aggressive intensity of cavitation erosion by investigating the effects of nozzle inner surface roughness.

1 RELATIONS BETWEEN SURFACE ROUGHNESS, TURBULENT FLOW, AND CAVITATION

Turbulent flow occurs when the ratio of inertial force to viscous force exceeds a critical value, and its intensity can be measured by the Reynolds number (*Re*). In a turbulent flow, the violent and unsteady motions of the fluid particles make the flow highly irregular, which produces large pressure fluctuations in the fluid. When the local pressure drops below the vapor pressure, cavitation occurs and then disordered, and unstable eddies are formed in the fluid. The formed vortices have a tendency of pairing into vortex rings of many different length scales, which greatly impacts the flow behaviours, including energy dissipation and pressure pulsations [23].

Fig. 2 illustrates the structure of a fully turbulent viscous flow passing through a circular pipe of the rough inner surface. As shown in the figure, the flow structure can be divided into viscous sublayer region and turbulent core region. Though the thickness of the viscous sublayer is rather small (about 10 % of the boundary layer thickness), the viscous shear force in the layer plays a significant role on the turbulence properties, such as the convective heat transfer, momentum and mass exchange, and energy diffusion [24]. If the viscous sublayer is affected, cavitation, which is closely related to the turbulent characteristics, will be influenced as a result.

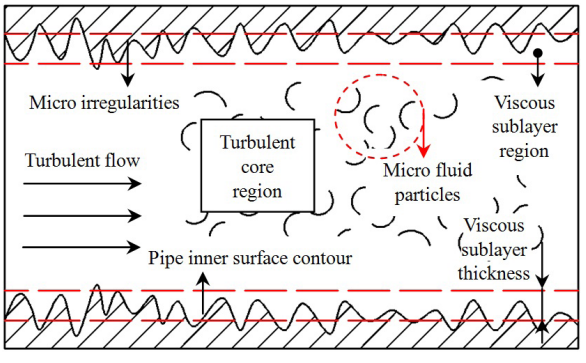

Fig. 2. *Schematic of flow structure of turbulent flow over rough surface*

Because of the practical limitations on surface machining, the inner surface of the nozzle is not ideally smooth but has enormous amounts of micro-irregularities called roughness elements. If the magnitude of roughness element height is similar to the viscous sublayer thickness, violent interactions between the roughness elements and the viscous sublayer will happen and thus significantly influence the turbulent flow. Based on the relations between turbulence and cavitation mentioned above, it can be deduced that once the turbulent flow is affected, the cavitation process will be influenced as well. This assumption is in accordance with one of the studies on the influence of surface roughness on turbulent flow, carried out by Nikuradse [25]. He demonstrated that the velocity distribution of the turbulent flow was dramatically dependent on the relative roughness. By means of experimental investigation, Li et al. [26] found that when the roughness height is more than five times the viscous sublayer thickness, the flow friction, which can cause large pressure drops in the fluid, begins to increase sharply. In contrast, when a high-speed liquid is flowing over the roughness elements, fluid separation tends to occur, which will promote the generation of cavities and thus the cavitation erosion intensity.

A preliminary calculation (detail is shown in Section 3.2) has shown that the most commonly used surface roughness values (0.8×10^{-6} m ~ 25×10^{-6} m) are of the same order of magnitude with the thickness of viscous sublayer at high Reynolds numbers. So, combined with the previous related literature [19] to [22], it could be expected that nozzle inner surface roughness should put some effects on the cavitation erosion ability of SRCW.

2 EXPERIMENTAL SETUP AND PROCEDURES

2.1 Experiment Apparatus and Procedures

A schematic diagram of the experimental setup for the cavitation erosion test under several ambient pressures is shown in Fig. 3. Pressured tap water was supplied from a plunger pump whose working pressure can be continuously regulated through the control table from 0 MPa to 60 MPa with a maximum flow rate of 120 l/min. Two bladder accumulators were applied to minimize the influence of pressure fluctuations of the pump on the experimental results. Specifically, one accumulator was installed near the pump, and the other one was positioned close to the nozzle being tested, as shown in Fig. 3. To remove the effects of pressure loss in the pipeline under different operating conditions, a pressure transducer (Model: BD DMP331P), which had been calibrated by the manufacturer, was installed immediately before the nozzle to make sure that the inlet pressure (P_i) of each test was consistent with the designed value of 25 MPa. The range and accuracy of the pressure transducer were 1 MPa to 40 MPa and ±0.05 %FS, respectively. And in each test, the shutter would not be removed until the value obtained by this transducer remained stable.

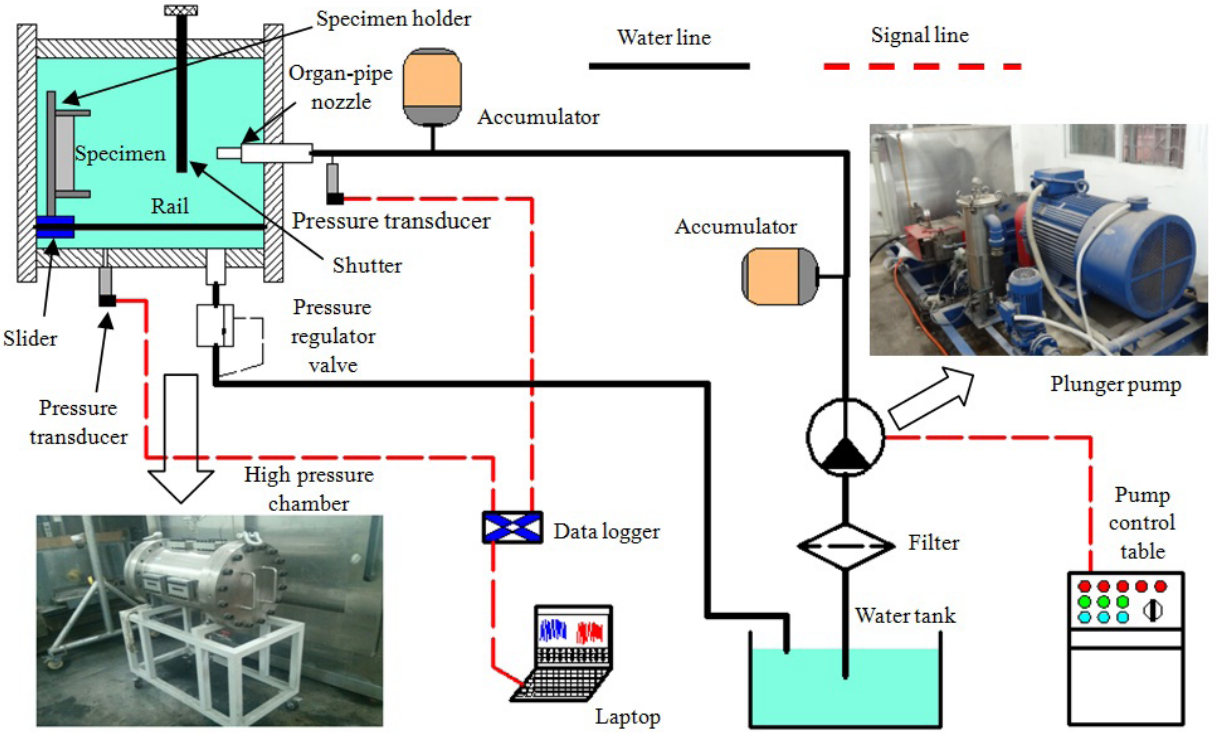

Fig. 3. *Schematic of experimental setup for erosion tests*

The tests were conducted in a high-pressure chamber made of stainless steel. The maximum design pressure of the chamber was 10 MPa, and the achievable standoff distance was 300 mm with a regulation precision of 0.5 mm. The chamber pressure (which is also the ambient pressure P_a) was regulated and controlled by an electromagnetic relief valve, as shown in the figure. Standoff distance, S, was defined as the distance from nozzle exit to the impingement surface of the specimen. Preliminary tests had been performed to determine a proper range of the testing standoff distance, which was from 10 mm to 100 mm with an interval of 10 mm. During the process of each test, the chamber pressure was monitored by another pressure transducer of the same model. The erosion time for each test was 180 seconds, which was guaranteed by removing the shutter between the nozzle and the specimen in the chamber.

The mass of each specimen was measured before and after each erosion test, and mass loss, Δm, was defined as the difference between the two values. The specimen was measured on an electronic balance (Model: Sartorius BSA224S-CW) with a resolution of 0.1 mg and linearity of 0.2 mg.

2.2 Nozzles and Specimens

In this experiment, all the organ-pipe nozzles had the same geometry with D_f = 13 mm, D_c = 5 mm, D_e = 2 mm, and L_c = 18 mm, which were obtained based on the design principles of organ-pipe nozzle proposed by Chahine [14]. The inner surface roughness values of the six nozzles (shown in Fig. 4) were 0.8 μm, 1.6 μm, 3.2 μm, 6.3 μm, 12.5 μm, and 25 μm, respectively, which were achieved by changing the machining process on a high-precision digital controlled lathe [22]. These roughness values are the most commonly used in machining nozzles of similar size. Before the tests, the inner surface roughness of each nozzle was measured on a roughness measuring instrument (Model: Hommel-Etamic T800 RC) with a resolution of 1 nm to ensure the precise accuracy of the roughness values. The manufacturer was Metrology, and the measuring range was 0.1 μm to 120 mm.

Considering that pure aluminium is commonly used in cavitation erosion tests [22], [28], and [29], the same material was used as a specimen here. The chemical composition and physical properties of the specimen are listed in Tables 1 and 2, respectively. It should be noted that the surface of each specimen exposed to the impingement of the jets had been

Table 1. Chemical composition of specimen (mass%)

Material	Chinese standard	Al	Si	Cu	Mg	Zn	Mn	Ti	Fe
Pure aluminium	1070A	99.70	≤0.20	≤0.03	≤0.03	≤0.07	≤0.03	≤0.03	0.000 ~ 0.250

Table 2. *Physical properties of specimen*

Material	Chinese standard	Density $\rho\times10^3$ [kg/m^3]	Elasticity modulus $E\times10^9$ [Pa]	Tensile strength $\sigma_b\times10^6$ [Pa]	Offset yield strength $\sigma_{0.2}\times10^6$ [Pa]	Vickers hardness $Hv\times10^9$ [Pa]
Pure aluminium	1070A	2.71	71	55	15	38

polished and measured on the mentioned roughness measuring instrument to ensure the uniformity of specimens.

Fig. 4. *The testing organ-pipe nozzles*

3 RESULTS AND DISCUSSION

Based on the previous related theoretical and experimental efforts [2], [22], and [28], the effects of nozzle inner surface roughness on the cavitating erosion intensity of SRCW were evaluated from the aspects of both the macroscopic appearances and the mass losses of the eroded specimens.

3.1 Macroscopic Appearances of the Eroded Specimens

Fig. 5 shows the macroscopic appearances of the eroded specimens at an ambient pressure of 4 MPa and a standoff distance of 40 mm. These photographs are chosen and displayed because the appearances reveal the most obvious differences at these operating conditions. From the size of the pit and the distribution density of the dots as well as the size of the eroded area, one can have a visualized and preliminary understanding of the effects of nozzle inner surface roughness on the cavitation erosion performance of SRCW.

As can be observed in the figure, all the eroded specimens have the typical appearance of cavitation erosion with a pit at the centre and a ring shape as the main erosion region composed of numerous small dots [28] to [30]. The pit is caused by the high-speed waterjet impingement of droplets, and the ring shape is created by a cavitation cloud. More specifically, when a cavitation bubble collapses to a boundary, micro-jets are formed during the process and subsequently a shock wave is generated at the moment of rebounding, resulting in the damage of materials most possibly through fatigue erosion [2]. It is clear that nozzle inner surface roughness significantly affects the cavitation ability. In more specific terms, the sizes of the pit in the centre are nearly the same with a diameter of about 4 mm for surface roughness values of 0.8 μm, 1.6 μm, and 3.2 μm. Moreover, the distribution of small dots composing the ring shape is somewhat scattered, and the general size is relatively small, meaning the cavitation abilities of these three nozzles are similar. Since the surfaces of these three nozzles are rather smooth, it should be reasonable to conjecture that this is because the mean height of the roughness elements is rather small compared with the viscous sublayer thickness under this condition. This is hydraulically smooth turbulent flow [25]. Therefore, the roughness elements can hardly protrude and interact with the viscous sublayer, and the turbulent behaviours of the high-speed flow cannot be affected nor can the cavitation ability.

From Fig. 5, it can be observed that the macroscopic appearance of the specimen eroded by the jets from the nozzle of the inner surface roughness of 6.3 μm is the most apparent, with respect to both the pit at the centre and the dots composing the ring shape. The pit has a diameter of about 8 mm, which is twice that of the pits on the specimens eroded by the jets from the nozzles of surface roughness values below 3.2 μm. In addition, the general sizes of the dots are larger, and the distributions are more concentrated. This indicates that both the high-speed waterjet impingement and the cavitation intensity are dramatically enhanced. Moreover, the improved

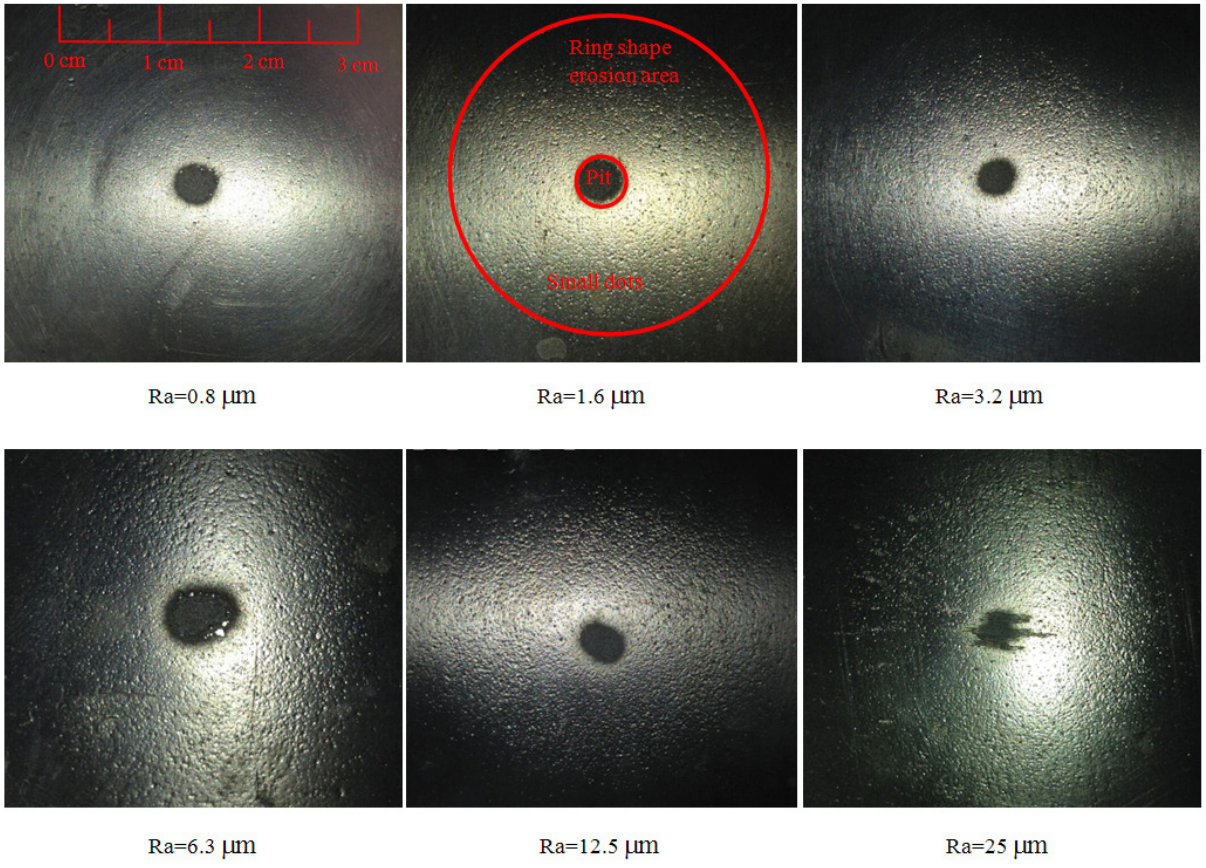

Fig. 5. *Photographs of the eroded specimens at Pa = 4 MPa, S = 40 mm, and σ = 0.190*

cavitation intensity is most probably caused by the increased inner surface roughness, as it is the only variable between each erosion test. It can be deduced that the improved impingement ability of the high-speed waterjet is most likely to be induced by the enhanced cavitation intensity. To be more specific, the promoted cavitation produces more bubbles around the jet periphery, leading to a great reduction of the friction and interaction between the high-speed jet and the surrounding fluid [29]. As a result, the high-speed water jet contains more energy, which subsequently leads to a bigger size of the pit at the centre.

With the surface roughness value increased to 12.5 μm, the sizes of the pit and the small dot become smaller again, meaning a reduction of both the impingement of high-speed waterjet and the cavitation intensity. This phenomenon is more evident when the nozzle inner surface roughness is increased to 25 μm. Under this condition, the pit is no longer a circle, indicating the jet beam is dispersed. The phenomenon suggests that surface roughness elements already violently interact with the high-speed flow through the viscous sublayer and put a disadvantageous effect on the cavitation erosion performance of SRCW. In contrast, it can be concluded that, under the current condition, surface roughness value of 6.3 μm is a critical value for the nozzle to achieve the strongest cavitation intensity. Below this value, surface roughness has little effect on the cavitation erosion behaviours, while above the value surface roughness will reduce the cavitation intensity.

3.2 Cavitation Erosion Intensity

Fig. 6 shows the mass loss of eroded specimen as a function of standoff distance with respect to various ambient pressures and values of nozzle inner surface roughness.

Each curve experiences a peak at a distance where the maximum mass loss occurs. This distance is called the optimum standoff distance. This observation suggests that the existence of an optimum standoff distance is a common feature of SRCW, regardless of the nozzle inner surface roughness. The main reason

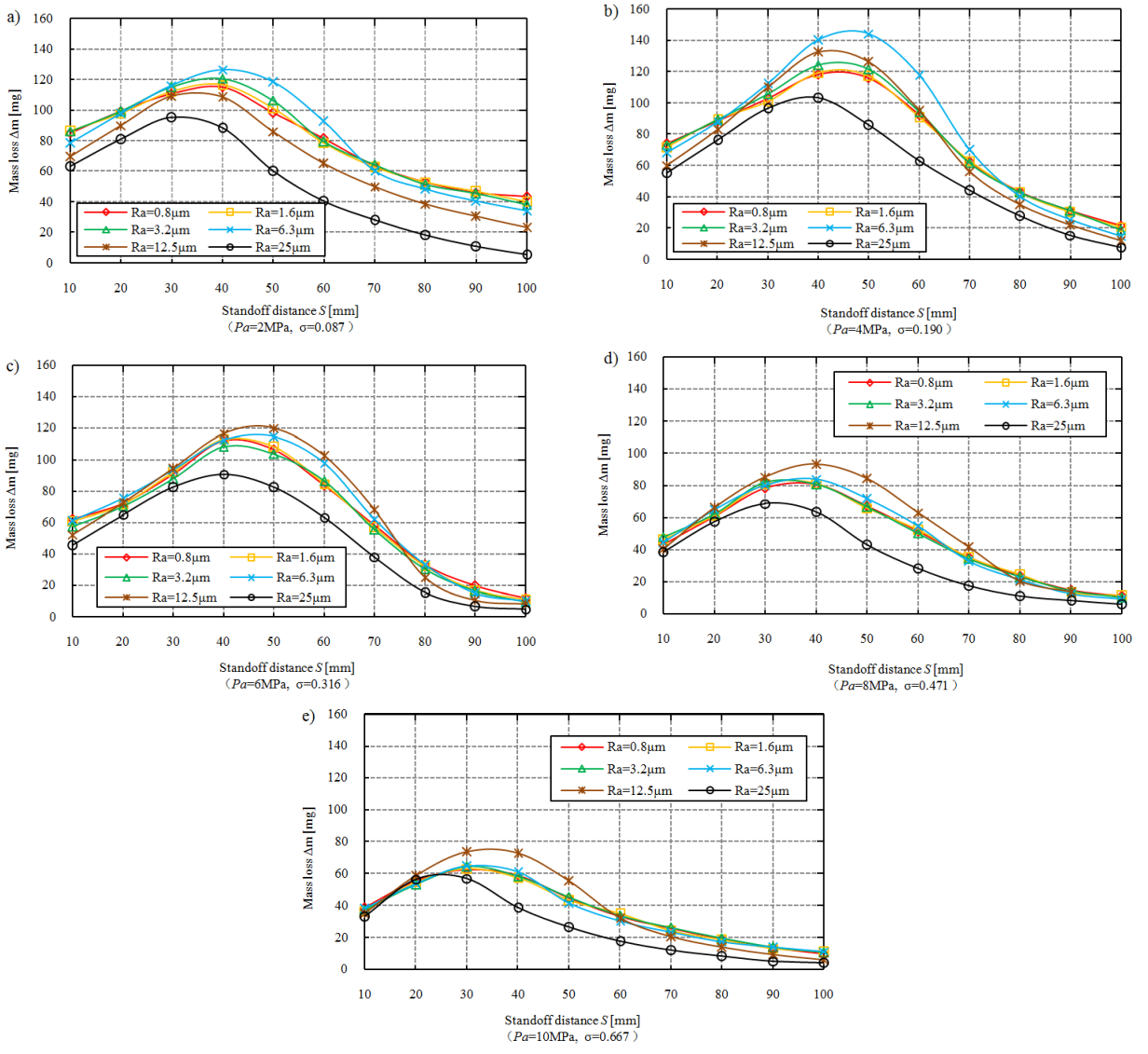

Fig. 6. *Mass loss as a function standoff distance at different ambient pressures; a) Pa = 2 MPa, b) Pa = 4 MPa, c) Pa = 6 MPa, d) Pa = 8 MPa, e) Pa = 10 MPa*

for the occurrence of optimum standoff distance is that bubbles generated in the boundary or shear layer need a certain time to grow into sizes at which the collapse of cavitation clouds could produce destructive power for the specimens [2]. Therefore, analysing the optimum standoff distance is an important way to evaluate the effects of nozzle inner surface roughness on cavitation erosion. Moreover, the figure makes it possible to determine a proper range of standoff distances where strong cavitating capabilities can be achieved under different operating conditions.

It is of great interest to note that even the nozzles have different values of surface roughness; the optimum standoff distance for each nozzle experiences the same tendency. More specifically, the optimum standoff distance first increases and then decreases with the increase of ambient pressure. This is in rough agreement with the experimental results obtained by Li et al. [18] and [31] who concluded that the optimum standoff distance should keep increasing with the increase of ambient pressure. The statement was that the increasing ambient pressure suppresses the bubbles. As a consequence, additional time was needed for the bubbles to grow, leading to an increase of the optimum standoff distance. Actually, this can also be used to explain the increased optimum

standoff distance at ambient pressures below 6 MPa. Since a certain degree of ambient pressure has the ability to keep the bubbles from bursting, more cavitation bubbles will exist in the shear layer under this condition. Another reason for the increasing optimum standoff distance should be the largely reduced friction between the jet and the surrounding fluid, caused by the enormous cavitation bubbles generated in the free shear layer. However, when the ambient pressure exceeds 6 MPa, the convective heat transfer and momentum and mass exchange between the jet and the ambient liquid become so violent that the energy of the jet dissipates rapidly with increasing standoff distance [32], leading to the decrease of the optimum standoff distance. In contrast, at high ambient pressures, pressure fluctuations around the jet are largely attenuated, causing a decrease in the number of cavitation bubbles. As a result, cavitating erosion intensity is dramatically weakened, which is reflected as a reduction of the optimum standoff distance [11].

It is a fact that an optimum standoff distance under all ambient pressures exists regardless of nozzle surface roughness. However, the values of the optimum standoff distance are different. For example, at ambient pressure of 2 MPa, the optimum standoff distance for the nozzle with a roughness value of 6.3 μm is around 45 mm, while for roughness values of 12.5 μm and 25 μm, it is about 35 mm. Furthermore, at ambient pressure of 2 MPa and 4 MPa, the optimum standoff distance of a nozzle with roughness value of 12.5 μm is always the largest. Furthermore, at ambient pressure of 6 MPa, 8 MPa, and 10 MPa, the optimum standoff distance of a nozzle with a roughness value of 25 μm is the largest.

In contrast, if the maximum mass loss is considered, it can be found that a roughness value of 6.3 μm is the best one at ambient pressures of 2 MPa and 4 MPa, while roughness value of 12.5 μm takes its place to be the best one at pump pressures of 6 MPa, 8 MPa, and 10 MPa. Specifically, proper surface roughness can promote the generation of cavitation bubbles, which is in satisfying agreement with the results obtained by Numachi et al. [33], who experimentally demonstrated that surface roughness could advance cavitation inception. Similar evidence can also be obtained from the research performed by Chang et al. [20].

Despite the influence of surface roughness on the value of optimum standoff distance, it is observed that nozzle inner surface roughness also significantly affects the magnitudes of the mass losses of the specimens.

As the figure illustrates that curves of roughness values of 0.8 μm and 1.6 μm are overlapped all the time, which means surface roughness below 1.6 μm have little effect on the cavitation erosion intensity. This is consistent with the assumption that the chamber plays a dominating role when the surface is relatively smooth. It is interesting to note that the maximum mass loss caused by the roughness value of 3.2 μm is a little larger than that caused by roughness values of 0.8 μm and 1.6 μm at lower ambient pressures (Fig. 6a and b). However, the difference between these curves diminishes gradually with increasing ambient pressure. After the ambient pressure has exceeded 6 MPa, the difference disappears (Fig. 6c and d). In addition, a surface roughness value of 25 μm should be avoided in the fabrication of organ-pipe nozzles because it leads to the weakest erosion intensity.

In order to provide a further discussion on the effects of nozzle inner surface roughness, the viscous sublayer thickness under each ambient pressure has been calculated and is shown in Table 3. It should be emphasized that only viscous sublayer thicknesses at nozzle chamber and exit were calculated because the velocity at nozzle inlet (U_i) is nearly 2.37% the velocity at nozzle exit (U_e). The calculation process is shown below.

The Bernoulli equation is [24]:

$$\frac{P_i}{\rho g}+\frac{U_i^2}{2g}=\frac{P_a}{\rho g}+\frac{U_e^2}{2g}+h_f+h_j, \tag{1}$$

where ρ is the liquid density, g is the acceleration of gravity, h_f is the frictional head loss, h_j is the local head loss.

$$h_f=\lambda\frac{l}{d}\frac{u^2}{2g}, \tag{2}$$

$$h_j=k\frac{u^2}{2g}, \tag{3}$$

where λ is the friction coefficient, l is the length of the flow channel (here it is the nozzle length), d is channel diameter, u is flow velocity, and k is the local resistance coefficient. Under the sudden contraction condition, k can be expressed as:

$$k=\frac{1}{2}\left(1-\left(\frac{A_2}{A_1}\right)^2\right)^2, \tag{4}$$

where A_1 and A_2 are the cross-section areas at the contraction.

In Eq. (2), λ, l, and u are rather small. So, it can be neglected during the calculation. When compared with U_e, U_i can also be neglected.

Table. 3. *Thickness of viscous sublayer under different conditions (in [μm,])*

Ra [μm]	P_a [MPa]									
	2		4		6		8		10	
	Chamber	Exit	Chamber	Exit	Chamber	Exit	Chamber	Exit	Chamber	Exit
0.8	9.011	0.0965	9.630	0.101	10.015	0.106	10.353	0.112	11.210	0.120
1.6	9.011	0.104	9.630	0.109	10.015	0.115	10.353	0.121	11.210	0.129
3.2	0.627	0.113	0.675	0.118	0.702	0.125	10.353	0.134	11.210	0.140
6.3	0.679	1.170	0.732	1.220	0.761	1.290	0.793	0.145	0.866	0.154
12.5	0.741	1.060	0.798	1.104	0.830	1.168	0.864	1.231	0.944	1.311
25	0.817	0.944	0.881	0.984	0.916	1.041	0.954	1.097	1.041	1.168

By combining Eqs. (1), (3), and (4), different U_e for each of the five ambient pressures are obtained, which are 172.20 m/s, 164.54 m/s, 156.52 m/s, 148.05 m/s, and 139.06 m/s, respectively.

For the viscous sublayer thickness, δ_l, it can be obtained by **[24]**:

$$\delta_l = \frac{32.8d}{\mathrm{Re}\sqrt{\lambda}}. \tag{5}$$

And Re is expressed by:

$$\mathrm{Re} = \frac{ud}{\nu}, \tag{6}$$

where ν is the fluid kinematic viscosity coefficient.

In terms of λ, it depends on Re and can be calculated as follows **[24]**:

For $10^4 < \mathrm{Re} < 26.98\left(\frac{d}{\Delta}\right)^{8/7}$:

$$\frac{1}{\sqrt{\lambda}} = 2\lg(\mathrm{Re}\sqrt{\lambda}) - 0.8, \tag{7}$$

where Δ is the absolute surface roughness, here, it is the surface roughness value.

For $26.98\left(\frac{d}{\Delta}\right)^{8/7} < \mathrm{Re} < 4160\left(\frac{d}{2\Delta}\right)^{0.85}$:

$$\frac{1}{\sqrt{\lambda}} = -2\lg\left(\frac{\Delta}{3.7d} + \frac{2.51}{\mathrm{Re}\sqrt{\lambda}}\right). \tag{8}$$

For $\mathrm{Re} > 4160\left(\frac{d}{2\Delta}\right)^{0.85}$:

$$\frac{1}{\sqrt{\lambda}} = 1.74 + 2\lg\frac{d}{2\Delta}. \tag{9}$$

From Eqs. (5) to (9), δ_l at each roughness value and each ambient pressure can be achieved, shown in Table 3.

Moreover, the important parameter defining cavitation intensity is cavitation number, σ, which can be expressed as:

$$\sigma = \frac{P_a - P_v}{\left(\rho U_e^2\right)/2}, \tag{10}$$

where P_v is the vapor pressure of the liquid.

From Table 3, it can be observed that the viscous sublayer thickness not only depends on the ambient pressure but also largely depends on the roughness value. And the sublayer thicknesses at chamber and exit are much different, particularly when the surface is relatively smooth, say 0.8 μm and 1.6 μm. The data also looks irregular. However, from the optimal surface roughness in Fig. 6, it seems that the viscous sublayer thicknesses at chamber and exit determine the erosion intensity respectively, depending on the surface roughness value. For example, at roughness values of 0.8 μm and 1.6 μm, the viscous sublayer thickness is around 10 μm, which is much thicker than the roughness element. As a result, the roughness elements are totally covered by the viscous sublayer and can hardly influence the turbulence core. Thus, the cavitation erosion intensities are similar.

When the viscous sublayer thickness at nozzle exit changes abruptly, the corresponding surface roughness results in the strongest cavitation erosion intensity. However, this is not applicable to the case of roughness value of 6.3 μm and ambient pressure of 6 MPa. Under this case, a roughness value of 6.3 μm is the one that causes the abrupt change, but roughness value of 12.5 μm is the optimum. Even with this inconsistency, the curves of roughness values of 6.3 μm and 12.5 μm nearly experience the same tendency. However, due to the rather limited literature on the effects of nozzle inner surface roughness, it is currently very difficult to provide an explanation for this phenomenon. Further theoretical and mathematical investigations need to be performed.

It is also observed in the figure that at an ambient pressure of 4 MPa, each surface roughness can cause a greater mass loss around the optimum standoff distance compared to those under the other ambient pressures, meaning a certain degree of ambient pressure can enhance the cavitation erosion intensity of SRCW. The fact that the jet has the strongest cavitation erosion intensity at an ambient pressure around 5 MPa is in good agreement with the results obtained by Johnson et al. **[11]**, demonstrating the reliability of our research.

4 CONCLUSIONS

For the purpose of enhancing the cavitation intensity of SRCW under ambient pressures, the effects of nozzle inner surface roughness values were studied by means of erosion testing. Unfortunately, there is currently little literature on the effects of nozzle inner surface roughness. Further investigations need to be conducted to understand the interactions of surface roughness and cavitation. However, the present study brings light to some evidence:

1. Under the experimental conditions, nozzle inner surface roughness has dramatic effects on the cavitation erosion performance of SRCW, which seems to largely depend on the viscous sublayer thickness. Corresponding to each ambient pressure, an optimum roughness value for achieving the strongest cavitation intensity exists.
2. The optimal surface roughness almost occurs at the place where the viscous sublayer thickness at the nozzle exit changes abruptly.
3. The existence of an optimum standoff distance is a common feature of SRCW, and the surface roughness affects its exact value of the optimum standoff distance.
4. A certain ambient pressure enhances cavitation erosion intensity, which is another feature of SRCW regardless of nozzle inner surface roughness.

5 ACKNOWLEDGEMENTS

This research is financially supported by the National Key Basic Research Program of China (No. 2014CB239203), the National Natural Science Foundation of China (No. 51474158) and the China Scholarship Council (No. 201406270047).

6 REFERENCES

[1] Karadžič, U., Bulatović, V., Bergant, A. (2014). Valve-induced water hammer and column separation in a pipeline apparatus. *Strojniški vestnik - Journal of Mechanical Engineering*, vol. 60, no. 11, p. 742-754, **DOI:10.5545/sv-jme.2014.1882**.

[2] Kim, K.H., Chahine, G., Franc, J.P., Karimi, A. (eds.) (2014). *Advanced Experimental and Numerical Techniques for Cavitation Erosion Prediction*. Springer, Dordrecht, **DOI:10.1007/978-94-017-8539-6**.

[3] Ciubotariu, C.R., Secosan, E., Marginean, G., Frunzaverde, D., Campian, V.C. (2016). Experimental study regarding the cavitation and corrosion resistance of Stellite 6 and self-fluxing remelted coatings. *Strojniški vestnik - Journal of Mechanical Engineering*, vol. 62, no. 3, p. 154-162, **DOI:10.5545/sv-jme.2015.2663**.

[4] Heath, D., Širok, B., Hočevar, M., Pečnik, B. (2013). The use of the cavitation effect in the mitigation of CaCO3 deposits. *Strojniški vestnik - Journal of Mechanical Engineering*, vol. 59, no. 4, p. 203-215, **DOI:10.5545/sv-jme.2012.732**.

[5] Perec, A., Pude, F., Stirnimann, J., Wegener, K. (2015). Feasibility study on the use of fractal analysis for evaluating the surface quality generated by waterjet. *Tehnički vjesnik - Technical Gazette*, vol. 22, no. 4, p. 879-883, **DOI:10.17559/TV-20140128231244**.

[6] Chahine, G.L., Kapahi, A., Choi, J.K., Hsiao, C.T. (2016). Modeling of surface cleaning by cavitation bubble dynamics and collapse. *Ultrasonics Sonochemistry*, vol. 29, p. 528-549, **DOI:10.1016/j.ultsonch.2015.04.026**.

[7] Dalfré Filho, J.G., Assis, M.P., Genovez, A.I.B. (2015). Bacterial inactivation in artificially and naturally contaminated water using a cavitating jet apparatus. *Journal of Hydro-environment Research*, vol. 9, no. 2, p. 259-267, **DOI:10.1016/j.jher.2015.03.001**.

[8] Biluš, I., Bombek, G., Hočevar, M., Širok, B., Cenčič, T., Petkovšek, M. (2014). The experimental analysis of cavitating structure fluctuations and pressure pulsations in the cavitation station. *Strojniški vestnik – Journal of Mechanical Engineering*, vol. 60, no. 3, p. 147-157, **DOI:10.5545/sv-jme.2013.1462**.

[9] Soyama, H. (2013). Effect of nozzle geometry on a standard cavitation erosion test using a cavitating jet. *Wear*, vol. 297, no. 1-2, p. 895-902, **DOI:10.1016/j.wear.2012.11.008**.

[10] Zhou, J., Hu, J. Jing, C. (2016). Lumped parameter modelling of cavitating orifice flow in hydraulic systems. *Strojniški vestnik - Journal of Mechanical Engineering*, vol. 62, no. 6, p. 373-380, **DOI:10.5545/sv-jme.2015.3082**.

[11] Johnson, V.E. Jr., Lindenmuth, W.T., Conn, A.F., Frederick, G.S. (1981). Feasibility study of tuned-resonator, pulsating cavitating water jet for deep-hole drilling. (No. SAND-81-7126). Sandia National Labs., Albuquerque, Hydronautics, Inc., Laurel., **DOI:10.2172/6266875**.

[12] Li, D., Kang, Y., Ding, X., Wang, X., Fang, Z. (2016). Effects of area discontinuity at nozzle inlet on the characteristics of self-resonating cavitating waterjet. *Chinese Journal of Mechanical Engineering*, vol. 29, no. 4, p. 813-824, **DOI:10.3901/CJME.2016.0426.060**.

[13] Johnson, V.E. Jr, Chahine, G.L., Lindenmuth, W.T., Conn, A.F., Frederick, G.S., Giacchino, G.J. (1984). Cavitating and structured jets for mechanical bits to increase drilling rate—Part I: Theory and concepts. *Journal of Energy Resources Technology*, vol. 106, no. 2, p. 282-288, **DOI:10.1115/1.3231053**.

[14] Chahine, G.L., Johnson, V.E. (1985). Mechanics and applications of self-resonating cavitating jets. *International Symposium on Jets and Cavities*, ASME, WAM, p. 21-33.

[15] Li, D., Kang, Y., Ding, X., Wang, X. Fang, Z., (2016). Effects of area discontinuity at nozzle inlet on the characteristics of high speed self-excited oscillation pulsed waterjets. *Experimental Thermal and Fluid Science*, vol. 79, p. 254-265, **DOI:10.1016/j.expthermflusci.2016.07.013**.

[16] Li, Z. (2014). Criteria for jet cavitation and cavitation jet drilling. *International Journal of Rock Mechanics and Mining Sciences*, vol. 71, p. 204-207, **DOI:10.1016/j.ijrmms.2014.03.021**.

[17] Johnson, V.E. Jr, Chahine, G.L., Lindenmuth, W.T., Conn, A.F., Frederick, G.S., Giacchino, G.J. (1984). Cavitating and structured jets for mechanical bits to increase drilling rate—Part II: Experimental results. *Journal of Energy Resources Technology*, vol. 106, no. 2, p. 289-294, **DOI:10.1115/1.3231054**.

[18] Li, G., Shi, H., Liao, H., Shen, Z., Niu, J., Huang, Z., Luo, H. (2009). Hydraulic pulsed cavitating jet-assisted drilling. *Petroleum Science and Technology*, vol. 27, no. 2, p. 197-207, **DOI:10.1080/10916460701700302**.

[19] Echouchene, F., Belmabrouk, H., Le Penven, L., Buffat, M. (2011). Numerical simulation of wall roughness effects in cavitating flow. *International Journal of Heat and Fluid Flow*, vol. 32, no. 5, p. 1068-1075, **DOI:10.1016/j.ijheatfluidflow.2011.05.010**.

[20] Chang, J.C., Huang, S.B. Lin, C.M. (2006). Effects of inlet surface roughness, texture, and nozzle material on cavitation. *Atomization and Sprays*, vol. 16, no. 3, p. 299-318, **DOI:10.1615/AtomizSpr.v16.i3.40**.

[21] [21] Li, D., Li X., Kang, Y, Wang, X., Long, X., Wu, S. (2015). Experimental investigation on the influence of internal surface roughness of organ-pipe nozzle on the characteristics of high speed jet. *Journal of Mechanical Engineering*, vol. 51, no. 17, p. 169-176, **DOI:10.3901/JME.2015.17.169**. (in Chinese)

[22] Li, D., Kang, Y., Wang, X., Ding, X., Fang, Z. (2016). Effect of nozzle inner surface roughness on the cavitation erosion characteristics of high speed submerged jets. *Experimental Thermal and Fluid Science*, vol. 74, p. 444-452, **DOI:10.1016/j.expthermflusci.2016.01.009**.

[23] Schubauer, G.B. Tchen, C.M., (2015). *Turbulent Flow*. Princeton University Press, Princeton.

[24] Elger, D.F., Roberson, J.A. (2013). *Engineering Fluid Mechanics*. Wiley, New York.

[25] Nikuradse, J. (1950). *Laws of Flow in Rough Pipes*. National Advisory Committee for Aeronautics, Washington.

[26] Li, X., Meng, J., Li, Z. (2011). Roughness enhanced mechanism for turbulent convective heat transfer. *International Journal of Heat and Mass Transfer*, vol. 54, no. 9, p. 1775-1781, **DOI:10.1016/j.ijheatmasstransfer.2010.12.039**.

[27] Li, D., Kang, Y., Ding, X., Wang, X., Fang, Z. (2016). An experimental investigation on the pressure characteristics of high speed self-resonating pulsed waterjets influenced by feeding pipe diameter. *Journal of Mechanical Science and Technology*, vol. 30, no. 11, p. 4997-5007, **DOI:10.1007/s12206-016-1019-3**.

[28] Hattori, S., Goto, Y., Fukuyama, T. (2006). Influence of temperature on erosion by a cavitating liquid jet. *Wear*, vol. 260, no. 11-12, p. 1217-1223, **DOI:10.1016/j.wear.2005.08.001**.

[29] Momma, T., Lichtarowicz, A. (1995). A study of pressures and erosion produced by collapsing cavitation. *Wear*, vol. 186-187, p. 425-436, **DOI:10.1016/0043-1648(95)07144-X**.

[30] Soyama, H. (2011). Enhancing the aggressive intensity of a cavitating jet by means of the nozzle outlet geometry. *Journal of Fluids Engineering*, vol. 133, no. 10, no. 101301, **DOI:10.1115/1.4004905**.

[31] Li, G., Shen, Z., Zhou, C., Zhang, D., Chen, H. (2005). Investigation and application of self-resonating cavitating water jet in petroleum engineering. *Petroleum Science and Technology*, vol. 23, no. 1, p. 1-15, **DOI:10.1081/LFT-20009686218**.

[32] Kerst, A.W., Judat, B., Schlünder, E.-U. (2000). Flow regimes of free jets and falling films at high ambient pressure. *Chemical Engineering Science*, vol. 55, no. 19, p. 4189-4208, **DOI:10.1016/S0009-2509(00)00074-9**.

[33] Numachi, F., Ōba, R., Chida, I. (1965). Effect of surface roughness on cavitation performance of hydrofoils—Report 1. *Journal of Basic Engineering*, vol. 87, no. 2, p. 495-502, **DOI:10.1115/1.3650583**.

Strojniški vestnik - Journal of Mechanical Engineering 63(2017)2, 103-110

DOI:10.5545/sv-jme.2016.3805 Original Scientific Paper
Received for review: 2016-06-15
Received revised form: 2016-11-21
Accepted for publication: 2016-11-29

Inverse Method for Controlling Pure Material Solidification in Spherical Geometry

Mohamed Charifi* – Rabah Zegadi
University of Sétif, Institute of Optics and Precision Mechanics, Algeria

In this study, we present the control of the solidification process of a phase-changing, pure material described in one-dimensional spherical geometry. We used an inverse global descent method in which the gradient and the adjoint equation are constructed in continuous variables of time and space. The control variable is the temperature at the fixed boundary of the solid domain. For the desired solidification front, the control was determined using information on the heat flux deduced by heat balance. The numerical resolution was based on a finite difference method in a physical domain with a moving grid related to the evolving solidification front with time. The developed numerical model was validated using an exact built solution. The numerical results of the control problem are presented for both the exact and noisy data cases. For the noisy data, a regularization method was applied. In the case of the exactdata, a rapid control determination was achieved except for time steps near the end. The random errors effects in bruited data were considerably reduced by regularization.
Keywords: phase change, interface solid/liquid, inverse problem, spherical geometry

Highlights
- *Control of pure material solidification in spherical geometry was studied for a solidification planar front.*
- *An inverse global method has been used to determine the temperature at the fixed boundary of the solid domain as a control.*
- *The numerical resolution was based on the finite difference method in a physical domain with a moving grid.*
- *The algorithm has enabled the rapid control determination with excellent accuracy.*

0 INTRODUCTION

Material phase change represents a major challenge in various fields (metallurgy, heat storage systems, food conservation, etc.). Each year, more than a billion tons of metals are solidified around the world, mainly ferrous alloys (steel, cast iron), and aluminium. Moreover, storing thermal energy methods used in the food and pharmaceutical industries and air conditioning are directly related to the melting and solidification phenomena. In the case of material solidification, the kinetics of the state change and, more specifically, the geometry of the interface phase transition and its evolution over time determine the structure and properties of the final state. The determination by direct measurement of the mobile interface is generally very difficult to achieve. Inverse methods are most commonly used to simulate such phenomena of phase change. The control of the solidification front of a material by simulation, in metallurgy, for example, enables modification of its mechanical properties (hardness, toughness or mechanical strength). These properties depend mainly on the parameters used in the simulation (temperature, heat flux, the geometry of the solid/liquid interface and its velocity evolution). It is, therefore, necessary to control the solid/liquid interface in order to obtain particular desired properties.

The melting or solidification of pure substances and eutectic alloys are characterized by a well-defined melting temperature. The solid and liquid phases are well differentiated by a sharp interface.

In the case of mixtures and non-eutectic alloys, the phase change spreads out over a temperature range where the solid and liquid phases coexist. This two-phase mushy region is limited by an interface with the liquid phase at the liquidus temperature and another interface with the solid phase at the solidus temperature [1].

Solid/liquid phase change problems have been widely discussed by several authors using either inverse or direct methods. Zabaras and Ruan [2] sequentially solved a one-dimensional inverse Stefan solidification problem. They used a deformable finite element method to calculate the position and the speed of displacement of the interface and information on the temperature measured by two or more sensors located within the solid phase. Zabrasand Kang [3] treated an iterative resolution numerical simulation of a freezing front control problem in a linear case. Samaï et al. [4] identified the position of the solidification front using an iterative descent method. Jiang and al. [5] solved an inverse problem by the conjugate gradient method using finite differences to determine the historic heat flux and the final temperature distribution. Tikhonov's zero order regularization method was introduced to stabilize the inverse solution. Hetmaniok and Słota

*Corr. Author's Address: University of Sétif, The Institute of Optics and Precision Mechanics, 19000 Sétif, Algeria, charifi_mohamed@yahoo.fr

[6] determined the boundary conditions in the process of binary alloy solidification when the temperature measurements at selected points of the cast are known. In this model of Stefan, the liquidus temperature varies with the concentration of the alloy component.

Various direct methods were also used by some authors for determining the temperature at a fixed boundary, knowing the position of a mobile interface solid/liquid [7] or for evaluating the position of one or many mobile interfaces for a given temperature [8] to [10]. Other studies on phase change on materials (PCM) were treated using cylindrical or spherical coordinates [11] to [13], by fixing the mobile front in the presence of convection [14] and increasing energy storage [15].

The position of the solid/liquid interface can be directly determined experimentally using temperature measurements [16], optical monitoring [17], x-ray [18], ultrasound [19] and [20], eddy current [21], thermoelectric [22], and electrical resistance diagnostics. Although these experimental techniques are largely used for identifying the solid/liquid interface in a phase change problem, they remain expensive and difficult to implement. Moravčík et al. treated experimentally the solidification conditions of cold worked high alloy tool steel in comparison to construction steels in quasi equilibrium state [23]. Steiner Petrovič and Šturm experimentally study the modification of a non-oriented electrical steel sheet entirely treated with antimony using a laser surface alloy [24]. Hriberšek et al. solved inverse problem for determining surface heat transfer coefficient between liquefied nitrogen and a plate of inconel 718. The design of the numerical simulation was validated experimentally [25].

Indirect identification or control of the solid-liquid interface requires a simulation of the problem and its resolution. In the case of material solidification, the phase change problem can be resolved by inverse methods, usually validated by experimental data. From a theoretical perspective, the validation of a simulation (mathematical model used) can be done using exact solutions in particular situations instead of experimental data.

In a solidification phase change process, the solid and liquid phases have different thermophysical properties. In the solid phase, the heat transfer is purely conductive. In the liquid phase, two heat transfer situations are possible. If the liquid phase is maintained at the phase change temperature as in our study case, the heat transfer is purely conductive. When the temperature of the liquid phase is greater than the phase change temperature, the heat transfer occurs by diffusion and natural convection.

The purpose of this work is to control a pure material solidification by an optimization method formulated as an inverse problem of thermal conduction. We are interested in the control of the solid/liquid interface for a pure material in one-dimensional spherical geometry considering a planar front. The control variable used is the temperature at the fixed boundary of the solid domain. The given problem data are the initial state, the desired front (planar front) evolution, and the phase change temperature. With supplementary information on the heat flux at the front deduced from a heat balance, the inverse problem resolution can be made. The thermal system of our problem is governed by the conduction equation. We introduce for this resolution the least square criteria characterizing the difference between the dynamic behaviour of the system and the corresponding developed mathematical model. We then introduce the adjoint equation for evaluating the criteria gradient. The use of an iterative algorithm based on a conjugated gradient enables to find the optimal solution. We described the problem equation with space-and-time continuous variables and the procedure for finding the criteria gradient with the corresponding adjoint equation. The numerical resolution was undertaken using the conventional finite difference method with a mobile grid related to the considered physical domain. The time variable is then discretized according to the Crank-Nicolson unconditionally stable scheme. The exposed results concern the exact built solution and the noisy exact data. In order to guaranty the well-posed problem and a stable solution for the noisy data case, Tickonov's regularization method was used.

1 INVERSE PROBLEM FORMULATION

The equations that govern the problem for the solid and the liquid phases are presented in the following.

1.1 Solid Phase

In the solid phase, the temperature $T(r,t)$ $r\in[S_d(t),\mathrm{R}]$ and the heat flux $\phi_s(t)$ penetrating the moving boundary $S_d(t)$ in the time interval $[0,t_f]$ are obtained by the resolution of the following thermal conduction equations:

$$\rho_s c_s \frac{\partial T(r,t)}{\partial t} - \frac{\lambda_s}{r^2}\frac{\partial}{\partial r}\left(r^2 \frac{\partial T(r,t)}{\partial r}\right) = 0, \qquad (1)$$

$$T(0,t) = U(t), \qquad (2)$$

$$T(S_d(t),t) = T_f, \quad (3)$$

$$S_d(t=0) = S_0, \quad (4)$$

$$T(r,0) = T_0(r), \quad (5)$$

$$\varphi_s(t) = \lambda_s \frac{\partial T(S_d(t),t)}{\partial r}. \quad (6)$$

1.2 Liquid Phase

In the liquid phase, the temperature $T(r,t)$ r$\in[0,S_d(t)]$ and the heat flux $\phi_l(t)$ penetrating the moving boundary $S_d(t)$ in the time interval $[0,t_f]$ are obtained by the resolution of the following thermal conduction equations:

$$\rho_l c_l \frac{\partial T(r,t)}{\partial t} - \frac{\lambda_l}{r^2}\frac{\partial}{\partial r}\left(r^2 \frac{\partial T(r,t)}{\partial r}\right) = 0, \quad (7)$$

$$T(S_d(t),t) = T_f, \quad (8)$$

$$\frac{\partial T(0,t)}{\partial r} = 0, \quad (9)$$

$$S_d(t=0) = S_0, \quad (10)$$

$$T(r,0) = T_0(r), \quad (11)$$

$$\varphi_l(t) = \lambda_l \frac{\partial T(S_d(t),t)}{\partial r}, \quad (12)$$

where the variables r, t and T in their non-dimensional forms are defined as follows:

$$r^* = \frac{r}{R}, \quad t^* = \frac{t\cdot\lambda}{\rho\cdot c\cdot R^2}, \quad T^* = \frac{T-T_f}{T_{ref}}, \quad (13)$$

where $T_{ref} = T(0,0) - T(0,t_f)$.

Remark: thereafter the symbol * will be omitted.

During solidification, the heat balance (Stefan equation) at the solid/liquid interface can be expressed as:

$$\varphi_p(t) - \varphi_l(t) = \varphi_L(t) = \rho_l L \frac{dS(t)}{dt}. \quad (14)$$

In the case in which the liquid phase is maintained at the melting temperature T_f, the heat flux entering the solid is:

$$\varphi_p(t) = \varphi_l(t) = \rho_l L \frac{dS(t)}{dt}. \quad (15)$$

To solve the direct problem, we need to determine $T(r,t;U)$ and $\phi_s(t;U)$ from the data: $\{t_f, S_0, T_0(r), T_f, S_d(t)\}$ and from the $U(t)$ control in the interval $(0<t<t_f)$. If $\phi_p(t)$ is the prescribed flux entering the solid at the front, the inverse problem to solved is to find the control $U^*(t)$ on $[0,t_f]$ from the data set in order to obtain $\phi_s(t;U^*)$ as close as possible to $\phi_p(t)$.

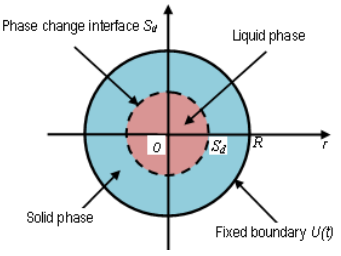

Fig. 1. *Definition domain solidification process*

1.3 Assumptions

This simulation concerns a pure material where the following assumptions are usually admitted for this type of material:

- The material in each phase is homogeneous and isotropic.
- The thermo-physical properties (λ,ρ,c) of the material are independent of temperature, but they are different form phase to phase.
- The effect of natural convection in the liquid phase of the material is not taken into account (constant density).
- No internal heat generation and all radiation effects are neglected.
- The mould wall is considered very thin with no temperature gradient. Its thermal resistance can be neglected.

2 INVERSE RESOLUTION METHOD

The introduced least squares criterion J is:

$$J(U) = \int_0^{t_f} w_1(t)(\varphi_s(t;U) - \varphi_p(t))^2\, dt. \quad (16)$$

The problem resolution consists in determining $U^*(t)$ with the conditions: $U^* \in V$,$\forall t \in [0,t_f]$ such that: $J(U^*) = \inf J(U)$ where V is the set of admissible solutions.

A Ribière-Polak conjugate gradient algorithm is used to calculate the time interval $[0,t_f]$ the iterates $U(t)$ according to the following steps:

1. Determination of T $(r,t;U^n)$ and $\phi_s(t;U^n)$ as solutions of the direct problem in the solid phase.
2. Evaluation of the criterion $J(U^*)$.
3. Resolution of the adjoint problem to calculate $\nabla J^n(t;U)$, the gradient of the criterion J with respect to U.
4. Solving the problem of variation to determine $\delta T(r,t)d$.
5. Determination of the iterates $U^{n+1}(t)$ using the following equation:

$$U^{n+1}(t) = U^n(t) - \theta^n d^n, \quad n = 1,2,3,\ldots, \tag{17}$$

with the descent direction d^n defined as:

$$d^n = \nabla J^n(t;U) + \alpha^n d^{n-1}, \tag{18}$$

and $$\alpha^n = \frac{\int_0^{t_f}\left[\nabla J^n - \nabla J^{n-1}\right]\nabla J^n dt}{\int_0^{t_f}\left[\nabla J^{n-1}\right]^2 dt}.$$

Gâteaux's directional derivative $D_{\delta U}(U)$ of the functional J at point U in the direction δU is defined by:

$$\delta J(\mathrm{U}) = \mathrm{D}_{\delta \mathrm{U}} J(U) = \lim_{\varepsilon \to 0} \frac{J(U+\varepsilon\delta U) - J(U)}{\varepsilon}, \tag{19}$$

$$\delta J(U) = 2\int_0^{t_f} w_1(t)\ (\varphi_s(t;U) - \varphi_p(t))\ \delta\varphi_s(t;U)\ dt, \tag{20}$$

$$\mathrm{D}_{\delta \mathrm{U}} J(U) = \int_0^{t_f} \nabla J(t;U)\delta U(t) dt. \tag{21}$$

Using the definition of Gâteaux's derivative and computing the variations, we obtain the variation problem where δT and $\delta\phi$ are solutions of the following variation equations:

$$\frac{\partial \delta T(\mathrm{r,t})}{\partial \mathrm{t}} - \frac{2}{r}\frac{\partial \delta T(r,t)}{\partial r} - \frac{\partial^2 \delta T(r,t)}{\partial r^2} = 0, \tag{22}$$

$$\delta T(1,t) = \delta U(t), \tag{23}$$

$$\delta T(S_d(t),t) = 0, \tag{24}$$

$$S_d(t=0) = S_0, \tag{25}$$

$$\delta T(r,0) = 0, \tag{26}$$

$$\delta\varphi = \lambda_s \frac{\partial \delta T(S_d(t),t)}{\partial r}. \tag{27}$$

After introducing the adjoint variable $P(r,t)$ on the variation problem and integrating, we obtain the following equations system in accordance with Eq. (20):

$$\frac{\partial P(\mathrm{r,t})}{\partial \mathrm{t}} - \frac{2}{r}\frac{\partial P(r,t)}{\partial r} + \frac{\partial^2 \delta T(r,t)}{\partial r^2} + \frac{2P(r,t)}{r^2} = 0,$$
$$S_d(t) \le r \le R\ , \quad 0 \le t \le t_f, \tag{28}$$

$$P(1,t) = 0, \tag{29}$$

$$P(S_d(t),t) = 2w_1(t)(\varphi_s(t;U) - \varphi_p(t)), \tag{30}$$

$$P(r,t_f) = 0. \tag{31}$$

Solving this equations system has to be done backward from the final condition $P(r,t_f)=0$. Using Eq. (21), the criterion gradient can be expressed as:

$$\nabla J(U) = -\frac{\partial P(1,t)}{\partial r}. \tag{32}$$

3 NUMERICAL RESOLUTION

As the solidification front is moving with time, we use the following transformation:

$$\xi = \frac{r-1}{S_d(t)-1}, \quad S_d(t)\ \le r \le 1 \quad \Leftrightarrow \quad 0 \le \xi \le 1, \tag{33}$$

This transformation enables obtaining a physical computation domain with a mobile mesh and to return to the natural variable r after resolution. The time variable is then discretized according to the unconditionally stable Crank-Nicolson's finite difference scheme.

By using a three-point off-centred derivate, the discreet gradient of the criteria is given by the following equation:

$$\nabla J(t;U) = -\frac{1}{(S_d^k - 1)}\left[\frac{\partial P}{\partial \xi}\right]_{im}^k = \left(\frac{3P_{im}^k - 4P_{im-1}^k + P_{im-2}^k}{2(S_d^k - 1)\Delta\xi}\right), \tag{34}$$

To verify the numerical model and the control algorithm reliability, we built the following exact solution:

$$T(r,t) = -\frac{1}{r}\left[e^{-\left[(0.2)^2 t - (0.2)r\right]} - e^{(-0.2)}\right]. \tag{35}$$

3.1 Case of No-Noisy Exact Data

The optimization algorithm used to determine the optimal control $U(t)$ that ensures a desired evolution front $S_d(t)$ was tested with and without a weighting function. When the weighting function is ($w_1(t)=1$), the algorithm converges but after a significant number of iterations ($n>1000$). Instead, the introduction of the weighting function $w_1(t)=t^2$ (Fig. 2a) allows the algorithm to converge more quickly after few iterations ($n=54$). Consequently, the weighting function has an impact on the computation time and the number of iterations. The improved results over the considered entire thermal process interval depend on the initial guess. The latter must not be chosen arbitrarily. It must belong to the domain of admissible solutions and obey the laws of heat transfer.

Figs. 2a and b show that the control $U(t)$ the flux at the fixed boundary are obtained with high precision after a few number of iterations on 95 % of the time horizon. At the remaining time, important errors appear as expected from these global optimization methods.

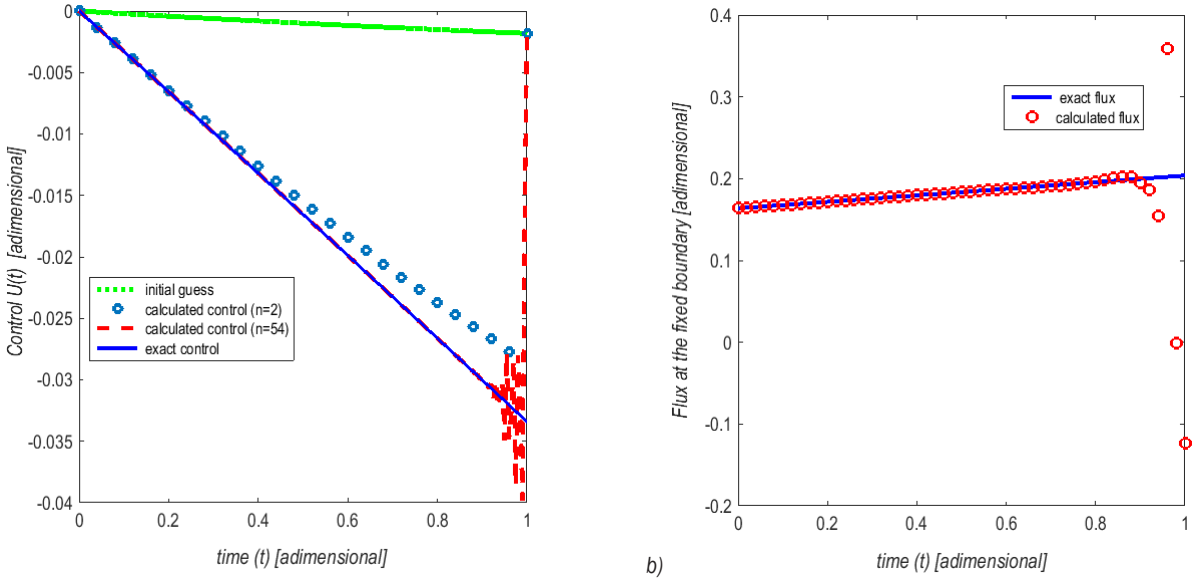

a) b)

Fig. 2. *a) Exact control and calculated and b) exact flux and calculated (no-noisy exact data)*

3.2 Case of Noisy Exact Data

To simulate these errors and generate a data flux $\phi_p(t)$ close to reality, a white noise $b(t)$ is added to the data $\phi_p(t)$ with a 5 % maximal amplitude using the following relation:

$$\varphi_p(t) = \varphi_p(t)_{exact} + b(t), \tag{36}$$

with $b(t)=\gamma(t)(0.05)\phi_{ref}$, $\gamma(t)$ is a random variable with a uniform probability density over $[-1, 1]$ and ϕ_{ref} is defined as:

$$\varphi_{ref} = \frac{\varphi_p(t_f)_{exact} + \varphi_p(0)_{exact}}{2}. \tag{37}$$

Fig. 3 shows that the inverse methods are susceptible to errors. The white noise added to the data $\phi_p(t)$ caused significant oscillations on the results. The relative error on the evaluated control $U(t)$ is about 20 %. This is related to the ill-posed nature of the problem. Consequently, these results are not satisfactory. According to [26], in the case of noisy

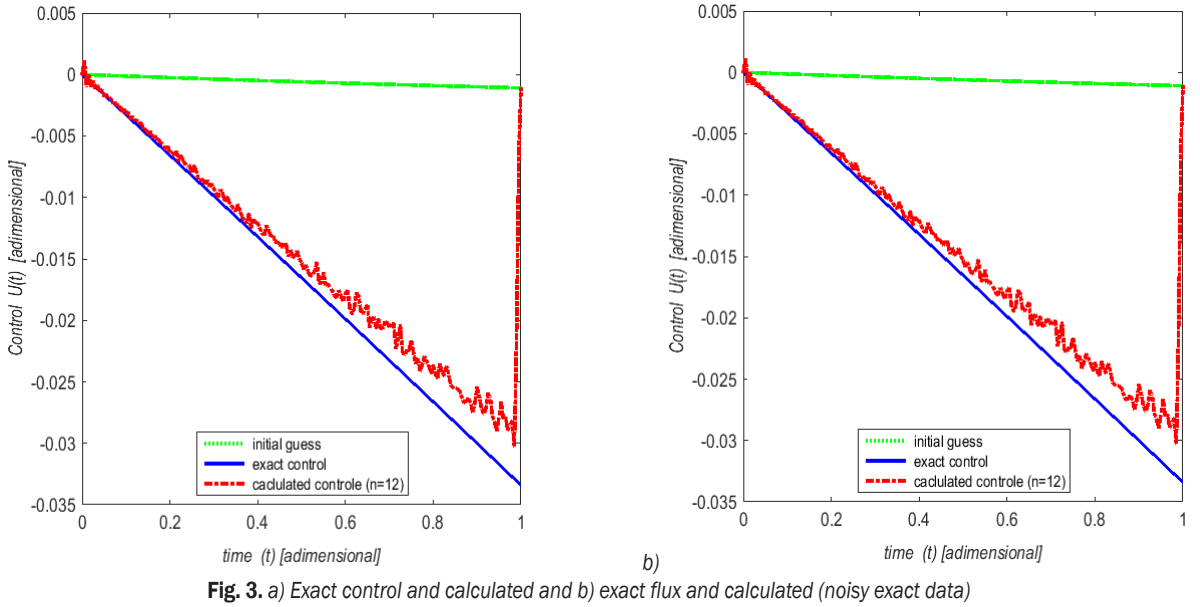

a) b)

Fig. 3. *a) Exact control and calculated and b) exact flux and calculated (noisy exact data)*

data, the computing stop criterion must satisfy the following condition:

$$\left| J(\mathrm{U}^{n+1}) - J(U^n) \right| < \varepsilon, \tag{38}$$

where ε: is the maximum amplitude of the noise.

3.3 Regularized Problem

In order to improve the results caused by the added white noise, the regularization method recommended by [27] was applied.

It consists of adding a criterion penalty term that keeps $U(t)$ in a function subspace and controls its variation rate. This method improves the accuracy of the U control obtained when the data are noisy.

The criterion $J(U)$ becomes:

$$J(U) = \int_0^{t_f} \mathrm{w}_1(t)(\varphi_s(t;U) - \varphi_p(t))^2 dt + \\ + \eta \int_0^{t_f} w_2(t) \left[\frac{dU(t)}{dt} \right]^2 dt, \tag{39}$$

where $w_2(t)=(t_f-t)$ is a weighting function and η is a regularization parameter. After derivation, we obtain the following discreet gradient:

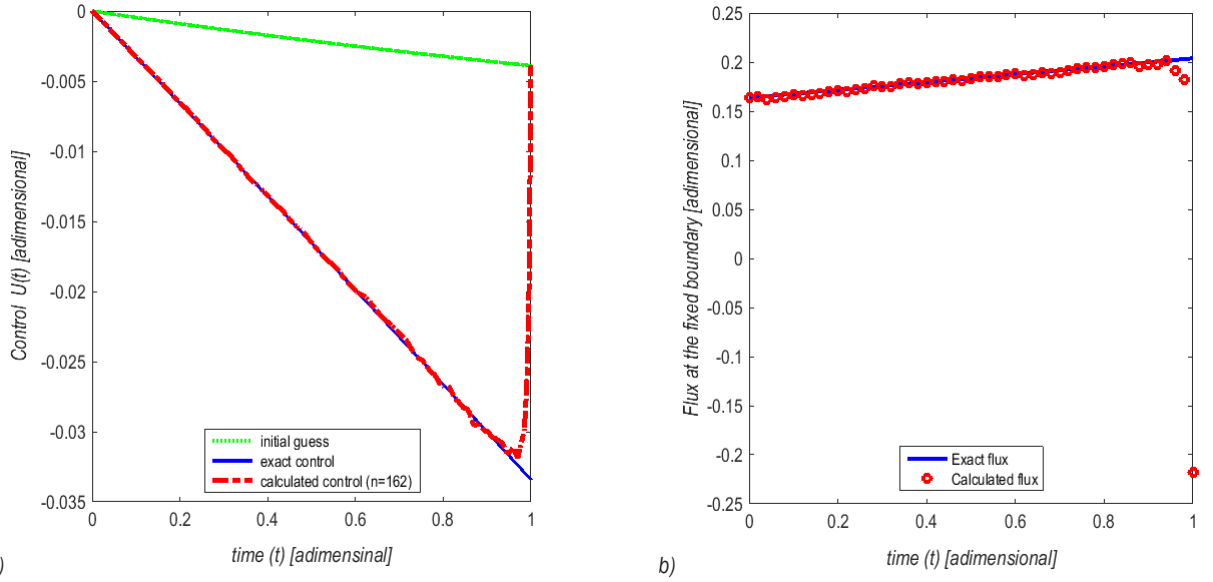

a) b)

Fig. 4. *a) Exact control and calculated and b) exact flux and calculated (Regularized problem)*

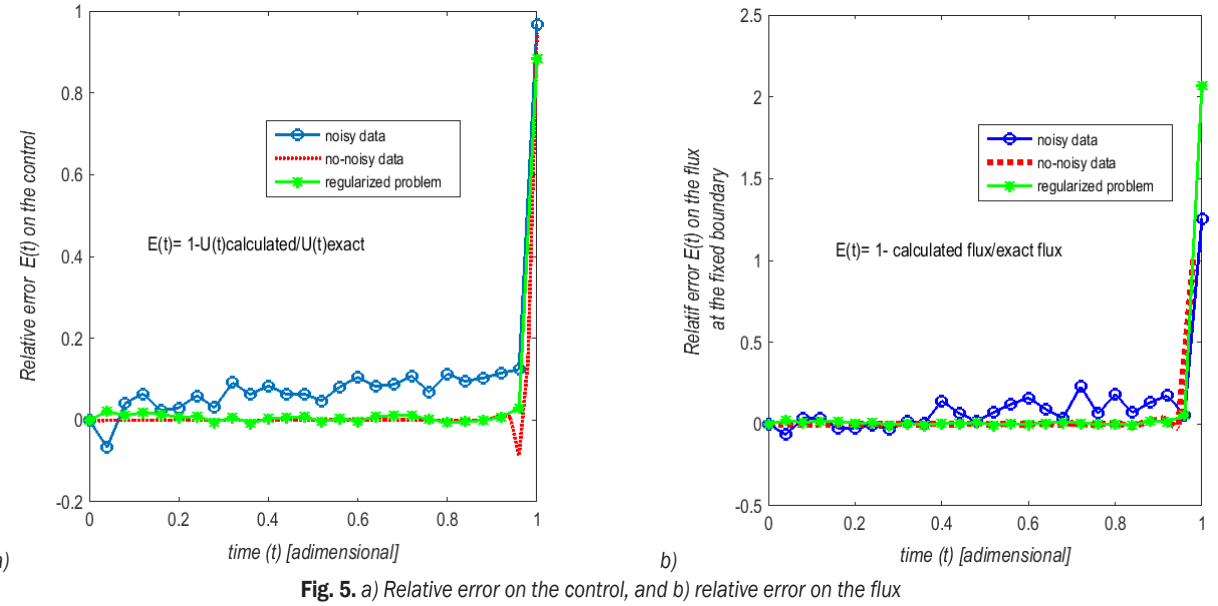

a) b)

Fig. 5. *a) Relative error on the control, and b) relative error on the flux*

$$\nabla J(t;U) = -\frac{\partial P(1,t)}{\partial r} - 2\eta \left[U'(t) - w_2(t)U''(t)\right]. \quad (40)$$

The choice of parameter η is made heuristically by successive tests while inspecting the solution regularity.

The results obtained using Tikhonov's method are satisfactory as shown in Fig. 4.

Fig. 5 represents the comparison of the relative error control Fig. 5a and flux Fig. 5b for no-noisy exact data, noisy exact data and those of the regularized problem. The oscillations amplitudes clearly decrease for the regularized problem. The control $U(t)$ and the flux $\phi(0,t)$ are stabilized over time.

4 CONCLUSIONS

An inverse method to control the evolution of the solidification front of a pure material in a one-dimensional spherical geometry problem was studied. This "ill-posed" problem was solved by using information as a prescribed flux at the front deduced from a heat balance.

It was formulated as an optimization problem in which a criterion of least squares is introduced between the model and the object. We then introduced the adjoint equation to accurately calculate the gradient criterion. The obtained equations were discretized using the finite differences classic method in a moving mesh domain. The numerical model was validated by an exact built solution. The resolution was carried out using the global conjugate gradient method. In the case of non-nosy exact data, the algorithm has enabled the rapid control determination with excellent accuracy except for the time steps near the end. The introduction of a selected initial guess has allowed the algorithm to converge more quickly. In the presence of random errors (noisy exact data case) on the prescribed flux, the used regularization method reduced their effects on the obtained control.

These obtained results constitute a good starting point for future work in which we consider the pure material solidification resolution in two-dimensional geometry and introducing convection.

5 NOMENCLATURE

C specific heat [J·kg^{-1}·k^{-1}],
d direction of displacement,
J criteria,
L latent heat [J·kg^{-1}],
T temperature [K],
P adjoint variable,
U control,
S position front,
V set of admissible solutions,
w_1, w_2 weighting functions,
R radial coordinate [m],
t time coordinate [s],
R dimensionless radial coordinate.

Greek symbols
α, ε positive real numbers,
ξ transform space coordinate,
η regularization parameter,
λ thermal conductivity [W·m^{-1}·K^{-1}],
ρ material density [kg·m^{-3}],
δ, ϕ differential, heat flux.

Subscripts
$0, f$ initial final
i, k space time nodes index
s, l solid, liquid
n iteration number

6 REFERENCES

[1] Ozisik, M.N., Orlande, H.R.B. (2000). *Inverse Heat Transfer: Fundamentals and Applications*. Taylor and Francis, New York.

[2] Zabaras, N., Ruan, Y. (1989). A deforming finite element method analysis of inverse Stefan problems. *International Journal for Numerical Methods in Engineering*, vol.28, no. 2, p. 295-313, **DOI:10.1002/nme.1620280205**.

[3] Zabaras, N., Kang, S. (1993). On the solution of an ill-posed design solidification problem using minimization techniques in finite and infinite-dimensional function spaces. *International Journal for Numerical Methods in Engineering*, vol. 36, no. 23, p. 3975-3990, **DOI:10.1002/nme.1620362304**.

[4] Samaï, M., Jarny, Y., Delaunay, D. (1993). An optimisation method using an adjoint equation to identify solidification front location. *Numerical Heat Transfer, Part B: Fundamentals,* vol. 23, no. 1, p. 67-89, **DOI:10.1080/10407799308914890**.

[5] Jiang, H., Nguyen, T.H., Prud'homme, M. (2005). Control of the boundary heat flux during the heating process of a solid material. *International Communications in Heat and Mass Transfer*, vol. 32, no. 6, p. 728-738, **DOI:10.1016/j.icheatmasstransfer.2004.10.009**.

[6] Hetmaniok, E., Słota, D. (2012). Numerical procedure of solving some inverse problem in solidification of the binary alloy. *Computer Assisted Methods in Engineering and Science*, vol. 19, p. 393-402.

[7] Ren, H.-S. (2007). Application of the heat-balance integral to an inverse Stefan problem. *International Journal of Thermal Sciences*, vol. 46, no. 2, p. 118-127, **DOI:10.1016/j.ijthermalsci.2006.04.013**.

[8] Momose, K., Yamakawa, T.,Kimito, H.(1998). An inverse analysis of two-phase Stefan problems using imaginary heat sources. *Heat Transfer – Asian Research*, vol. 27, no. 3, p. 179-191, **DOI:10.1002/(SICI)1520-6556(1998)27:3<179::AID-HTJ1>3.0.CO;2-S**.

[9] Yu, X., Nelson, D.J., Vick, B. (1995). Phase change with multiple fronts in cylindrical systems using the boundary element method. *Engineering Analysis with Boundary Elements*, vol. 16, no. 2, p. 161-170, **DOI:10.1016/0955-7997(95)00052-6**.

[10] Nowak, I., Nowak, A.J., Wrobel, L.C. (2002). Identification of phase change fronts by Bezier splines and BEM. *International Journal of Thermal Sciences*, vol. 41, no. 6, p.492-499, **DOI:10.1016/S1290-0729(02)01342-X**.

[11] Regin, A.F., Solanki, S.C., Saini, J.S. (2006). Latent heat thermal energy storage using cylindrical capsule: Numerical and experimental investigations. *Renewable Energy*, vol.31,no. 13, p.2025-2041, **DOI:10.1016/j.renene.2005.10.011**.

[12] Bilir, L., Ilken, Z. (2005). Total solidification time of a liquid phase change material enclosed in cylindrical/spherical containers. *Applied Thermal Engineering*, vol. 25, no. 10, p. 1488-1502, **DOI:10.1016/j.applthermaleng.2004.10.005**.

[13] Assis, E., Katsman, L., Ziskind, G., Letan, R. (2007). Numerical and experimental study of melting in a spherical shell. *International Journal of Heat and Mass Transfer*, vol. 50, no. 9-10, p. 1790-1804, **DOI:10.1016/j.ijheatmasstransfer.2006.10.007**.

[14] Ismail, K.A.R., Da Silva, M.G.E. (2003). Numerical solution of the phase change problem around a horizontal cylinder in the presence of natural convection in the melt region. I*nternational Journal of Heat and Mass Transfer*, vol. 46, no. 10, p. 1791-1799, **DOI:10.1016/S0017-9310(02)00487-8**.

[15] Lamberg, P. (2004). Approximate analytical model for two-phase solidification problem in a finned phase-change material storage. *Applied Energy*, vol. 77, no. 2, p.131-152, **DOI:10.1016/S0306-2619(03)00106-5**.

[16] Kittl, J.A., Reitano, R., Aziz, M.J., Brunco, D.P, Thompson, M.O. (1993). Time-resolved temperature measurements during rapid solidification of Si-As alloys induced by pulsed-laser melting. *Journal of Applied Physics*, vol. 73, no. 8, p. 3725-3733, **DOI:10.1063/1.352903**.

[17] Queheillallt, D.T., Lu, Y., Wadeley, H.N.G. (1997). Laser ultrasonic studies of solid-liquid interface. *Journal of the Acoustical Society of America*, vol. 101, no. 2, p. 843-853, **DOI:10.1121/1.418042**.

[18] Kakimoto, K., Eguchi, M., Watanabe, H. Hibiya, T. (1988). In-situ observation of solid-liquid interface shape by X-ray radiography during silicon single crystal growth. *Journal of Crystal Growth*, vol. 91, no. 4, p. 509-514, **DOI:10.1016/0022-0248(88)90118-2**.

[19] Parker, R.L., Manning, J.R., Peterson, N.C. (1985). Application of pulse-echo ultrasonics to locate the solid/liquid interface during solidification and melting of steel and other metals. Journal of AppliedPhysics, vol. 58, no. 11, p. 4150-4164, **DOI:10.1063/1.335547**.

[20] Burhan, D., Ihara, I., Seda, Y. (2005). In situ observations of solidification and melting of aluminum alloy using ultrasonic waveguide sensor. *Materials Transactions*, vol. 46, no. 9, p. 2107-2113, **DOI:10.2320/matertrans.46.2107**.

[21] Wadley, H.N.G., Dharmasena, K.P. (1997). Method for liquid-solid interface shape and location discrimination during eddy current sensing of Bridgman growth. *Journal of Crystal Growth*, vol. 172, no. 3-4, p. 313-322, **DOI:10.1016/S0022-0248(96)00496-4**.

[22] Verhoeven, J.D., Gibson, E.D. (1969). A thermoelectric probe for measuring solid-liquid interface velocities and temperatures. *Journal of Crystal Growth*, vol. 5, no. 4, p. 235-238, **DOI:10.1016/0022-0248(69)90050-5**.

[23] Moravčík, R., Štefániková, M., Čička, R., Čaplovič, L., Kocúrová, K., Šturm, R. (2012).Phase transformations in high alloy cold work tool steel. *Strojniški vestnik - Journal of Mechanical Engineering*, vol. 58, no. 12, p. 709-715, **DOI:10.5545/sv-jme.2012.531**.

[24] Steiner Petrovič, D., Šturm, R. (2014). Fine-structured morphology of a silicon steel sheet after laser surface alloying of sb powder. *Strojniški vestnik - Journal of Mechanical Engineering*, vol. 60, no. 1, p. 5-11, **DOI:10.5545/sv-jme.2013.1347**.

[25] Hriberšek, M., Šajn, V., Pušavec, F., Rech. J., Kopač, J. (2016). The procedure of solving the inverse problem for determining surface heat transfer coefficient between liquefied nitrogen and Inconel 718 workpiece in cryogenic machining. *Strojniški vestnik - Journal of Mechanical Engineering*, vol. 62, no. 6, p. 331-339, **DOI:10.5545/sv-jme.2016.3572**.

[26] Alifanov, O.M., Mikhailov, V.V. (1978). Solution of the non-linear inverse thermal conductivity by the iteration method, Journal of Engineering Physics, (Translated from Inzhenerno-Fizicheskii Zhurnal, vol. 35, no. 6, p. 1123-1129), **DOI:10.1007/BF01104861**.

[27] Tikhonov, A., Arsenine, V.Y. (1977). *Solution of Ill-Posed Problems*, Wiley, New York.

Strojniški vestnik - Journal of Mechanical Engineering 63(2017)2, 111-118
DOI:10.5545/sv-jme.2016.3589
Original Scientific Paper
Received for review: 2016-03-17
Received revised form: 2016-08-15
Accepted for publication: 2016-12-16

Work Hardening of Non-Axisymmetric Die-Less Spinning

Zhen Jia[1] – Zhiren Han[1,*] – Baoming Liu[1] – Yong Xiao[2]

[1] Shenyang Aerospace University, Key Lab of Fundamental Science for National Defence of Aeronautical Digital Manufacturing Process, China
[2] Northwestern Polytechnical University, School of Mechanical Engineering, China

Non-axisymmetric shell parts are widely used in the fields of aviation, aerospace and automobiles. Because of good flexibility, short production preparation period and low cost, die-less spinning has the advantages in processing those parts. However, the special work-hardening distribution being caused by its processing technology will affect the performance of these parts. Therefore, the work-hardening of non-axisymmetric die-less spinning is studied through experiments and by using the finite element method (FEM). The law of "smaller half cone angle (HCA) with bigger work-hardening" is found by testing the surface hardness of the spun workpieces. Microstructure observation and theoretical analyses are adopted to reveal the law. The reason for that is that the roller causes greater plastic strain inhomogeneity in the smaller HCA-forming process. It is also found that the working condition with the largest HCA difference has the biggest work-hardening difference and the maximum hardness difference can be 15 %.

Keywords: non-axisymmetric spinning, work-hardening status, die-less spinning, HCA, FEM, strain

Highlights

- *Because of the effect of the special work-hardening distribution being caused by the non-axisymmetric die-less spinning process on the strength of non-axisymmetric shell parts, the work-hardening of non-axisymmetric die-less spinning is studied through experiments and by using FEM.*
- *Three working conditions of non-axisymmetric die-less spinning experiments are carried out with the deduced roller path. The work-hardening distributions of the workpieces are obtained via the surface hardness testing.*
- *The law "smaller half cone angle (HCA) with bigger work-hardening" is found and can be applied to the HCAs on either one or several workpieces.*
- *The reason for the law is that the roller causes greater plastic strain inhomogeneity in the smaller HCA forming process.*

0 INTRODUCTION

Spinning, a kind of metal forming technique, is commonly known as a process for transforming flat sheet metal blanks, usually with axisymmetric profiles, into hollow shapes by a tool which forces a blank onto a mandrel. Due to its flexible, stable, and near net-shape forming for axisymmetric parts, spinning is widely used in aerospace, chemical products, and special materials parts processing **[1]** to **[3]**. Previously, shell parts with non-axisymmetric shapes were mainly manufactured by welding two stamping parts whose shapes are the half of the non-axisymmetric parts in the traditional process, such as automotive catalytic converters (see Fig. 1). Recently, with the development of the spinning technology, the non-axisymmetric tubular parts can be manufactured. Xia et al. **[4]** and **[5]** and Wia **[6]** developed a spinning method to produce a non-axisymmetric tube. The whole strength of the parts is significantly improved by the integrated forming method of spinning. In their investigations, the working principle, forming characteristics and deformation mechanism of the non-axisymmetric tube spinning is discussed by adopting the finite element method (FEM) and experiments. It shows that the distributions of strain, stress and thickness reduction of the non-axisymmetric tubular spun workpieces are non-axisymmetric and uneven. Awiszus and Härtel **[7]** and Härtel and Laue **[8]** investigate the spinning process for making non-circular parts by adopting modelling and experiment methods, and the process optimization has been proposed. Music and Allwood **[9]** put forward a flexible asymmetric spinning method by replacing the asymmetric mandrel with three rollers which can be controlled on a seven-axis machine. Sugita and Arai **[10]** investigate the effect of different parameters of the pass set on the formability in synchronous multi-pass spinning. The above-mentioned research results have laid a solid foundation for the asymmetric and non-circular cross-section spinning technology, and indicate that the uneven status of the force and the deformation forming during the non-axisymmetric or noncircular spinning processes will lead to different microstructures and thus cause different work-hardening states. It is mainly because that the work-hardening behaviour of the parts is closely related to the microstructure. Therefore, the microstructure evolution during the spinning process has been studied by many scholars in recent years.

*Corr. Author's Address: Shenyang Aerospace University, 38 Daoyi South Avenue, Daoyi Development District, Shenyang, China, Hanren888@163.com

Zhan et al. [11] investigate the influence of the heating temperature on the hot shear spinning of TA15 alloy and conclude that the non-uniform deformation along the thickness direction leads to a non-uniform microstructure. The effect of the shear spinning on the deformation behavior and the microstructure of $AlMg_6Mn$ alloy was investigated by Radović et al. [12]. Yan et al. [13] and Xia et al. [14] and [15] investigated the effect of power spinning on the microstructure of the tubular part. They conclude that the average grain size of the ferrite can be reduced to 500 nm from the initial one of 50 μm after the stagger spinning.

Die-less spinning means the parts are spun from a sheet blank without a mandrel die, which can enhance the cost reduction and shorten the production cycle for the non-axisymmetric spinning process. However, the force state of the process will be different from the one with the mandrel due to the lack of support to the blank. And this may result in special microstructure of the alloy and cause different work-hardening states which will reflect the strength [16] on the surface of the non-axisymmetric cone. Therefore, the work-hardening state of the non-axisymmetric die-less spinning is investigated in this paper.

Fig. 1. *Schematic diagram of automotive catalytic converter*

1 NON-AXISYMMETRIC SPINNING

Fig. 2 shows the geometric model of a non-axisymmetric cone. It can be seen that the cone is made up of countless thin circular sheets; the half cone angles (HCA) seen from the side view are different, and this means the lower cross section is an eccentric circle relative to the upper one; the relative eccentricity increases gradually with the increase of the height of the cone. The process of shear spinning is that the sheet blank rotates with the spindle and tail cap. The roller moves along a specific path and contacts the blank first and then forces the blank to form the desired shape without a mandrel. Based on the above conditions, a non-axisymmetric spinning is proposed: When the blank rotates a small angle $\Delta\theta$, the roller goes down from the upper sheet to the lower one along the axial direction. At the same time, the roller moves far away from the rotational centre along the radial direction, and moves towards the rotational centre after 90° rotated by the blank. The roller goes straight down in the axial direction and switches to the radial direction in every 180° of the rotation cycle. The radius of the circle in each sheet increases from top to bottom. Thus, a spiral trajectory with a gradually expanding radius is used for the roller path, and its mathematical expression (deduced in [17]) is:

$$x = -0.5if\left(\frac{\Delta\theta}{360}\right)(\tan\alpha - \tan\gamma)\cos\theta + \\ + \sqrt{\left[R_0 + 0.5if\left(\frac{\Delta\theta}{360}\right)(\tan\alpha + \tan\gamma)\right]^2 - \\ -\left[0.5if\left(\frac{\Delta\theta}{360}\right)(\tan\alpha - \tan\gamma)\right]^2 \sin^2\theta}, \quad (1)$$

$$z = -if\left(\frac{\Delta\theta}{360}\right), \quad (2)$$

where x and z are the radial and axial coordinates of the roller path, respectively. R_0 is the initial radius of the cross section; α and γ are the co-angles of the maximum and minimum HCA (see Fig. 2) respectively; θ is the accumulation of $\Delta\theta$; f is the axial feed rate; and i, as a integer, is a global variable whenever the spindle rotates an angle increment $\Delta\theta$, and there is:

$$\theta = i\Delta\theta. \quad (3)$$

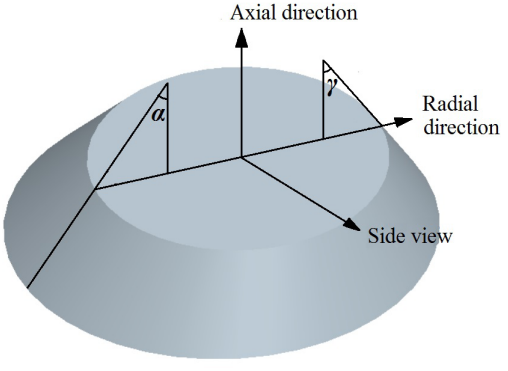

Fig. 2. *Geometric model of non-axisymmetric cone*

2 EXPERIMENT AND ANALYSES

2.1 Spinning Experiment

The working conditions of different HCAs in Table 1 are adopted for the spinning experiments. The material

of the disk blank is 6061-O aluminium alloy, and the radius and thickness of the blank are 120 mm and 1.2 mm, respectively. The initial radius R_0 is 25 mm. The diameter of the roller is 110 mm. The working radius of the roller is 2 mm. The angle between the rotation axis of the roller and the axial direction of the spinning system is 45°. The axial feed rate f is 0.3 mm/rev. The feed speed of the roller is 5000 mm/min. With the roller path equations, the non-axisymmetric spinning experiments are carried out on the PS-CNCSXY 5-axis spinning machine as shown in Fig. 3.

Table 1. *Working conditions of the non-axisymmetric spinning*

HCA	Working condition I	Working condition II	Working condition III
α [°]	45	60	60
γ [°]	30	30	45

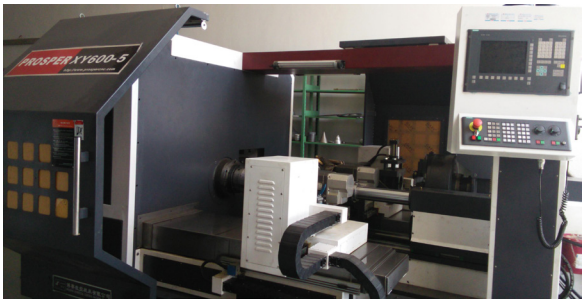

Fig. 3. *PS-CNCSXY 5-axis spinning machine*

The machine is a numerically-controlled (NC) one. It is driven by four servomotors (GS3050Y-NP2) which control the movements of the two rollers along axial and radial directions on both sides of the spindle, and the control accuracy can be 0.001 mm. The roller path is executed by the combination motion of the spindle rotation and roller feed. The rotational velocity of the workpiece must match the movement of the roller through the NC system of the spinning machine. The experiment results are shown in Fig. 4.

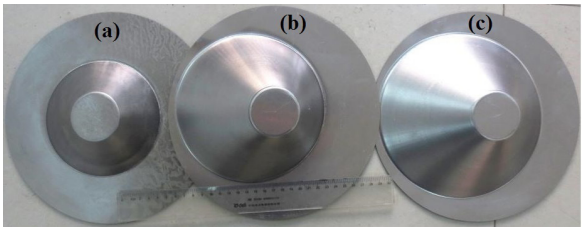

Fig. 4. *Spun workpieces; a) working condition I; b) working condition II; c) working condition III*

2.2 Work-Hardening Distributions

Three longitude directions (0°, 90° and 180°) and three latitudes (top, middle and bottom) are set on the spun workpieces as shown in Fig. 5. The intersections of the longitude lines and latitude lines can then be defined as 9 positions. In these positions, 9 specimens with the length and width 12 mm × 8 mm are cut down from the workpiece (see Fig. 5). Then the hardness tests were carried out at three points, which are selected randomly on the surface of the specimens with the HVS-50 Vickers hardness tester (Fig. 6).

The average value of the hardness of the three measuring positions on each specimen is taken as the

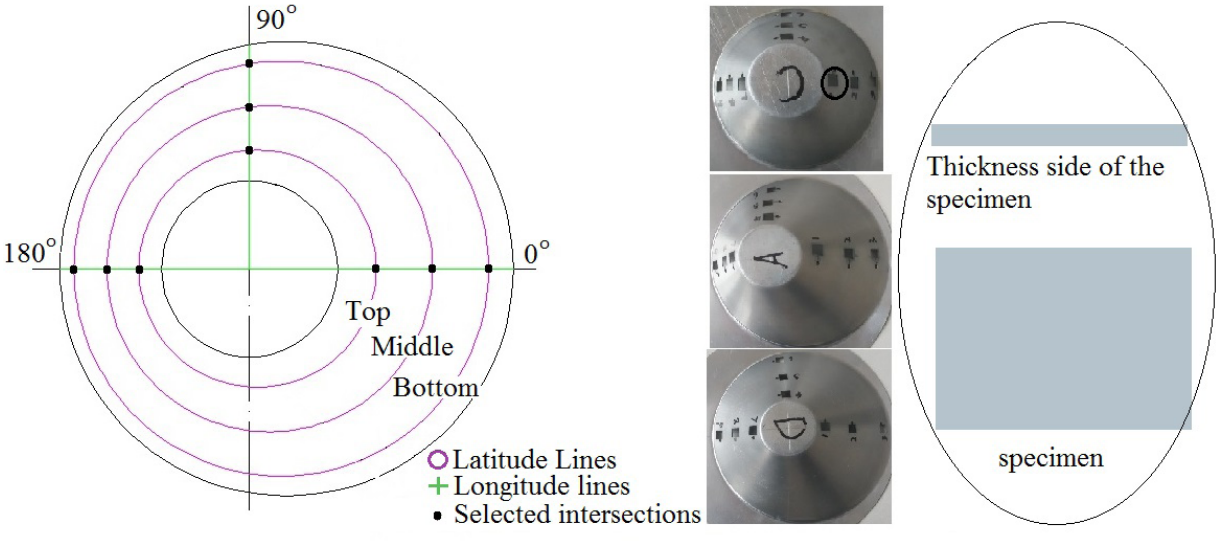

Fig. 5. *Positions and shapes of the specimens*

hardness of the selected intersection (see Fig. 5), and the hardness of all the intersections is shown in Fig. 7. It can be found that small differences in the hardness exist in the specimens with the same HCA. However, there is an obvious tendency that the material with smaller HCA has greater surface hardness. This means the work-hardening distribution of non-axisymmetric die-less spinning is uneven, and bigger work-hardening appears in the position with smaller HCA.

Fig. 6. *HVS-50 Vickers hardness tester*

The hardness of the parts is closely related to the microstructure. The microstructure of the specimens that were used for the hardness test is thus observed with an optical microscope. First, the thickness sides (Fig. 5) of the specimens are ground and polished. Then, all the smooth surfaces are corroded through the electrolysis method. Finally, the metallographic photos of the specimens are obtained as shown in Fig. 8. It can be found that the grain boundary of the workpiece is broken after two plastic deformations (one is the rolling aluminium alloy plate and the other is the spinning process) and many precipitates emerge. According to [18], the grain of 6061 aluminium alloy will be refined to a very small one and its boundary will also be broken after large plastic deformation. At the same time, the disorganized precipitates seriously hinder the observation of dislocations. Therefore, the metallographic method of the workpieces spun from the 6061 aluminium alloy sheet blank is not suitable for revealing work-hardening. However, the differences of the microstructure can be reflected by the macroscopic states of the stress and strain. Therefore, the finite element method is adopted to analyse the essence of the work-hardening distribution of the non-axisymmetric die-less spinning (the metal with smaller HCA has higher surface hardness).

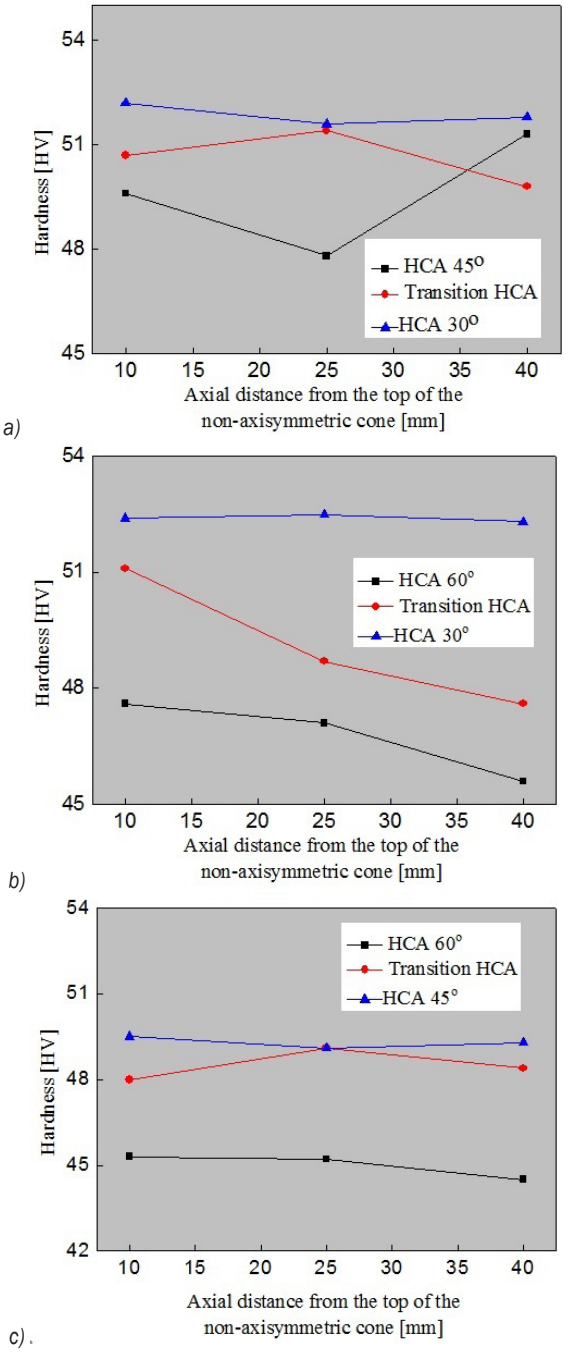

Fig. 7. *Hardness distributions of the workpieces under the three working conditions; a) working condition I; b) working condition II; c) working condition III*

2.3 Establishment of the Finite Element Model

In order to simulate the non-axisymmetric die-less spinning process, a FEM must first be established. The movement relationship between the roller and the workpiece is the main boundary condition of the

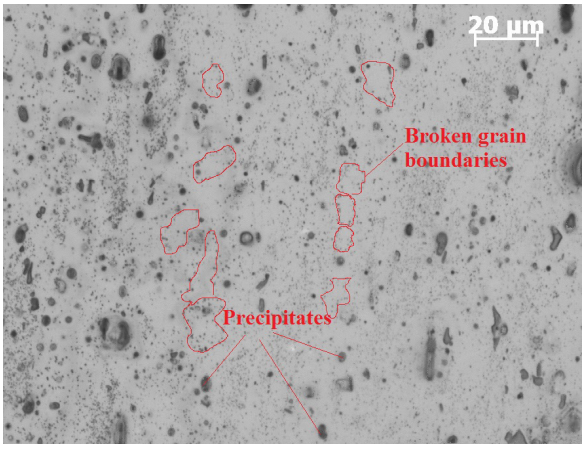

Fig. 8. *Metallographic photo of the specimen*

model, and it is set in agreement with the experiments by using Eqs. (1) to (3). Then the three-dimensional geometric models of disk blank, tail cap, spindle, and roller are established and assembled in the ABAQUS finite element software (see Fig. 9). All the geometric models are meshed. The roller, tail cap and spindle are arranged in rigid bodies. By considering that there is no deformation happening to the part that is clamped by the tail cap and the spindle, this part of the blank is also constrained into a rigid body. Furthermore, it is driven to rotate with the spindle synchronously. The suspended part of the disk blank is set into a deformable body and meshed with an 8-node linear brick, reduced integration, hourglass control element (C3D8R) for the accurate calculation for the stress-strain. The maximum length of the mesh is 3 mm, and the minimum one is 1 mm. The rotation centre of the roller can move in the plane *X-Z* of the spinning coordinate system (see Fig. 9), and the roller is also driven to rotate around its rotation centre by the friction from the blank. The friction coefficient is set to the value of 0.15 according to the experience value of oil lubrication. The other spinning conditions of the FEM are set up the same as the experiments.

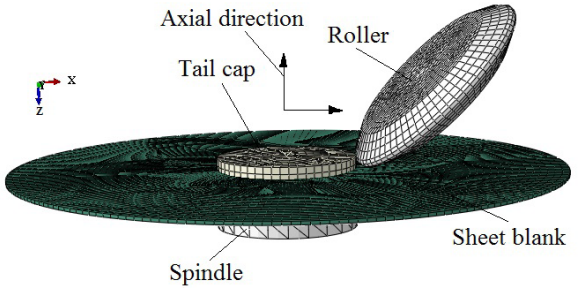

Fig. 9. *Assembly diagram of the FEM for the non-axisymmetric die-less spinning*

The material of the blank is 6061 aluminium alloy and its elastic modulus is 67000 MPa, Poisson ratio is 0.33, yield strength is 51.59 MPa, and tensile strength is 146.12 MPa. The constitutive relation of the material is obtained from [4]:

$$\sigma_f = 234\varepsilon^{0.26}, \tag{4}$$

where, σ_f is the flow stress and ε is the true strain.

3 SIMULATION RESULTS

The morphology of modelling result, in comparison with the experimental one, is shown in Fig. 10. It shows that the simulated results are well consistent with the experimental ones. A further contrast of the HCAs is carried out, as shown in Table 2. It can be found that all the HCAs appear to be close to the theoretical size, and the maximum error occurs in the γ of working condition II from the simulation; it can reach 16.3 %. The maximum deviation of the HCAs between the experimental and simulation results is no more than 11 %. In addition, the simulated wall thickness distribution is compared with the experimental one, and the measuring positions in the working condition I are shown in Fig. 11 together with the ones in the working conditions II and III (the measuring positions also distributed evenly along the HCA direction in the other working conditions). All the measurements of the wall thickness are listed in Table 3. It shows that the simulations agree well with the experiments and the maximum deviation is within 15.1% in the three working conditions. This indicates that the FEM for the non-axisymmetric die-less spinning is considered credible.

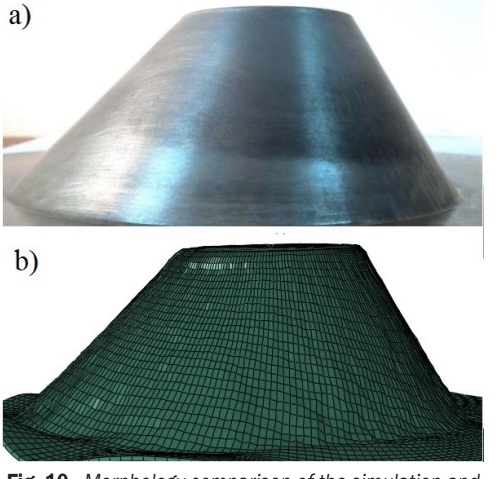

Fig. 10. *Morphology comparison of the simulation and experimental results in working condition I; a) Experimental result; b) Simulation result*

Table 2. *HCAs of the simulation and experimental results*

	HCA	Working condition		
		I	II	III
Experimental result	α [°]	45.9	57.4	59.1
	γ [°]	31.5	31.4	45.6
Simulation result	α [°]	47.7	60.4	62.5
	γ [°]	32.7	34.9	46.9

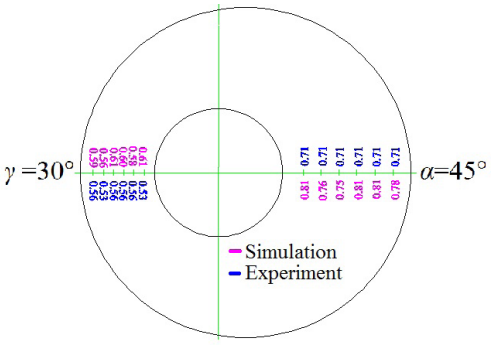

Fig. 11. *Measuring positions of the wall thickness*

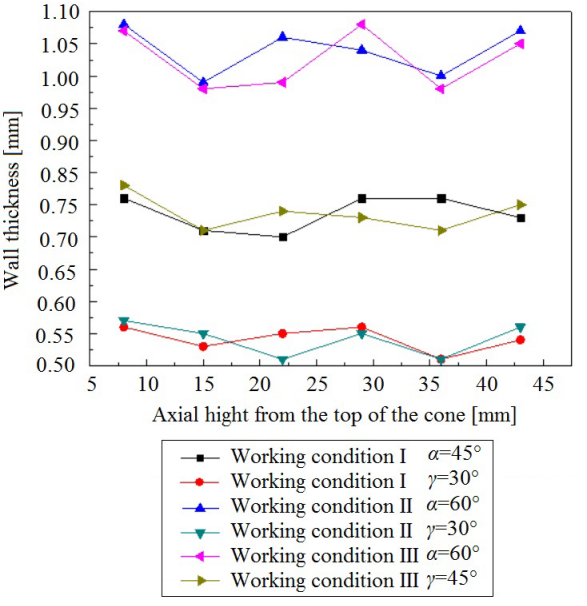

Fig. 12. *Comparison of the wall thickness distributions in the three working conditions*

Table 3. *Measurements of the wall thickness [mm]*

Axial height [mm]	Working condition					
	I		II		III	
	α=45°	γ=30°	α=60°	γ=30°	α=60°	γ=45°
8	0.71	0.53	0.98	0.57	1	0.73
15	0.71	0.56	0.96	0.57	0.98	0.73
22	0.71	0.56	0.99	0.56	0.98	0.73
29	0.71	0.56	0.97	0.57	1	0.72
36	0.71	0.53	0.97	0.56	0.98	0.72
43	0.71	0.56	0.97	0.56	0.98	0.72

4 DISCUSSION

The wall thickness distribution of the three working conditions from the simulation are illustrated in Fig. 12. Tensile stress increases with the decreasing of HCA. However, the wall thickness becomes thinner with the decreasing of HCA. This also means the smaller HCA causes larger plastic strain.

Fig. 13 shows the equivalent strain field on the workpiece at the spinning times of 24 s, 48 s, and 74 s. It can be found that the deformation is obviously uniform in the non-axisymmetric spinning process, and the uneven degree of the deformation increases with the spinning process. When the plastic strain achieves maximum with the smallest HCA in working condition I and II, the hardness is precisely the biggest one (51.9 HV, the average value of the hardness with the same HCA (Working condition I, γ = 30°); 52.4 HV, the average value of the hardness with the same HCA (Working condition II, γ = 30°). In order to reveal "smaller HCA with bigger work-hardening", the movement of the non-axisymmetric spinning is resolved by steps. The non-axisymmetric cone can be seen as an aggregate of numerous sheets with the eccentric circular cross-section, and it is spun layer by layer. Fig. 14 displays the roller path between two layers. Moreover, it is defined that as the roller starts from the upper layer to the lower one, the workpiece rotates 360°. In the first 180°, the roller moves far away from the rotation centre in the radial direction and the bigger HCA α is formed; then the roller moves close to the rotation centre at the radial direction in the next 180° as it gets down to the lower layer and the smaller HCA γ being formed. In the forming process of γ, the blank suffers increasing pressure from the roller and this leads to more uniform deformation. WANG et al. [19] point out that the non-uniformity of plastic strain will directly affect the orientation of the dislocation movement, and promote the formation of the deformation band, which leads to the work-hardening of the material. Therefore, the greater work-hardening occurs at the position with smaller HCA.

The largest difference of the HCA exists in working condition II, so there is the most uneven deformation on the workpiece of it, and it also has the biggest surface hardness difference (the maximum hardness differences of working condition I, II and III are 9.2%, 15.1% and 11.2%). This interesting

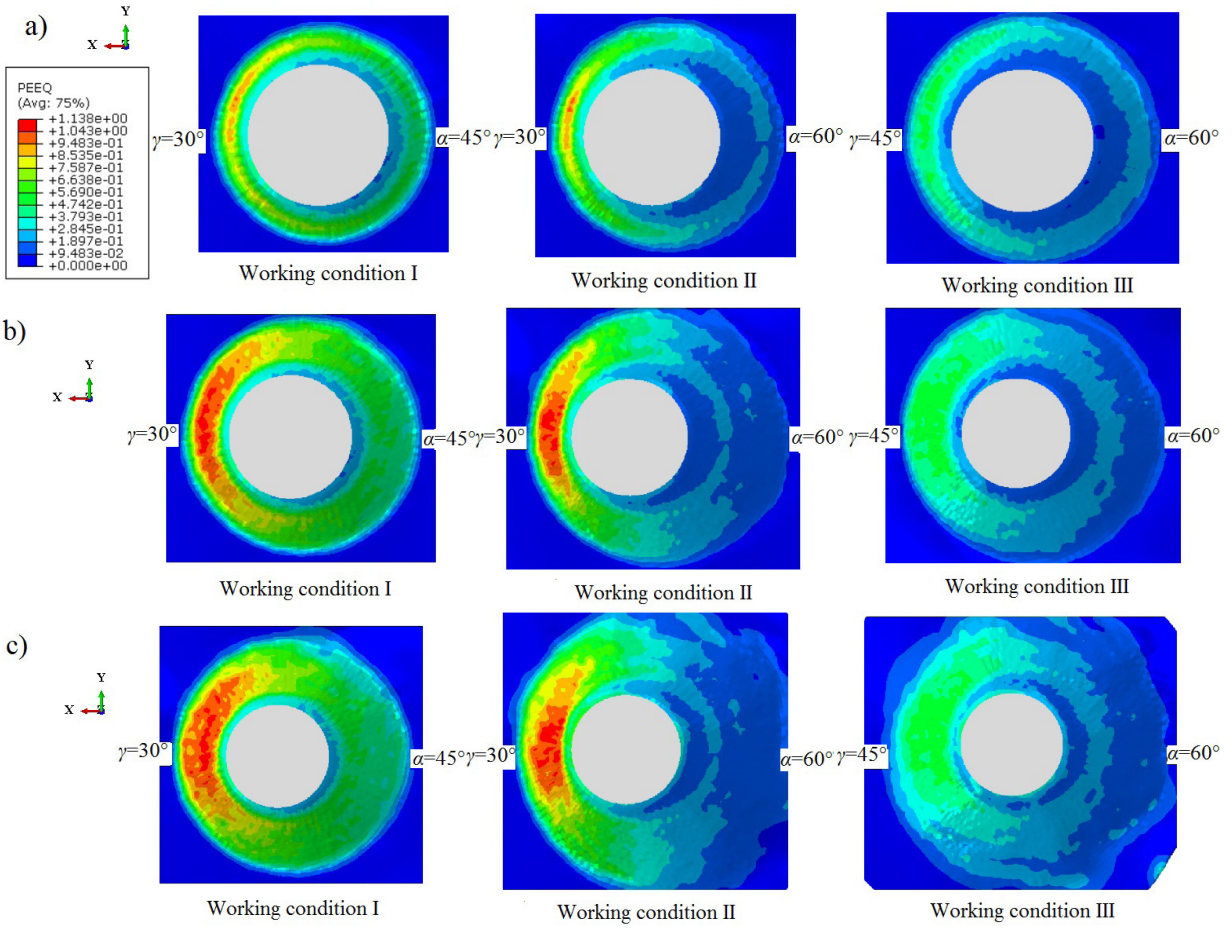

Fig. 13. *Equivalent strain field of the non-axisymmetric die-less spinning; a) spinning time 24 s; b) spinning time 48 s; c) spinning time 74 s*

phenomenon also confirms the above analysis: greater work-hardening is caused by greater non-uniformity of deformation.

5 CONCLUSIONS

Three working conditions of non-axisymmetric die-less spinning experiments are carried out, and the work-hardening distributions of the workpieces are obtained by the surface hardness testing. It is found that the work-hardening distribution of non-axisymmetric die-less spinning is uneven, and bigger work-hardening appears on the position with smaller HCA. The reason for "smaller HCA with bigger work-hardening" is revealed through finite element method: when the smaller HCA is formed, the deformation is more uniform due to the increasing pressure from the roller. The working condition with the largest HCA difference has the biggest wok-hardening difference, and the maximum hardness difference can reach 15 %.

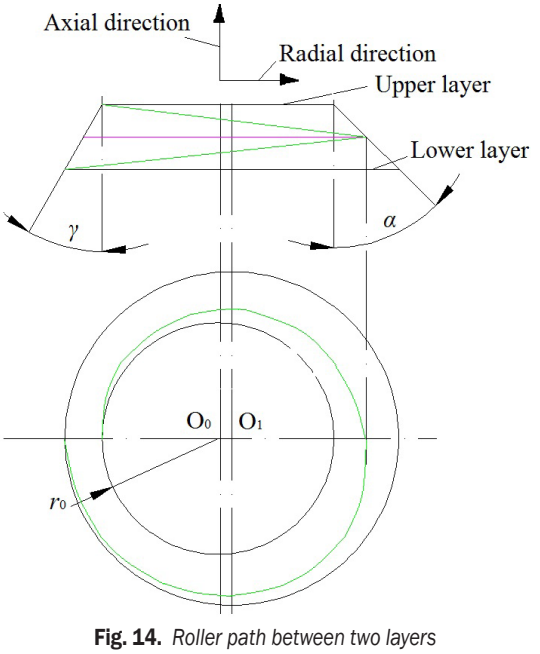

Fig. 14. *Roller path between two layers*

6 ACKNOWLEDGEMENTS

This work was financially supported by the Natural Science Foundation of Liaoning Province, China (No. 201602558), and authors wish to express their gratitude.

7 REFERENCES

[1] Zhan, M., Yang, H., Guo, J., Wang, X.X. (2015). Review on hot spinning for difficult-to-deform lightweight metals. Transactions of Nonferrous Metals Society of China, vol. 25, no. 6, p. 1732-1743, **DOI:10.1016/S1003-6326(15)63778-5**.

[2] Xia, Q., Xiao, G., Long, H., Cheng, X., Sheng, X. (2014). A review of process advancement of novel metal spinning. *International Journal of Machine Tools and Manufacture*, vol. 85, p. 100-121, **DOI:10.1016/j.ijmachtools.2014.-05.005**.

[3] Han, D., Yang, H., Zhang, L.W., Mou, S.Z., Yang, Y.T., Xiao-Xing, H.E. (2010). Effects of heat treatment and spinning temperature on microstructure and properties of 3A21 aluminum alloy. *Journal of Solid Rocket Technology*, vol. 33, no. 2, p. 225-228. (in Chinese)

[4] Xia, Q.X., Xie, S.W., Huo, Y.L., Ruan, F. (2008). Numerical simulation and experimental research on the multi-pass neck-spinning of non-axisymmetric offset tube. *Journal of Materials Processing Technology*, vol. 206, no.1-3, p. 500-508, **DOI:1016/j.jmatprotec.2007.12.066**.

[5] Xia, Q.X., Cheng, X.Q., Hu, Y., Ruan, F. (2006). Finite element simulation and experimental investigation on the forming forces of 3D non-axisymmetrical tubes spinning. *International Journal of Mechanical Sciences*, vol. 48, no. 7, p. 726-735, **DOI:10.1016/j.ijmecsci.2006.01.014**.

[6] Xia, Q.X. (2004). Investigation on the mechanism of the spinning technology of the 3D non-axisymmetric parts. *Chinese Journal of Mechanical Engineering*, vol. 40, vo. 2, p. 153-156, **DOI:10.3901/JME.2004.02.153**. (in Chinese)

[7] Awiszus, B., Härtel, S. (2011). Numerical simulation of non-circular spinning: a rotationally non-symmetric spinning process. *Production Engineering*, vol. 5, no. 6, p. 605-612, **DOI:10.1007/s11740-011-0335-9**.

[8] Härtel, S., Laue, R. (2015). An optimization approach in non-circular spinning. *Journal of Materials Processing Technology*, vol. 229, p. 417-430, **DOI:10.1016/j.jmatprotec.2015.09.-003**.

[9] Music, O., Allwood, J.M. (2011). Flexible asymmetric spinning. *CIRP Annals - Manufacturing Technology*, vol. 60, no. 1, p. 319-322, **DOI: 10.1016/j.cirp.2011.03.136**.

[10] Sugita, Y., Arai, H. (2015). Formability in synchronous multipass spinning using simple pass set. *Journal of Materials Processing Technology*, vol. 217, p. 336-344, **DOI:10.1016/j.jmatprotec.2014.11.017**.

[11] Zhan, M., Wang, Q.L., Han, D., Yang, H. (2013). Geometric precision and microstructure evolution of TA15 alloy by hot shear spinning. *Transactions of Nonferrous Metals Society of China*, vol. 23, no. 6, p. 1617-1627, **DOI:10.1016/S1003-6326(13)-62639-4**.

[12] Radović, L., Nikačević, M., Jordović, B. (2012). Deformation behaviour and microstructure evolution of AlMg6Mn alloy during shear spinning. *Transactions of Nonferrous Metals Society of China*, vol. 22, no. 5, p. 991-1000, **DOI:10.1016/S1003-6326(11)61275-2**.

[13] Yang, B.J., Xia, Q.X., Cheng, X.Q. (2012). Investigation on fabrication of ultrafine-grain tubular part through power spinning. Journal of Functional Materials, no. 2, p. 266-269. (in Chinese)

[14] Xia, Q., Xiao, G., Long, H., Cheng, X., Yang, B. (2014). A study of manufacturing tubes with nano/ultrafine grain structure by stagger spinning. *Materials and Design*, vol. 59, p. 516-523, **DOI:10.1016/j.matdes.2014.03.012**.

[15] Xiao, G., Xia, Q., Cheng, X., Zhou, Y. (2015). Research on the grain refinement method of cylindrical parts by power spinning. *The International Journal of Advanced Manufacturing Technology*, vol. 78, no. 5, p. 971-979, **DOI:10.1007/s00170-014-6686-6**.

[16] Lu, J., Zeng, X., Ding, W. (2008). The Hall–Petch relationship. *Light Metals*, vol. 8, p. 59-64. (in Chinese)

[17] Han, Z.R., Xu, Q., Jia, Z., Li, X.B. (2015). Experimental research on oblique cone die-less shear spinning. *Proceedings of the Institution of Mechanical Engineers, Part B: Journal of Engineering Manufacture*, vol. 78, no. 23, p. 11772-11782, **DOI:10.1177/0954405415586607**.

[18] Luo, X., Shi, Q.N., Liu, S.H., Chen, Y.L., Wang, X.Q. (2009). Study on microstructure and properties of ultra-fine-grain 6061 aluminium alloy. *Transactions of Materials and Heat Treatment*, vol. 30, no. 3, p. 71-75. (in Chinese)

[19] Wang, X., Jiang, C., Han, X. (2015). Plastic strain heterogeneity and work hardening of Ni single crystals. *Acta Metallurgica Sinica*, vol. 51, no. 12, p. 1457-1464. (in Chinese)

Strojniški vestnik - Journal of Mechanical Engineering 63(2017)2, 119-128

DOI:10.5545/sv-jme.2016.4014 Original Scientific Paper
Received for review: 2016-08-30
Received revised form: 2016-10-20
Accepted for publication: 2016-11-22

MHD Boundary Layer Behaviour over a Moving Surface in a Nanofluid under the Influence of Convective Boundary Conditions

Mohamed Abdel-wahed[1,*] – Tarek Emam[2,3]
[1] Benha University, Faculty of Engineering at Benha, Egypt
[2] Ain Shams University, Faculty of Science, Egypt
[3] University of Jeddah, Faculty of Science and Arts, Saudi Arabia

The present work provides an analysis of the hydro-magnetic nanofluid boundary layer over a moving surface with variable thickness in the presence of nonlinear thermal radiation and convective boundary conditions. The governing partial differential equations system that describes the problem is converted to a system of ordinary differential equations by the similarity transformation method; such a system is solved numerically. The velocity, temperature, and nanoparticle concentration of the boundary layer are plotted and investigated in details. Moreover, the surface skin friction, rate of heat and mass transfer are deduced and explained in detail.
Keywords: Nanofluids, MHD flow, convective conditions, non-linear thermal radiation

Highlights
- *The non-linear Rosseland thermal radiation clearly affects the thermal and concentration boundary layers.*
- *The surface shear stress of the convex outer shape surface (n <1) is higher than that of the concave outer shape surface (n > 1).*
- *The presence of convective conditions decreases the surface heat flux as well as the mass flux.*

0 INTRODUCTION

Choi **[1]** has suggested the injection of nano-size particles into regular fluids, such as water and oil. He has proved experimentally that the injection of these particles improves the thermal conductivity of the fluid. This conclusion has opened the way to use these new fluids in chemical engineering, mechanical engineering, medicine, and many other fields.

Industrial applications of nanofluids, such as cooling processes, paper production, glass blowing, plastic extrusion, and wire drawing. are modeled by the mathematical model of boundary layer flow. In such a model, two important concepts are considered by researchers. The first concept is that the fluid and nanoparticles are assumed to be in thermal equilibrium, and no slip may occur between the fluid molecules and nanoparticles. Thus, the concentration of nanoparticles within the boundary layer is considered to be uniform. Taking this concept into consideration, Hamad **[2]** has found an analytical solution of natural convection flow of a nanofluid over a linearly streaching sheet in the presence of a magnetic field. Yacob et al. **[3]** numerically studied the problem of steady boundary layer shear flow over a stretching/shrinking surface with a convective boundary condition. Alsaedi et al. **[4]** have studied the effect of heat generation or absorption on stagnation point flow of a nanofluid over a surface with convective boundary conditions. Elbashbeshy et al. **[5]** deduced an exact solution for the nanofluid boundary layer over a moving surface subjected to the magnetic field in the presence of suction or injection. Abu Bakar et al. **[6]** have studied the slip effect and the convective boundary conditions on the boundary layer flow over a stretching sheet. Öztürk et al. **[7]** have investigated the effects of slip flow of nanofluid and constant heat flux on parallel heated plates.

The second concept is that there are several slip mechanisms that may occur due to Brownian motion and the thermophoresis phenomena so that the distribution of the nanoparticles within the regular fluid is considered to be non-uniform. This assumption has been investigated by Noghrehabadi et al. **[8]** as they studied the effect of the slip boundary conditions on the heat transfer characteristics of stretching sheet considering the effect of nanoparticles Brownian motion and the thermophoresis forces. Rahman et al. **[9]** investigated the dynamics of the natural convection boundary layer flow of a viscous incompressible Nanofluid over a nonlinear stretching sheet in the presence of a magnetic field with thermal radiation. Ramesh et al. **[10]** have investigated the influence of heat source or on a non-Newtonian fluid with nanoparticles over a stretching sheet. The effect of thermal radiation for a magnetohydrodynamic (MHD) boundary layer over a stretching sheet with convective boundary conditions was studied by Nadeem et al.

*Corr. Author's Address: Benha University, Cairo, Egypt, eng_moh_sayed@live.com

[11]. Chamkha et al. [12] investigated the influence of viscous dissipation and magnetic field on natural convection from a vertical plate in a non-Darcy porous medium saturated with a nanofluid. RamReddy et al. [13] examined the effect of Soret parameter on mixed convective flow along a vertical plate in a Nanofluid under a convective boundary condition. Ibrahim et al. [14] have considered the slip boundary conditions in velocity, temperature and concentration to study the boundary layer flow and heat transfer of a nanofluid. Hayat et al. [15] analysed the MHD boundary layer flow of nanofluid over a permeable stretching sheet with convective type boundary conditions for heat and mass transfer process.

All of the above studies have considered flat surfaces, whether vertical or horizontal, so the surface thickness is constant and not variable. Even though industrial applications may include cases of variable thickness surfaces, Fang et al. [16] studied the behaviour of the momentum boundary layer over a moving surface with variable thickness. Elbashbeshy et al. [17] extended the work of Fang to study the momentum and thermal boundary layer over a flatness plate in the presence of thermal radiation. In this work, the authors have assumed that no slip occurs between the fluid molecules and the nanoparticles, which is consistent with the first concept. Abdel-wahed et al. [18] extended the works of Fang and Elbashbeshy to investigate the boundary layer over a moving flatness plate in a nanofluid considering the effects of Brownian motion and the thermophoresis force with heat generation.

The objective of this work is to study the MHD boundary layer with convective boundary conditions over a flatness-moving surface taking the nanoparticles' Brownian motion and thermophoresis force into account. In addition, it is assumed that the boundary layer is subjected to non-linear Rosseland thermal radiation as modelled by Astreios et al. [19] and Abdel-wahed et al. [20].

1 METHODS

As shown in Fig. 1, we consider a surface with a flatness profile specified by $y=\delta\left(x+b\right)^{\frac{1-n}{2}}$ moving with nonlinear velocity $Uw\left(x\right)=a\left(x+b\right)^{n}$ along the x-axis. It is also assumed that the bottom surface of the plate is heated by a hot convection fluid of temperature T_w that provides a heat transfer coefficient h. Moreover, a magnetic field of strength $B\left(x\right)=B_0\left(x+b\right)^{\frac{n-1}{2}}$ and a thermal radiation of heat flux $q_r=-\left(\frac{4\sigma^*}{3\alpha^*}\right)\frac{\partial T^4}{\partial y}$ are applied normally to the surface and parallel to the y axis. The upper surface of the plate is subjected to a steady- laminar-incompressible viscous manofluid with temperature T and nanoparticle concentration C. The end of the boundary layer has an ambient temperature T_∞ and concentration C_∞.

It is noteworthy that n is the shape parameter. It is assumed that $n>-1$ in this work for the validity of the similarity variable and functions.

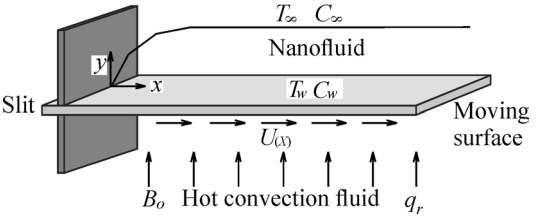

Fig. 1. *Physical model and coordinate system*

The governing boundary layer equations for such model with nonlinear Rosseland thermal radiation with convective boundary conditions [15] and [18] can be written as:

$$\frac{\partial u}{\partial x}+\frac{\partial v}{\partial y}=0, \tag{1}$$

$$u\frac{\partial u}{\partial x}+v\frac{\partial u}{\partial y}=\nu\frac{\partial^2 u}{\partial y^2}-\frac{\sigma B^2\left(x\right)}{\rho}u, \tag{2}$$

$$\left\{\begin{array}{c} u\dfrac{\partial T}{\partial x}+v\dfrac{\partial T}{\partial y}=\pm^{\times}\dfrac{\partial^2 T}{\partial y^2} \\ +\left(\dfrac{1}{\rho\, Cp}\right)\dfrac{\partial q_r}{\partial y} \\ +\tau\left[D_B\dfrac{\partial C}{\partial y}\dfrac{\partial T}{\partial y}+\dfrac{D_T}{T_\infty}\left(\dfrac{\partial T}{\partial y}\right)^2\right] \end{array}\right\}, \tag{3}$$

$$u\frac{\partial C}{\partial x}+v\frac{\partial C}{\partial y}=D_B\frac{\partial^2 C}{\partial y^2}+\frac{D_T}{T_\infty}\left(\frac{\partial^2 T}{\partial y^2}\right), \tag{4}$$

with boundary conditions:

$$\left\{\begin{array}{c} at\ \ y=\delta\left(x+b\right)^{\frac{1-n}{2}} \\ u=U_w, v=0,\ q_r-k\dfrac{\partial T}{\partial y}=h\ \left(T_w-T\right), \\ -D_m\dfrac{\partial C}{\partial y}=k_m\ \left(C_w-C\right) \\ as\ \ y\to\infty \\ u=0,\ \ v=0,\ \ T=T_\infty,\ \ C=C_\infty \end{array}\right\}. \tag{5}$$

2 SIMILARITY TRANSFORMATION & SOLUTION

We look for a similarity solution of Eqs. (1) to (4) with the boundary conditions, Eq. (5) using the following non-dimensional functions:

$$\left\{\begin{array}{c} \eta = y\sqrt{\left(\frac{n+1}{2}\right)\left(\frac{a\left(x+b\right)^{n-1}}{\upsilon}\right)} \\ \psi = \sqrt{\left(\frac{2}{n+1}\right)\left(x+b\right)^{n+1} a\upsilon}\, F\left(\eta\right) \\ T = \theta\left(\eta\right)\ \left[Tw - T\infty\right] + T\infty \\ C = \varphi\left(\eta\right)\ \left[Cw - C\infty\right] + C\infty \end{array}\right\}, \tag{6}$$

where η is the similarity variable, and ψ is the stream function which is defined as $u=\partial\psi/\partial y$ and $v=\partial\psi/\partial x$ which satisfies Eq. (1) and $\theta(\eta)$, $\phi(\eta)$ represent the dimensionless temperature and concentration, respectively.

Substituting Eq. (6) into Eqs. (2) to (4), one can obtain the following ordinary differential equations:

$$F''' + FF'' - \left(\tfrac{2n}{n+1}\right)F'^2 - \left(\tfrac{2}{n+1}\right)M\,F' = 0, \tag{7}$$

$$\left\{\begin{array}{c} 3\ \theta'' + R_d \dfrac{\left[\left(1+\left(\theta_w - 1\right)\ \theta\right)^4\right]''}{\left(\theta_w - 1\right)} \\ +3\,\mathrm{Pr}\ \left[F\theta' + Nb\theta'\varphi' + Nt\,\theta'^2\right] = 0 \end{array}\right\}, \tag{8}$$

$$\varphi'' + \frac{1}{2}Le\,F\varphi' + \left(\frac{Nt}{Nb}\right)\theta'' = 0, \tag{9}$$

with boundary conditions:

$$\left\{\begin{array}{c} F\left(\alpha\right) = \alpha\left(\tfrac{1-n}{1+n}\right),\ \ F'\left(\alpha\right) = 1 \\ \theta'\left(0\right) = -\left(\dfrac{3\ \gamma_1\ \gamma_2}{4\ \gamma_2\ R_d\ \theta_w^3 + 3\ \gamma_1\sqrt{\frac{1+n}{2}}}\right)\left[1-\theta\left(0\right)\right], \\ \varphi'\left(0\right) = -\gamma_3\ \left[1-\varphi\left(0\right)\right], \\ F'\left(\infty\right) = 0,\ \ \theta\left(\infty\right) = 0,\ \ \ \varphi\left(\infty\right) = 0 \end{array}\right\}. \tag{10}$$

Here primes denote differentiation with respect to η. The parameter $\alpha = \delta\sqrt{\frac{1+n}{2}\frac{a}{\upsilon}}$ is the surface thickness parameter. So $\eta = \alpha = \delta\sqrt{\frac{1+n}{2}\frac{a}{\upsilon}}$ indicates the plate surface. Upon defining $F\left(\eta\right) = f\left(\eta-\alpha\right) = f\left(\zeta\right)$, the similarity Eqs. (7) to (9) and the associated boundary conditions Eq. (10) become:

$$f''' + ff'' - \left(\frac{2n}{n+1}\right)f'^2 - \left(\frac{2}{n+1}\right)M\,f' = 0, \tag{11}$$

$$\left\{\begin{array}{c} \left[1+\dfrac{4Rd}{3}\left(1+\left(\theta_w-1\right)\ \theta\right)^3\right]\theta'' \\ +4Rd\left(\theta_w-1\right)\left[1+\left(\theta_w-1\right)\ \theta\right]^2\theta'^2 \\ +\mathrm{Pr}\left[f\theta' + Nb\theta'\varphi' + Nt\,\theta'^2\right] = 0 \end{array}\right\}, \tag{12}$$

$$\varphi'' + \frac{1}{2}Le\,f\varphi' + \left(\frac{Nt}{Nb}\right)\theta'' = 0, \tag{13}$$

with boundary conditions:

$$\left\{\begin{array}{c} f\left(0\right) = \alpha\left(\tfrac{1-n}{1+n}\right)\sqrt{\tfrac{1+n}{2}},\ \ f'\left(0\right) = 1, \\ \theta'\left(0\right) = -\left(\dfrac{3\ \gamma_1\ \gamma_2}{4\ \gamma_2\ Rd\ \theta_w^3 + 3\ \gamma_1\sqrt{\frac{1+n}{2}}}\right)\left[1-\theta\left(0\right)\right], \\ \varphi'\left(0\right) = -\gamma_3\ \left[1-\varphi\left(0\right)\right] \\ f'\left(\infty\right) = 0,\ \ \theta\left(\infty\right) = 0,\ \ \ \varphi\left(\infty\right) = 0 \end{array}\right\}. \tag{14}$$

Here primes denote differentiation with respect to (ζ).

It is worth mentioning that the value of the shape parameter n controls the boundary layer behaviour such that for $n=1$ the boundary condition Eq. (14) reduced to $f(0)=0$ which refers to an impermeable surface, while for $n<1$ the indicated boundary condition becomes $f(0)>0$ which refers to suction. Moreover, $n>-1$ corresponds to $f(0)<0$ which refers to injection.

The systems of Eqs. (11) to (13) together with the boundary conditions Eq. (14) are solved using a shooting method. In this process, it is necessary to choose a suitable finite value $\zeta\to\infty$, say ζ_∞. To solve the problem, it is required to have the values of $f''(0)$, $\theta'(0)$ and $\phi'(0)$, which are not given in the problem. Suitable guessing values for $f''(0)$, $\theta'(0)$ and $\phi'(0)$ are chosen and then integration is carried out. Comparing the calculated values of f', θ and ϕ at $\zeta=\zeta_{\max}\approx 10$ with the given boundary conditions $f'(\zeta_\infty)=0$, $\theta(\zeta_\infty)=0$ and $\phi(\zeta_\infty)=0$, the estimated values, $f''(0)$, $\theta'(0)$ and $\phi'(0)$ are adjusted. Then taking a series of values for $f''(0)$, $\theta'(0)$ and $\phi'(0)$ and applying the fourth order classical "Rung–Kutta method" with step-size $\Delta\eta=0.01$. However, the above procedure is repeated until the converged results within a tolerance limit of 10^{-6} are obtained.

The accuracy of the results is examined with the published work Hayat et al. [15].

Table 1. *Values of the fluid velocity, temperature, and nanoparticle concentration gradient at Nb=0.4, Nt=0.3, Le=2, Pr=1, M=0.4, γ_3=0.9 and $\gamma_1=\gamma_2=1$*

	$-f''(0)$	$-\theta'(0)$	$-\phi'(0)$
Hayat et al. [15]	1.459340	0.430912	0.318750
present	1.459339	0.430912	0.318750

3 RESULTS

The physical quantities that are interesting in this study are the skin friction coefficient, Nusselt and Sherwood numbers, which indicate physically to surface shear stress, rate of heat transfer, and rate of mass transfer respectively.

3.1 Surface Shear Stress

Surface shear stress can be defined as:

$$\left\{\begin{array}{c} \tau_w=\mu\left(\dfrac{\partial u}{\partial y}\right)_{y=\delta(x+b)^{\frac{1-n}{2}}} \\ =\mu\, U_w\sqrt{\dfrac{a}{\upsilon}\left(\frac{n+1}{2}\right)(x+b)^{n-1}}\, f''(0) \end{array}\right\}. \quad (15)$$

The skin friction coefficient is given by:

$$C_f=\frac{2\tau_w}{\rho U_w^2} \quad \text{i.e.} \quad 2\sqrt{\left(\tfrac{n+1}{2}\right)}f''(0)=\sqrt{R_e}\,C_{fx}. \quad (16)$$

3.2 Surface Heat Flux

Surface heat flux can be defined as:

$$\left\{\begin{array}{c} q_w=(q_r)_w-k\left(\dfrac{\partial T}{\partial y}\right)_{y=\delta(x+b)^{\frac{1-n}{2}}} \\ =-k(T_w-T_\infty)\sqrt{\left(\dfrac{n+1}{2}\right)\dfrac{a}{\upsilon}}(x+b)^{\frac{n-1}{2}}\theta'(0) \end{array}\right\}. \quad (17)$$

Since the Nusselt number is given by:

$$Nu=\frac{(x+b)q_w}{k(T_w-T_\infty)} \quad \text{i.e.}$$

$$Nu=-\left[\sqrt{\tfrac{n+1}{2}}\sqrt{R_e}+\frac{4Rd\theta_w^3}{3}\right]\theta'(0). \quad (18)$$

3.3 Surface Mass Flux

Surface mass flux can be defined as:

$$\left\{\begin{array}{c} q_m=-D_B\left(\dfrac{\partial C}{\partial y}\right)_{y=\delta(x+b)^{\frac{1-n}{2}}} \\ =-D_B(C_w-C_\infty)\sqrt{\left(\dfrac{n+1}{2}\right)\dfrac{a}{\upsilon}}(x+b)^{\frac{n-1}{2}}\varphi'(0) \end{array}\right\}. \quad (19)$$

Since the Sherwood number is given by:

$$Sh=\frac{(x+b)q_m}{D_B(C_w-C_\infty)} \quad \text{i.e.} \quad \frac{Sh}{\sqrt{R_e}}=-\sqrt{\tfrac{n+1}{2}}\varphi'(0). \quad (20)$$

4 DISCUSSION

The velocity, temperature and concentration profiles with the variation of all embedded parameters are shown in Figs. 2 to 18.

Figs. 2 to 4 present the influence of the thickness parameter α. It is observed that increasing of α leads to decreasing the velocity, temperature and concentration in the case of $n<1$ and the opposite is true for $n>1$ and no effect of this parameter on the boundary layer in the case of flat surface $n=0$. Moreover, one can observe that the surface temperature is higher in the case of $n>1$ than that in the case of $n<1$, and the influence of the thickness parameter on the temperature changes by changing the value of n such that in the case of $n>1$ the temperature Increases by the increase of the value of the thickness parameter and the opposite is true for $n<1$.

In addition, the nanoparticles concentration increases by increasing the thickness parameter in the case of $n>1$ and decreases in the case of $n<1$. Figs. 5 to 7 show the effect of magnetic field parameter on the boundary layer velocity, temperature, and concentration respectively.

It is clear that the increase of the magnetic parameter decreases the velocity and the opposite is true for the temperature and nanoparticles concentration.

The effect of non-linear thermal radiation appears in the dimensionless system through the radiation parameter Rd and temperature ratio parameter θ_w. The effects of the radiation parameter on the boundary layer temperature and concentration are exhibited in Figs. 8 and 9. It is clear that the effect of this parameter near the surface differs from its effect far from the surface such that the increasing of the radiation parameter near the surface decreases the temperature near the surface to a certain point at which the effect is reversed. In contrast, the increase of such parameter increases the temperature of the boundary layer.

In contrast, the effects of the temperature ratio on the boundary layer temperature and concentration are

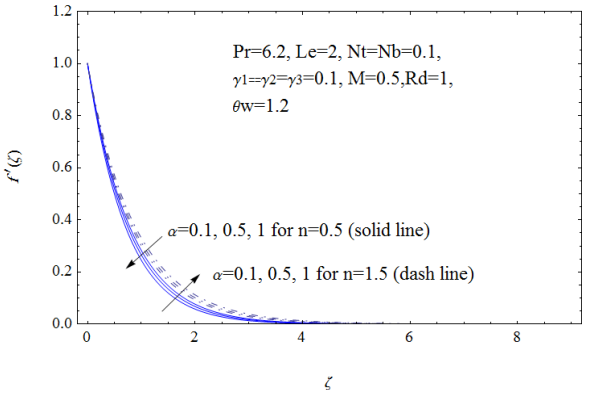

Fig. 2. *Influence of thickness parameter on the velocity*

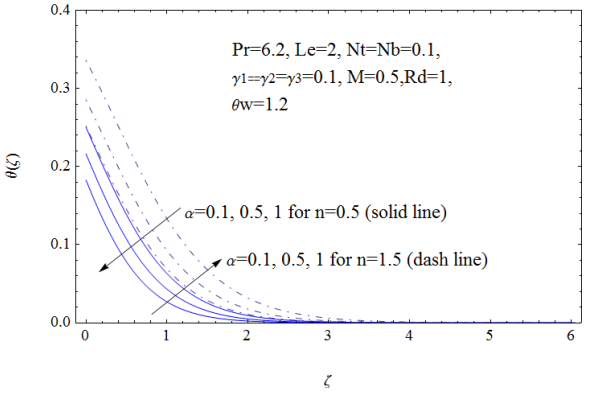

Fig. 3. *Influence of thickness parameter on the temperature*

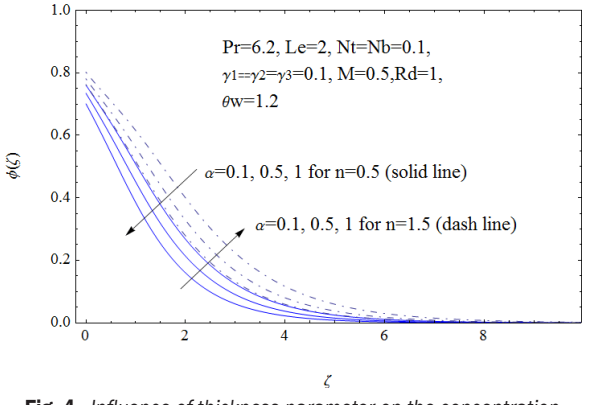

Fig. 4. *Influence of thickness parameter on the concentration*

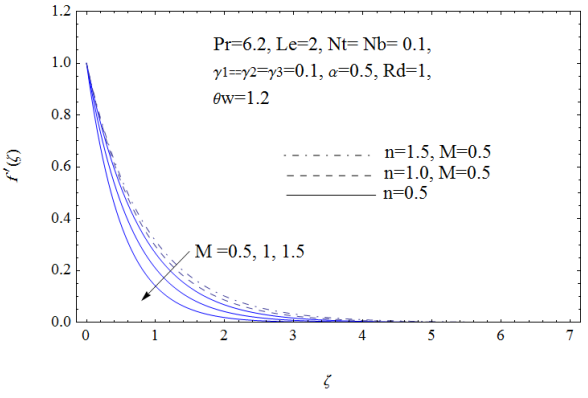

Fig. 5. *Influence of magnetic parameter on the velocity*

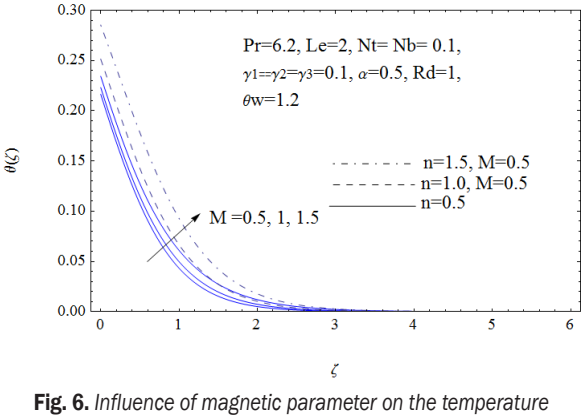

Fig. 6. *Influence of magnetic parameter on the temperature*

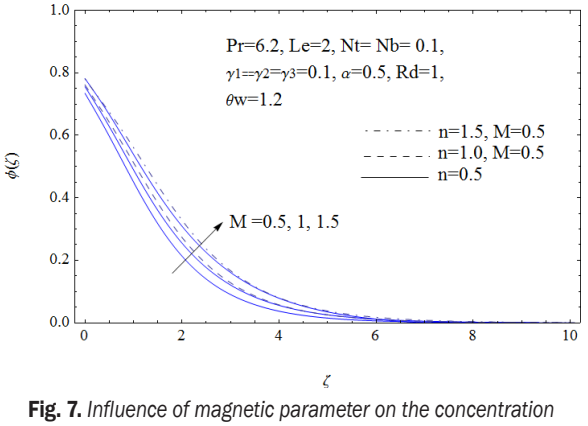

Fig. 7. *Influence of magnetic parameter on the concentration*

shown in Figs. 10 and 11. The figures show that the increase of the temperature ratio decreases both the temperature and the concentration of the nanoparticles near the surface.

The effects of Biot numbers on the temperature and nanoparticles concentration are shown in Figs. 12 to 14. It is clear that the temperature and nanoparticle concentration both increase by the increase in thermal Biot number and concentration Biot number.

The effect of random motion of the nanoparticles within the fluid appears in this study through the Brownian motion parameter Nb. Referring to Figs. 15 and 16, one can observe that increasing Nb leads to an increase in the temperature and a decrease of the nanoparticles concentration. Moreover, one can observe that the impact of the random moving of particles on the concentration decreases by increasing the value of Brownian motion parameter for all values of the shape parameter n.

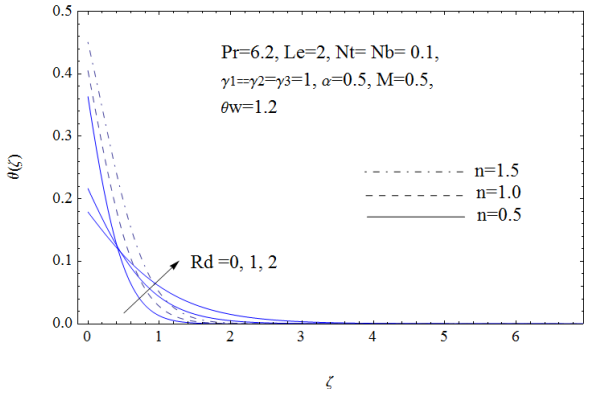

Fig. 8. *Influence of radiation parameter on the temperature*

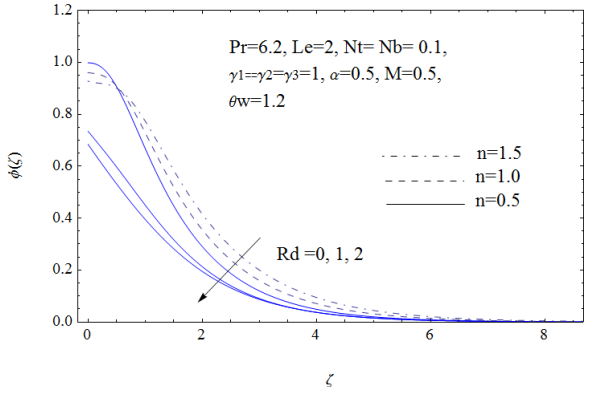

Fig. 9. *Influence of radiation parameter on the concentration*

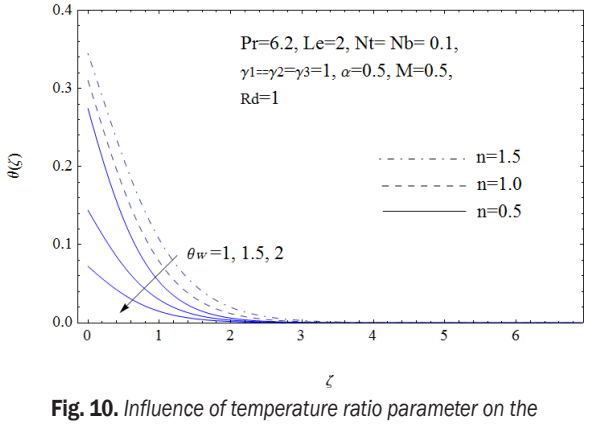

Fig. 10. *Influence of temperature ratio parameter on the temperature*

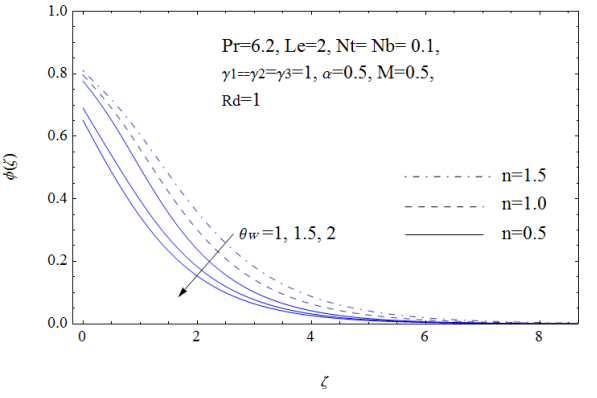

Fig. 11. *Influence of temperature ratio parameter on the concentration*

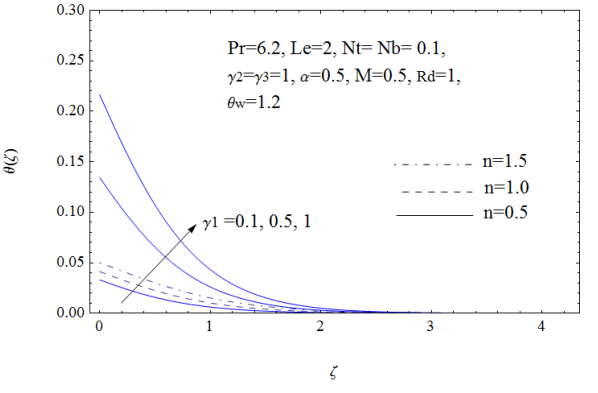

Fig. 12. *Influence of thermal ratio parameter on the temperature*

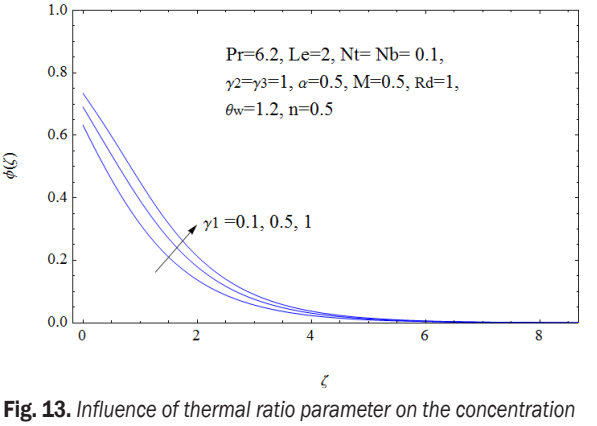

Fig. 13. *Influence of thermal ratio parameter on the concentration*

The Thermophoresis parameter Nt is a dimensionless parameter that describes the response of the suspended particles to the force of the temperature gradient. Figs. 17 amd 18 show that the increase of this parameter leads to increasing the boundary layer temperature and nanoparticles concentration. Moreover, Fig. 18 shows that the effect of this phenomenon on the concentration is very clear in the case of $n>1$. In addition, one can observe that increasing the thermophoresis parameter leads to forming a concentrated zone of the nanoparticles near the surface.

The main objective of this work is to study the effects of convective condition with the thickness variation and the nonlinear thermal radiation on the boundary layer behaviour.

Table 2 presents the values of the skin friction, Nusselt number and the Sherwood number for linear

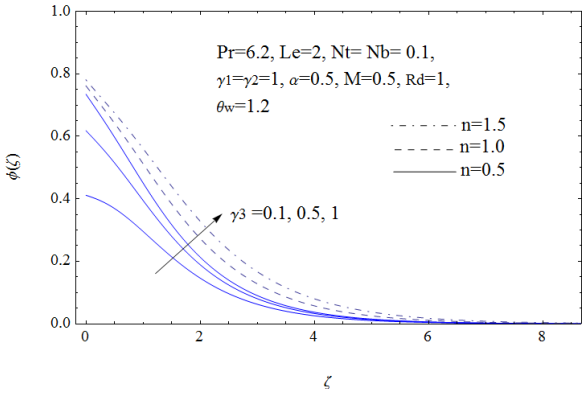

Fig. 14. *Influence of concentration Biot number on the concentration*

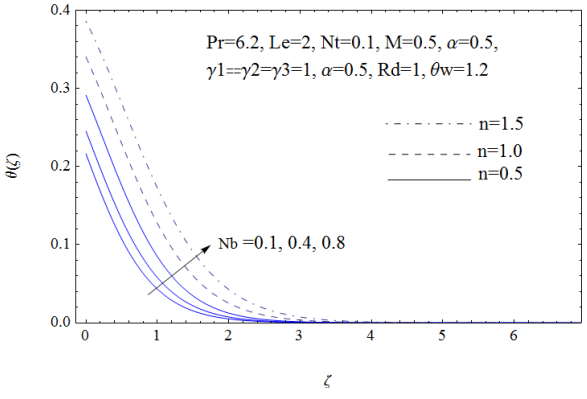

Fig. 15. *Influence of Brownian motion parameter on the temperature*

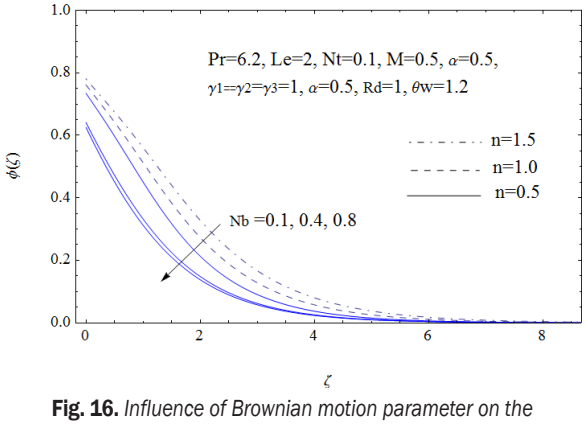

Fig. 16. *Influence of Brownian motion parameter on the concentration*

and non-linear thermal radiation at three cases of shape parameter *n*. from the first look, one can observe that the skin friction and Sherwood number values increase with the increase of the shape parameter *n*. Such increasing of *n* decreases the values of the Nusselt number. Moreover, one can observe that the presence of thermal radiation increases the Nusselt

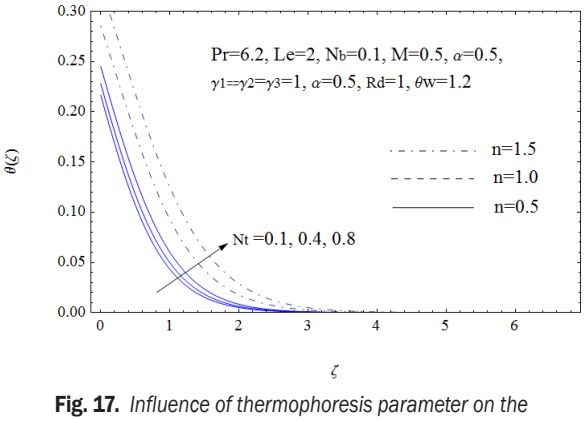

Fig. 17. *Influence of thermophoresis parameter on the concentration*

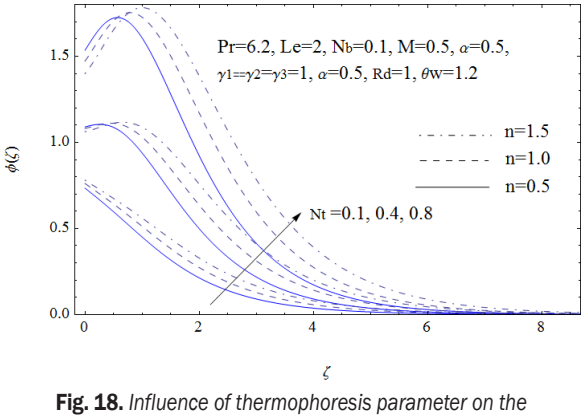

Fig. 18. *Influence of thermophoresis parameter on the concentration*

and Sherwood numbers. Finally, the values obtained in Table 2 indicate that the nonlinear modelling of the thermal radiation gives high values for Nusselt and Sherwood numbers. It is worth mentioning that the increasing of the skin friction and Nusselt number values to the increase of surface shear stress and the rate of heat transfer from the surface.

The effects of hydromagnetic flow on the skin friction, Nusselt number and Sherwood number are shown in Table 3. The observed results show that using hydromagnetic flow as a cooling medium increases skin friction, and decrease Nusselt number and Sherwood number. Consequently, the surface shear stress is increased, and the rate of heat transfer and rate of mass transfer is decreased by increasing the magnetic parameter *M*.

Table 4 shows the influence of thermal Biot number on the Nusselt and Sherwood Numbers. It is clear that the increase of the heat convective coefficient increases the heat flux and decreases the mass flux relative to the increasing and decreasing of the Nusselt and Sherwood Numbers, respectively. In contrast, the effect of concentration Biot number on

Table 2. *Values of skin friction, Nusselt number and Sherwood number for linear and non-linear thermal radiation at Le=2, Pr=6.2, Nt=Nb=0.1, M=0.5, α=0.5, and $\gamma_1=\gamma_2=\gamma_3=0.1$*

θ_w	Rd	n	$-f''(0)$	$-\theta'(0)$	$-\phi'(0)$	Cfx	Nu	Sh
1	1	0.5	1.2807	0.0439	0.0814	2.2183	0.0966	0.0705
		1.0	1.2247	0.0411	0.0793	2.4495	0.0960	0.0793
		1.5	1.1827	0.0383	0.0774	2.6446	0.0953	0.0866
1.2	0	0.5	1.2807	0.1099	0.0733	2.2183	0.0951	0.0635
		1.0	1.2247	0.0943	0.0722	2.4495	0.0943	0.0722
		1.5	1.1827	0.0834	0.0713	2.6446	0.0933	0.0797
	1	0.5	1.2807	0.0308	0.0829	2.2183	0.0976	0.0718
		1.0	1.2247	0.0294	0.0807	2.4495	0.0971	0.0807
		1.5	1.1827	0.0282	0.0788	2.6446	0.0966	0.0881

Table 3. *Values of skin friction, Nusselt number and Sherwood number for MHD flow at α=0.5, Le=2, Pr=6.2, Nt=Nb=0.1, θ_w=1.2, Rd=1 and $\gamma_1=\gamma_2=\gamma_3=1$*

M	n	$-f''(0)$	$-\theta'(0)$	$-\phi'(0)$	Cfx	Nu	Sh
0.5	0.5	-1.2807	-0.2472	-0.2653	-0.0031	151.93	162.45
	1.00	-1.2247	-0.2266	-0.2384	-0.0035	160.73	168.56
	1.50	-1.1827	-0.2089	-0.2192	-0.0037	165.60	173.26
1	0.5	-1.5297	-0.2450	-0.2443	-0.0037	150.45	149.61
	1.00	-1.4142	-0.2241	-0.2177	-0.0040	158.95	153.96
	1.50	-1.3351	-0.2060	-0.1991	-0.0042	163.32	157.43
2	0.5	-1.9310	-0.2415	-0.2181	-0.0047	148.45	133.57
	1.00	-1.7321	-0.2196	-0.1854	-0.0049	155.77	131.10
	1.50	-1.5981	-0.2006	-0.1675	-0.0051	159.02	132.41

Table 4. *Values of Nusselt number and Sherwood number for different values of thermal Biot number α=0.5, Le=2, Pr=6.2, Rd=1, θ_w=1.2, M=0.5, Nt=Nb=0.1 and $\gamma_1=\gamma_3=1$*

γ_2	n	$-\theta'(0)$	$-\phi'(0)$	Nu	Sh
0.1	0.50	0.08478	0.34525	0.26876	0.29900
	1.00	0.07490	0.31222	0.24747	0.31222
	1.50	0.06771	0.28563	0.23170	0.31935
0.5	0.50	0.20411	0.28636	0.64704	0.24799
	1.00	0.18533	0.25829	0.61235	0.25829
	1.50	0.17000	0.23725	0.58175	0.26525
1	0.50	0.24716	0.26528	0.78351	0.22974
	1.00	0.22657	0.23839	0.74859	0.23839
	1.50	0.20886	0.21915	0.71473	0.24502

Table 5. *Values of Nusselt number and Sherwood number for different values of concentration Biot number Le=2, Pr=6.2, Rd=1, θ_w=1.2, M=0.5, α=0.5, Nt=Nb=0.1 and $\gamma_1=\gamma_2=1$*

γ_3	n	$-\theta'(0)$	$-\phi'(0)$	Nu	Sh
0.1	0.50	0.24863	0.05885	0.78818	0.05096
	1.00	0.22822	0.05719	0.75403	0.05719
	1.50	0.21066	0.05630	0.72087	0.06295
0.5	0.50	0.24770	0.19088	0.78521	0.16530
	1.00	0.22714	0.17631	0.75047	0.17631
	1.50	0.20945	0.16585	0.71676	0.18543
1	0.50	0.24716	0.26528	0.78351	0.22974
	1.00	0.22657	0.23839	0.74859	0.23839
	1.50	0.20886	0.21915	0.71473	0.24502

the rate of heat and mass transfer is shown in Table 5. The effect of this number on the Nusselt number is low and limited, but it has a direct effect on the Sherwood number and the mass flux such that increasing the concentration Biot number increases the mass flux.

5 CONCLUSIONS

This study presents a mathematical model of a continuous moving non-flat surface over a hot convective fluid subjected to nonlinear thermal radiation and magnetic field. Above the surface, there is a Nanofluid boundary layer with Brownian motion and thermophoresis effects. The heat and mass transfer characteristics of the boundary layer are the main concern of this study, and the following results are obtained:

- The values of the Nusselt and Sherwood numbers for non-linear thermal radiation model are high comparing with a linear model.

- Surface shear stress for the convex outer shape surface ($n<1$) is higher than that in the case of concave outer shape surface ($n>1$).
- The presence of convective conditions decreases surface heat flux and mass flux.
- The random motions of the nanoparticles and the thermophoresis force have direct and high influences on the concentration boundary layer, especially for the non-flat surface.

6 NOMENCLATURES

u velocity in the x direction [m/s],
v velocity in the y direction [m/s],
υ kinematic viscosity [m²/s],
a, b, δ constants [-],
T temperature [ºC],
C concentration [mol/m³],
C_p specific heat capacity [J/(kg·K)],
k thermal conductivity [W/(m·K)],
h convective heat transfer coefficient [-],
k_m surface mass transfer coefficient [-],
D_B Brownian diffusion [m²/s],
D_T thermophoresis diffusion [m²/s],
q_r heat flux [W/m²],
ρ density of the base fluid [kg/m³],
σ electrical conductivity [s/m],
$B(x)$ strength of the magnetic field [kg/(s²·m)],
$\alpha^{\times}$ thermal diffusion [m²/s],
α^* Rosseland mean absorption coefficient [-],
η, ζ similarity variables [-],
$\theta(\eta)$ dimensionless temperature [-],
$\phi(\eta)$ dimensionless concentration [-],
σ^* Boltzmann constant, [m²·kg/(s²·K)]
α thickness parameter, $\alpha = \delta\sqrt{\frac{1+n}{2}\frac{a}{\upsilon}}$ [-],
θ_w temperature ratio, $\theta_w = T_w / T_\infty$ [-],
Pr Prandtl number, $\mathrm{Pr} = \upsilon/\alpha$ [-]
Le Lewis number, $\mathrm{Le} = \upsilon/D_B$ [-],
M magnetic field parameter, $\mathrm{M} = \frac{\beta_0^2\sigma}{a\rho}$ [-],
Rd radiation parameter, $\mathrm{Rd} = \frac{4\,\sigma^* T_\infty^3}{k\,\alpha^*}$ [-],
Nb Brownian parameter, $Nb = \frac{\tau D_B}{\upsilon}(C_w - C_\infty)$ [-],
Nt thermophoresis parameter, $Nt = \frac{\tau D_t}{\upsilon T_\infty}(T_w - T_\infty)$ [-],
γ_1 thermal ratio, $\gamma_1 = h/k$,[-]
γ_2 thermal Biot number, $\gamma_2 = \frac{h}{k}\sqrt{\frac{\upsilon}{a(x+b)^{n-1}}}$ [-],
γ_3 concentration Biot number, $\gamma_3 = \frac{k_m}{D_m}\sqrt{\frac{\upsilon}{a(x+b)^{n-1}}}$ [-],
τ specific heat capacity ratio, $\tau = \frac{(\rho Cp)_p}{(\rho Cp)_f}$ [-]

7 REFERENCES

[1] Choi, S.U.S., J.A. Estman (1995). Enhancing thermal conductivity of fluids with nanoparticles. *Proceedings of the ASME International Mechanical Engineering Congress & Exposition*, vol. 231, p. 99-105.

[2] Hamad, M.A.A. (2011). Analytical solution of natural convection flow of a Nanofluid over a linearly stretching sheet in the presence of magnetic field. *International Communications in Heat and Mass Transfer*, vol. 38, no. 4, p. 487-492, **DOI:10.1016/j.icheatmasstransfer.2010.12.042**.

[3] Yacob, N.A., Ishak, A., Pop, I., Vajravelu, K. (2011). Boundary layer flow past a stretching/ shrinking surface beneath an external uniform shear flow with a convective surface boundary condition in a Nanofluid. *Nanoscale Research Letters*, vol. 6, 1-7, **DOI:10.1186/1556-276X-6-314**.

[4] Alsaedi, A., Awai, s M., Hayat, T. (2012). Effects of heat generation/absorption on stagnation point flow of Nanofluid over a surface with convective boundary conditions. *Communications in Nonlinear Science and Numerical Simulation*, vol. 17, no. 11, p. 4210-4223, **DOI:10.1016/j.cnsns.2012.03.008**.

[5] Elbashbeshy E.M.A., Emam T.G., and Abdel-wahed M.S. (2014). An exact solution of boundary layer flow over a moving surface embedded into a nanofluid in the presence of magnetic field and suction/injection. *Heat and Mass Transfer*, vol. 50, no. 1, p. 57-64, **DOI:10.1007/s00231-013-1224-x**.

[6] Abu Bakar N.A., Zaimi W.M.K.A.W., Abdul Hamid R., Bidin, B., Ishak, A. (2012). Boundary layer flow over a stretching sheet with a convective boundary condition and slip effect. *World Applied Sciences Journal*, vol. 17, p. 49-53.

[7] Öztürk, A., Kahveci, K. (2016). Slip flow of nanofluids between parallel plates heated with a constant heat flux. *Strojniški vestnik – Journal of Mechanical Engineering*, vol. 62, no. 9, p. 511-520, **DOI:10.5545/sv-jme.2016.3188**.

[8] Noghrehabadi A., Pourrajab R., Ghalambaz M. (2013).Flow and heat transfer of nanofluids over stretching sheet taking into account partial slip and thermal convective boundary conditions. *Heat and Mass Transfer*, vol. 49, no. 9, p. 1357-1366, **DOI:10.1007/s00231-013-1179-y**.

[9] Rahman, M.M., Eltayeb, I.A. (2013). Radiative heat transfer in a hydromagnetic nanofluid past a non-linear stretching surface with convective boundary condition. *Meccanica*, vol. 48, no. 3, p. 601-615, **DOI:10.1007/s11012-012-9618-2**.

[10] Ramesh, G.K., Gireesha B.J. (2014). Influence of heat source/sink on a Maxwell fluid over a stretching surface with convective boundary condition in the presence of nanoparticles. *Ain Shams Engineering Journal*, vol. 5, no. 3, p. 991-998, **DOI:10.1016/j.asej.2014.04.003**.

[11] Nadeem, S., Haq, R.U. (2014). Effect of thermal radiation for megnetohydrodynamic boundary layer flow of a nanofluid past a stretching sheet with convective boundary conditions. *Journal of Computational and Theoretical Nanoscience*, vol. 11, n. 1-9, p. 32-40, **DOI:10.1166/jctn.2014.3313**.

[12] Chamkha, A.J., Rashad, A.M., RamReddy, C., Murthy, P.V.S.N. (2014). Viscous dissipation and magnetic field effects in a non-Darcy porous medium saturated with a nanofluid under convective boundary condition. *Special Topics & Reviews*

in Porous Media, vol. 5, no. 1, p. 27-39, **DOI:10.1615/SpecialTopicsRevPorousMedia.v5.i1.30**.

[13] RamReddy Ch., Murthy P.V.S.N., Chamkha, A.J., Rashad, A.M. (2013). Soret effect on mixed convection flow in a Nanofluid under convective boundary condition. *International Journal of Heat and Mass Transfer*, vol. 64, p. 384-392, **DOI:10.1016/j.ijheatmasstransfer.2013.04.032**.

[14] Ibrahim, W., Shankar, B. (2013). MHD boundary layer flow and heat transfer of a nanofluid past a permeable stretching sheet with velocity, thermal and solutal slip boundary conditions. *Computers & Fluids*, vol. 75, p. 1–10, **DOI:10.1016/j.compfluid.2013.01.014**.

[15] Hayat, T., Imtiaz, M, Alsaedi, A. (2014). MHD flow of nanofluid over permeable stretching sheet with convective boundary conditions, *Thermal Science* (On-line first), **DOI:10.2298/TSCI140819139H**.

[16] Fang, T., Zhang, J., Zhong ,Y. (2012). Boundary layer flow over a stretching sheet with variable thickness. *Applied Mathematics and Computation*, vol. 218, no. 13, p. 7241-7252, **DOI:10.1016/j.amc.2011.12.094**.

[17] Elbashbeshy, E.M.A, Emam, T.G., Abdel-wahed, M.S. (2013). Flow and heat transfer over a moving surface with non-linear velocity and variable thickness in a nanofluid in the presence of thermal radiation. *Canadian Journal of Physics*, vol. 91, no. 2, p. 124-130, **DOI:10.1139/cjp-2013-0168**.

[18] Abdel-wahed, M.S., Elbashbeshy, E.M.A., Emam, T.G. (2015). Flow and heat transfer over a moving surface with non-linear velocity and variable thickness in a Nanofluid in the presence of Brownian motion. *Applied Mathematics and Computation*, vol. 254, p. 49-62, **DOI:10.1016/j.amc.2014.12.087**.

[19] Pantokratoras, A., Fang, T. (2013). Sakiadis flow with nonlinear Rosseland thermal radiation. *Physica Scripta*, vol. 87, no. 1, **DOI:10.1088/0031-8949/87/01/015703**.

[20] Abdel-wahed, M.S., Akl, M. (2016). Effect of hall current on MHD flow of a nanofluid with variable properties due to a rotating disk with viscous dissipation and nonlinear thermal radiation. *AIP Advances*, vol. 6, no. 9, **DOI:10.1063/1.4962961**.

Strojniški vestnik - Journal of Mechanical Engineering 63(2017)2, 129-137
DOI:10.5545/sv-jme.2016.3719
Original Scientific Paper
Received for review: 2016-05-08
Received revised form: 2016-07-29
Accepted for publication: 2016-12-05

Comfort Improvement of a Novel Nonlinear Suspension for a Seat System Based on Field Measurements

Leilei Zhao – Changcheng Zhou* – Yuewei Yu
Shandong University of Technology, School of Transportation and Vehicle Engineering, China

This paper describes improved ride comfort of a novel nonlinear suspension for seat system based on field measurements. For the novel nonlinear suspension proposed, a rubber spring is used as its elastic element which has highly nonlinear characteristics to adapt various working conditions, and an asymmetrical damper is designed to yield asymmetric damping characteristics. Previous seat models were not very suitable for the system; thus, a nonlinear mathematical model was built to describe it better. Then, based on field measurements, the model parameters were identified, and the suspension damping coefficients were tuned under the practical constraints, to achieve satisfactory ride comfort to the greatest extent possible. Finally, the bench test was carried out, and the results show that, after the coefficients tuning, the seat vertical frequency-weighted root mean square (RMS) acceleration values are decreased by about 10 % and 8 % under the driving conditions on the highway and the gravel road, respectively, which proves the damping coefficients tuned are workable. The novel nonlinear suspension and the method of the damping coefficients tuning provide a valuable reference for further improving ride comfort to better protect the driver's health.

Keywords: ride quality; road conditions; nonlinear suspension; coefficients tuning

Highlights

- *A rubber spring is used as an elastic element of seat suspension.*
- *A nonlinear mathematical model of seat suspension system.*
- *Integrated optimization of damping coefficients.*
- *Field measurements.*

0 INTRODUCTION

Seat suspension is an essential component of trucks. The design of seat suspension has significance for comfort improvement [1] to [3]. Prolonged exposure to occupational vibrations leads to some diseases for drivers [4] and [5]. Reducing the vibration transmitted from vehicle to the driver has become a key issue [6] and [7]. To reduce the vibration, various seat suspension systems use a wide variety of springs as the elastic component, including the coil spring, the air spring, and the rubber spring, etc.

Due to the good nonlinear characteristics of the rubber spring, it is widely used as the elastic element of vehicle suspension systems, especially in rail vehicle suspensions and in chassis suspensions of commercial vehicles. For example, to improve the service life of the rubber spring for rail vehicle suspensions, Luo et al. researched the fatigue design method of rubber springs [8]. Luo presented an evaluation method of the creep behaviours of the rubber suspension for railway vehicles [9]. Sebesan et al. analysed the broad application prospects of the rubber suspension on the railway vehicles [10]. Pang et al. analysed the mechanical properties of the rubber suspension for heavy vehicles using the finite element method [11]. Many research efforts on the modelling and designs of the vibration isolation system using rubber springs have been made. Thaijaroen and Harrison studied the dynamic behaviours of rubber isolators using a simulation model with six parameters [12]. Sun et al. investigated the modelling method and the parameter acquisition method of a rubber isolator [13]. In their paper [14], they presented a model to describe the hysteretic characteristics of a rubber isolator. Ren et al. studied the effects of the temperature and the pressure on the shear stiffness of the rubber spring [15].

In recent years, the rubber spring has been applied to the seat suspension. For example, Zhou et al. investigated a seat suspension system with a type of rubber spring embedded with metal splints [16]. The dynamic characteristics of the seat suspension should be matched according to the road conditions of vehicles [17] to [19]. The common methodology is to use a passive seat suspension system model to optimize the results, which could be approached by the single degree-of-freedom (DOF) vibration isolation system [20] and [21]. To facilitate the dynamic analysis of vehicles equipped with the rubber spring, Berg presented a rubber spring model with five parameters [22]. Shi and Wu presented a nonlinear model with fractional derivatives for rubber springs of railway vehicle suspensions [23].

*Corr. Author's Address: Shandong University of Technology, School of Transportation and Vehicle Engineering, China, greatwall@sdut.edu.cn

These above studies about the designs of the vibration isolation system using rubber springs have significant relevance to the seat suspension. However, these previous models were not very suitable for the seat suspension system with a nonlinear hollow rubber spring and an asymmetrical damper with bushings, which will be optimized in this paper.

The objective of this work is to present a nonlinear mathematical model for a novel seat suspension system which employs a hollow rubber spring as the elastic element and improves its ride comfort by optimal design based on field measurements. According to the field measurements, the damping coefficients were tuned. In the end, by bench test, the optimal matching results were validated.

1 SEAT SYSTEM MODEL

The driver's seat analysed in this study is a new seat, which was tested for use in a heavy truck. The suspension seat was configured as a typical scissor system. It employs a hollow rubber spring and a hydraulic damper. They were mounted between the scissor structure on the seat pan and the seat frame. The hollow rubber spring, as shown in Fig. 1, is used as the elastic element of the seat suspension system, which has highly nonlinear characteristics to adapt the various working conditions.

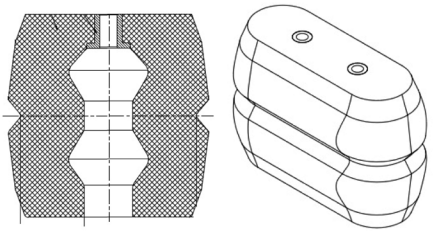

Fig. 1. *The hollow rubber spring*

A good and simple mathematical model would enable us to make reasonable indicative predictions of seat performance, and related models exist. The paper [25] provided a linear model of a seat suspension system with the damper mounting bushings. The paper [16] presented a nonlinear model of seat suspension system with the polynomial fitting the stiffness characteristics of the rubber spring, but the damper has linear damping. In this study, the seat dynamic properties are known to be non-linear, and the damper mounting bushings and friction in various seat components cannot be neglected, especially in response to low magnitude vibration. Thus, the previous models of seat suspension systems were not expected to be sufficient to simulate the driver's seat used in this study.

The assumptions made in formulating the model are as follows. *Assumption* 1: The elastic deformation of the seat frame could be ignored for this simplified model, and the driver is replaced by a matching block while removing the seat cushion. *Assumption* 2: The hollow rubber spring stiffness is considered to be nonlinear, while its damping is considered to be constant. *Assumption* 3: The asymmetric damping characteristics of the seat damper are simplified to be different constants in compression and rebound. *Assumption* 4: The Coulomb friction F_f within the linkage mechanism and the rubber spring is assumed to possess ideal properties. *Assumption* 5: The dynamic properties of the damper mounting bushings are characterized by equivalent linear stiffness while neglecting the damping coefficients.

A vertical dynamic model of the seat system was created on the basis of the assumptions, as shown in Fig. 2. C_s represents the rubber spring damping, m represents the effective mass; K_{b1} and z_{b1} represent the upper bushing stiffness and vertical displacement, respectively; K_{b2} and z_{b2} represent the lower bushing stiffness and vertical displacement, respectively; z_s represents the seat pan vertical displacement; q represents the vertical displacement input. Although the model is relatively simple, it can capture the major dynamic properties of seat suspension systems, including the seat vertical acceleration response, the seat suspension dynamic travel and so on. For academic purposes and the practical engineering problem, it may be useful to introduce the complex problem in a simplified form.

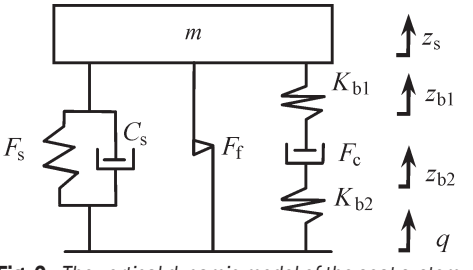

Fig. 2. *The vertical dynamic model of the seat system*

The motion equations of the model can be written as:

$$\begin{cases} m\ddot{z}_s = -F_s - C_s(\dot{z}_s - \dot{q}) - K_{b1}(z_s - z_{b1}) - F_f \\ F_c - K_{b1}(z_s - z_{b1}) = 0 \\ F_c - K_{b2}(z_{b2} - q) = 0 \end{cases}. \quad (1)$$

In Eq. (1), the force F_f can be written as:

$$F_f = F_0 \cdot \mathrm{sgn}(\dot{z}_s - \dot{q}), \quad (2)$$

where, F_0 is the magnitude of Coulomb friction force.

The damping force F_c can be written as:

$$F_c = \begin{cases} C_1(\dot{z}_{b1} - \dot{z}_{b2}) & \dot{z}_{b1} - \dot{z}_{b2} \geq 0 \\ C_2(\dot{z}_{b1} - \dot{z}_{b2}) & \dot{z}_{b1} - \dot{z}_{b2} \leq 0 \end{cases}, \quad (3)$$

where, C_1 is the rebound damping and C_2 is the compression damping.

The polynomial model was adopted to depict the dynamic properties of the rubber spring [25]; thus, the F_s can be simplified as:

$$F_s = K_{s1}(z_s - q) + K_{s3}(z_s - q)^3, \quad (4)$$

where, K_{s1} and K_{s3} are the stiffness coefficients.

2 PARAMETERS IDENTIFICATION

2.1 Field Measurements

To provide accurate input signals for parameters identification, the field measurements were carried out. The driver's weight is 65 kg. For a truck in this study, its drive type is 4×2, and its gross vehicle weight and load capacity are 5 and 10 tonnes, respectively. Taking the truck with this new-type seat as a test object, an accelerometer (sensor type, Lance LC0173) was installed on the driver's seat base. With the truck under fully laden conditions, on the highway at 65 km/h, 75 km/h, and 85 km/h, and on the gravel road at 40 km/h, 50 km/h, and 60 km/h, the acceleration signals were tested. Both the highway and the gravel road are relatively straight, and their surfaces are very dry. For each test condition, the sampling length was 40 s, and the sampling frequency was 200 Hz.

To avoid the dynamic characteristic influences of the seat cushion and the driver, further laboratory measurements were undertaken. The seat cushion was removed, and then the seat was secured to the test rig made by Moog Inc. with the driver replaced by a 65-kg matching block. Accelerometers (sensor type, Lance LC0173) were installed on the seat base and on the seat pan. The equipment exerted the previous acceleration excitations for 40 s from the field measurements, and the accelerations on the seat pan were measured under the driving conditions on the highway and the gravel road. For each laboratory measurement, the sampling length was 40 s, and the sampling frequency was 200 Hz.

2.2 Model Parameter Identification

Taking the minimum of quadratic error function J_I between the simulated seat vertical acceleration root-mean-square RMS_{sim} and the tested RMS_{test}, the objective function J_I of parameters identification can be expressed as:

$$\min\{J_I\} = \min\{\mathrm{RMS}_{sim} - \mathrm{RMS}_{test}\}^2, \quad (5)$$

where, K_{s1}, K_{s3}, K_{b1}, K_{b2}, C_s, C_1, C_2, and F_0 are the variables to be identified.

The vector of the variables to be identified:

$$\mathbf{x} = [K_{s1}, K_{s3}, K_{b1}, K_{b2}, C_s, C_1, C_2, F_0]. \quad (6)$$

In order to facilitate the parameters identification, Table 1 provides a list of the variables to be identified.

Table 1. *Estimated initial, upper and lower limits values for model parameters identification*

Variables		Initial values	Lower bound	Upper bound
K_{s1}	[kN/m]	12	8	30
K_{s3}	[kN/m³]	2120	1800	9950
K_{b1}	[kN/m]	100	80	150
K_{b2}	[kN/m]	100	80	150
C_s	[N·s/m]	80	100	500
C_1	[N·s/m]	600	300	1600
C_2	[N·s/m]	200	100	1000
F_0	[N]	10	2	30

Based on the target function J_I and the constraint conditions above, the identification problem is a minimal design problem with constraint conditions. This study adopts multi-island genetic algorithm to solve the problem, and the specific identification program was compiled using the software Matlab. This algorithm is a conventional global optimization method [26]. The essential parameters of the algorithm are considered, as listed in Table 2. Based on the built model of the seat system, a MATLAB/Simulink simulation model was created, and the flow chart of parameter identification is shown in Fig. 3.

Based on the signals measured under the driving condition on the highway at 65 km/h, 75 km/h, and 85 km/h, the model parameters were identified, respectively. The convergence values of the target function J_I are 0.000012, 0.000008, and 0.000004, respectively. The results are listed in Table 3. In order to reduce the error of the identified parameters, the average values at different speeds are regarded as the final results.

Table 2. *The essential parameters of the algorithm*

Parameters	value
Sub-population size	10
Number of islands	10
Number of generations	10
Rate of crossover	1.0
Rate of mutation	0.01
Rate of migration	0.01
Interval of migration	5
Elite size	1
Tournament size	0.5
Penalty base	0.0
Penalty multiplier	1000.0
Penalty exponent	2

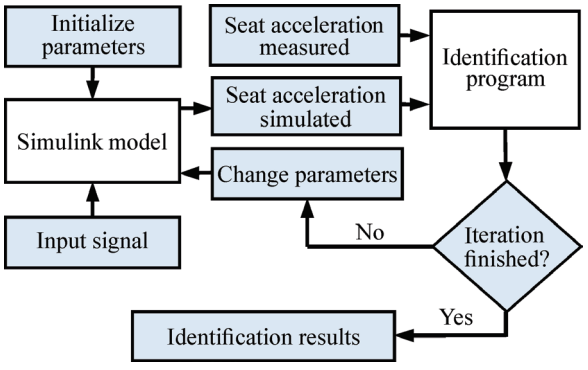

Fig. 3. *The flow chart of parameter identification*

Table 3. *The results of system parameter identification*

Mechanical parameter		Running Speed [km/h]			Average value
		65	75	85	
K_{s1}	[kN/m]	17.1	17.5	17.3	17.3
K_{s3}	[kN/m³]	9354.8	9359.2	9351.6	9355.2
K_{b1}	[kN/m]	119.3	120.4	118.6	119.4
K_{b2}	[kN/m]	116.8	119.5	119.3	118.5
C_s	[N·s/m]	104.2	101.1	102.7	102.7
C_1	[N·s/m]	651.7	656.3	652.8	653.6
C_2	[N·s/m]	431.5	427.8	429.3	429.5
F_0	[N]	13.9	11.2	13.2	12.8

2.3 Simulation Validation of the Identified Parameters

To verify the correctness of the parameters identified, a finite element method (FEM) analysis about the compression-spring force of the rubber has been made. This study adopts well known Moony-Rivlin model to simulate mechanical properties of rubber spring in ANSYS software [27]. A comparison between deformation curve of the rubber spring calculated by ANSYS software and that identified is shown in Fig. 4.

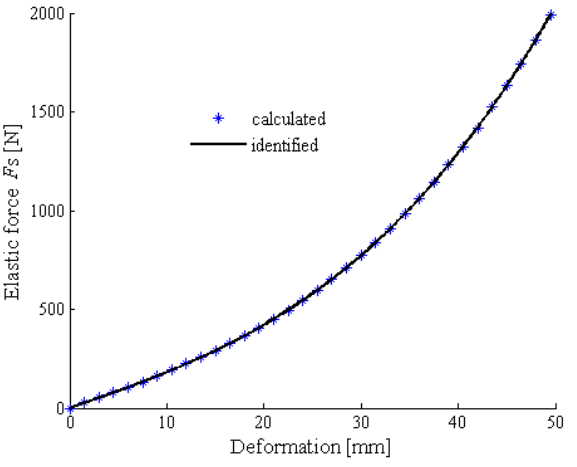

Fig. 4. *A comparison between the deformation curve calculated by ANSYS software and that identified*

From Fig. 4, it can be known that the deformation curve calculated by ANSYS software is extremely close to that identified. The results show that the deformation curve identified is acceptable. To further verify the effectiveness of the seat suspension system model with the parameters identified, using the signals measured under the driving condition on the gravel road at 40 km/h, 50 km/h, and 60 km/h, the simulations were conducted, respectively. The signal length for each simulation is 15 s. A comparison of the seat vertical acceleration RMS values between the simulated and those measured on the gravel road is shown in Table 4.

Table 4. *Comparison of the seat vertical acceleration RMS values between the simulated and the measured*

RMS		Running Speed [km/h]		
		40	50	60
Measured	[m/s²]	1.87	2.26	2.75
Simulated	[m/s²]	1.76	2.14	2.96
Absolute deviation	[m/s²]	–0.11	–0.12	0.21
Relative deviation	[%]	–5.88	–5.31	7.64

From Table 4, the relative deviations of the seat vertical acceleration RMS values between the simulated and the measured are –5.88 %, –5.31 %, and 7.64 %, respectively. The results show that the model with the identified parameters is workable. In order to further compare the discrepancies between the simulated and the measured, Fig. 5 presents a comparison of the seat vertical acceleration responses a_z between the simulated and measured at 60 km/h.

Fig. 6 presents a comparison of the seat vertical acceleration power spectral density (PSD) between the simulated and measured at 60 km/h. From Figs. 5 and 6, both the simulated a_z and PSD coincide well with the measured, respectively. The results show that the model with the parameters identified is workable.

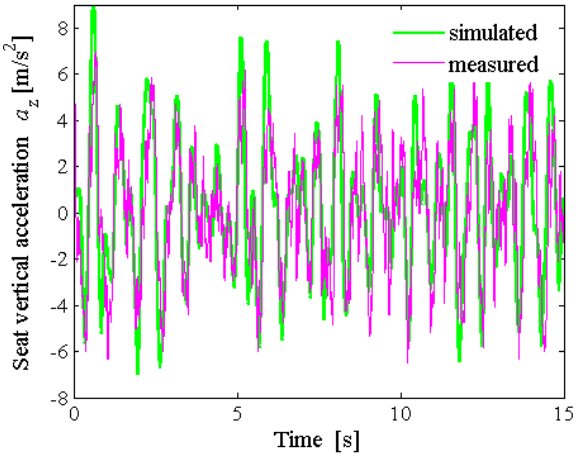

Fig. 5. *Comparison of the seat vertical acceleration response az between the simulated and the measured*

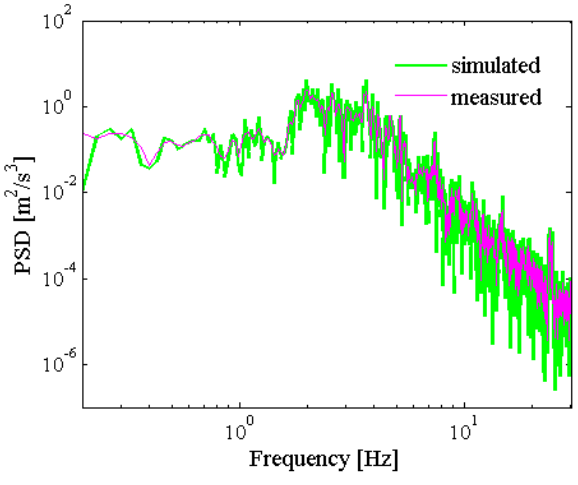

Fig. 6. *Comparison of the seat vertical acceleration PSD between the simulated and the measured*

3 SENSITIVITY ANALYSIS AND DAMPING MATCH

3.1 Sensitivity Analysis of the Model Parameters

At present, the commonly used index of ride comfort is weighted RMS acceleration recommended by ISO 2631-1:1997 [28]. According to this standard, the weighted RMS acceleration at seat pan and seat back in three directions should be calculated for evaluating ride comfort. The seat vertical frequency-weighted RMS acceleration was adopted to evaluate ride comfort in this study. The seat vertical frequency-weighted RMS acceleration $\sigma_{\ddot{z}_s}$ can be expressed as:

$$\sigma_{\ddot{z}_s} = [\int_{0.5}^{80} w^2(f) G_a(f) \mathrm{d}f]^{1/2}, \tag{7}$$

where, $G_a(f)$ is the power spectral density of the seat's vertical acceleration. The frequency weighted coefficient $w(f)$ in Eq. (7) is as follows:

$$w(f) = \begin{cases} 0.5 & (0.5 \le f < 2.0) \\ f/4.0 & (2.0 \le f < 4.0) \\ 1.0 & (4.0 \le f < 12.5) \\ 12.5/f & (12.5 \le f < 80.0) \end{cases}. \tag{8}$$

In this section, the sensitivity analysis was done to reveal the effects of the model parameters on the index of ride comfort. According to [29], in this paper, the sensitivity can be defined as:

$$S_{\pm 10\%} = \left[\frac{\sigma_{\ddot{z}_s}(B \pm 10\% \cdot B) - \sigma_{\ddot{z}_s}(B)}{\sigma_{\ddot{z}_s}(B)} \right] / [\pm 10\%]. \tag{9}$$

$$S = \sqrt{\frac{1}{2}(|S_{+10\%}| + |S_{-10\%}|)}, \tag{10}$$

where, B is the design variable, including K_{s1}, K_{s3}, K_{b1}, K_{b2}, C_s, C_1, C_2, and F_0; $S_{\pm 10\%}$ is the level of sensitivity in the given design range ±10 %; S is the sensitivity.

The calculated sensitivities of the model parameters under different conditions are shown in Table 5. The final sensitivity order of model parameters is shown in Fig. 7.

Table 5. *The calculated sensitivities of the model parameters under different conditions*

Mech. par.	On the gravel road [km/h]			On the highway [km/h]			Average value
	40	50	60	65	75	85	
K_{s1}	0.412	0.408	0.410	0.413	0.410	0.411	0.411
K_{s3}	0.232	0.231	0.234	0.230	0.233	0.231	0.232
K_{b1}	0.182	0.189	0.186	0.187	0.185	0.184	0.186
K_{b2}	0.187	0.185	0.181	0.182	0.189	0.186	0.185
C_s	0.112	0.111	0.110	0.112	0.113	0.112	0.112
C_1	0.321	0.322	0.329	0.324	0.322	0.326	0.324
C_2	0.281	0.280	0.281	0.279	0.283	0.282	0.281
F_0	0.090	0.091	0.089	0.093	0.091	0.092	0.091

Table 5 shows almost the same sensitivity distribution of the model parameters under different conditions. The average value of the sensitivities was taken as the real sensitivity. From Fig. 7, the

linear stiffness coefficient K_{s1} of the spring has the most substantial effect on the seat vertical frequency-weighted RMS acceleration, and followed by the equivalent damping coefficients C_1 and C_2 of rebound stroke compression and stroke. For the magnitude of Coulomb friction force F_0, its performance impact is minimal; however, it cannot be ignored for the dynamic model built. In addition, all the sensitivities are less than 0.45, which shows the identification values of model parameters are highly stable. That is to say, even though a deviation exists for each identified parameter of the model, the dynamic response does not change dramatically.

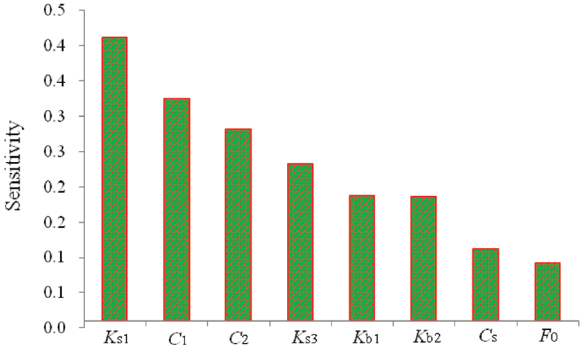

Fig. 7. The sensitivity order of model parameters

3.2 Damping Match

From the sensitivity analysis above, for the given rubber spring, the equivalent damping coefficients C_1 and C_2 have a critical influence on ride comfort. Thus, in this section, the damping match for the seat suspension system will be carried out.

To reduce the vibration from the seat base, the damping match objective function J_o can be expressed as:

$$\min\{J_o\} = \min\{\sigma_{\ddot{z}_s}\}, \tag{11}$$

where, C_1 and C_2 are the variables to be optimized.

In the optimization process, to ensure that the collision probability between the seat frame and the bump stop is within 0.135 %, the ratio of the standard deviation $\sigma(f_d)$ of the seat suspension dynamic travel f_d to the limited travel $[f_d]$ of the seat suspension system must satisfy:

$$\frac{\sigma(f_d)}{[f_d]} \le \frac{1}{3}, \tag{12}$$

where, the dynamic limited travel $[f_d]$ of the seat suspension for the original truck is 35 mm.

According to the study on the design of seat suspension [30], the optimization range of the damper damping coefficients for the seat suspension must satisfy:

$$\begin{cases} 500 \le C_1 \le 1100 \\ 100 \le C_2 \le 600 \end{cases}, \tag{13}$$

Based on the target function J_o and the constraint conditions above, the optimization problem is also a minimal design problem with constraint conditions. This study also adopts a multi-island genetic algorithm to solve the problem, and the damping optimization program was compiled. The essential parameters of the algorithm are the same as those of the identification program. The flow chart of damping optimization is shown in Fig. 8.

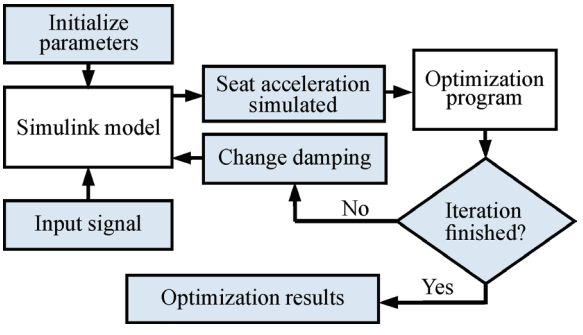

Fig. 8. *The flow chart of damping optimization*

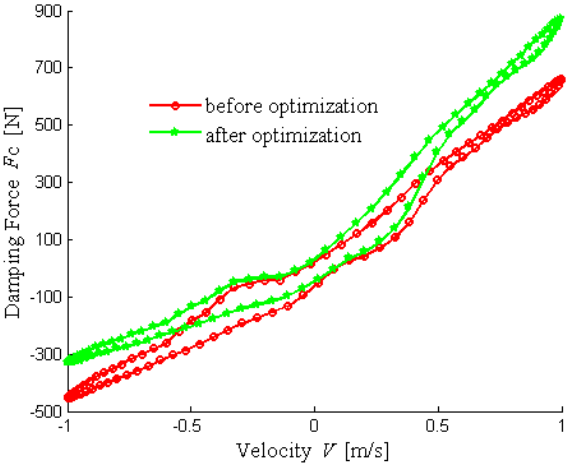

Fig. 9. *The curve of velocity vs. damping force*

Using the signals measured under the driving condition on the highway at 85 km/h that the truck travels most, the damping coefficients C_1 and C_2 of the damper were optimized, which are 891.8 and 329.5 N·s/m, respectively. The ratios of the rebound damping coefficient C_1 to the rebound damping coefficient C_2 for before and after optimization are

1.52 and 2.71, respectively. Base on the requirement of the damping coefficients optimized, the damper was redesigned by the damper manufacturer through trial and error. A comparison of the damper damping characteristics curve measured between before and after optimization is shown in Fig. 9.

From Fig. 9, after optimization, the rebound damping force becomes larger, while the compression damping force becomes smaller. Thus, both the damping coefficients and the ratio of the rebound damping coefficient C_1 to the rebound damping coefficient C_2 have significant influences on ride comfort.

4 TEST VERIFICATION

To verify the effectiveness of the damping coefficients optimized, a bench test was conducted.

The test was conducted on the test rig. The seat system with the damper damping coefficients optimized was attached to the test rig. The accelerometer was installed on the seat pan, and the driver was replaced with 65 kg sandbags. The sandbags were restrained with a belt. The equipment exerted the previous acceleration excitations mentioned above from the field measurements, and the accelerations on the seat pan were measured under the driving conditions on the highway at 65 km/h, 75 km/h, and 85 km/h, and on the gravel road at 40 km/h, 50 km/h, and 60 km/h. For each test condition, accelerations were collected for 40 s, filtered with minimum cut-off 0.5 Hz and maximum cut-off 80 Hz, and digitized at 1024 samples/s. According to Eq. (7), the seat vertical frequency-weighted RMS accelerations for different conditions were calculated. The results and comparisons between before and after optimization are shown in Table 6.

Table 6. *Comparison of the seat vertical frequency-weighed RMS acceleration before and after optimization*

Driving condition		RMS acceleration		
		Before optimization [m/s²]	After optimization [m/s²]	Relative deviation [%]
Gravel road	40 [km/h]	1.71	1.52	11.1
	50 [km/h]	1.97	1.80	8.6
	60 [km/h]	2.03	1.86	8.4
Highway	65 [km/h]	0.51	0.45	11.8
	75 [km/h]	0.56	0.50	12.0
	85 [km/h]	0.59	0.53	10.2

From Table 6, it can be seen that, under the driving condition on the highway at 65 km/h, 75 km/h, and 85 km/h, the seat vertical frequency-weighted RMS acceleration values are decreased by 11.8%, 12%, and 10.2%, respectively. Under the driving condition on the gravel road at 40 km/h, 50 km/h, and 60 km/h, the seat vertical frequency-weighted RMS acceleration values are decreased by 11.1%, 8.6%, and 8.4%, respectively. On the whole, the index of ride comfort has an improvement of about 10%.

In addition, the test for each running condition above was also conducted with the driver sitting on the seat. During testing, the driver sat upright with his back in contact with the seat back, placed his hands in his laps, and was restrained by a seat belt. In comparison, the driver would consider the ride comfort better than before optimization.

The results show that the seat system model and the damping match method proposed are reliable, and the damping coefficients matched are workable and effective.

5 CONCLUSIONS

A new mathematical model was built to better describe the novel nonlinear suspension for seat system, which can capture the main dynamic properties of seat suspension system. Using the signals measured under the driving condition on the highway at different running speeds, the model parameters were identified. Using the signals measured under the driving condition on the gravel road at different running speeds, the model was verified, and the results show that the parameters identified are workable. From the sensitivity analysis, the linear stiffness coefficient K_{s1} of the spring has the most substantial effect on the seat vertical frequency-weighted RMS acceleration, followed by the equivalent damping coefficients C_1 and C_2 of rebound stroke compression and stroke. For the magnitude of Coulomb friction force F_0, its performance impact is minimal.

Using the signals measured under the driving condition on the highway that the truck travels on most, the damper damping coefficients C_1 and C_2 were optimized. The results optimized show that both the damping coefficients and the ratio of the rebound damping coefficient C_1 to the rebound damping coefficient C_2 have significant influences on ride comfort. The bench test results further show that the seat system model and the damping match method proposed are reliable, and the damping coefficients matched are workable and effective. The novel nonlinear suspension and the method of the damping coefficients tuning provide a valuable reference for

further improving ride comfort to protect the driver's health better.

In the following study, the more complex model for the new type of suspension system will be researched, and the simulations with a complete vehicle including an appropriate model of the seat and the human body will be conducted. The random input running test and pulse input running test for ride comfort with the vehicle will be carried out according to the standard ISO2631-1:1997.

6 ACKNOWLEDGEMENTS

This work is supported by the National Natural Science Foundation of China (51575325), the Nature Science Foundation of Shandong (ZR2013EEM007), and Key R & D projects in Shandong Province (2015GGX105006).

7 REFERENCES

[1] Park, S.J., Lee, Y.S., Nahm, Y.E., Lee, J.W., Kim, J.S. (1998). Seating physical characteristics and subjective comfort: design considerations. *SAE Technical Paper*, no. 980653, **DOI:10.4271/980653**.

[2] Demontis, S., Giacoletto, M. (2002). Prediction of car seat comfort from human-seat interface pressure distribution. *SAE Technical Paper*, no. 2002-01-0781, **DOI:10.4271/2002-01-0781**.

[3] Blood, R.P., Ploger, J.D., Yost, M.G., Ching, R.P., Johnson, P.W. (2010) Whole body vibration exposures in metropolitan bus drivers: A comparison of three seats. *Journal of Sound and Vibration*, vol. 329, no. 1, p. 109-120, **DOI:10.1016/j.jsv.2009.08.030**.

[4] Kim, H.J., Martin, B.J. (2013). Biodynamic characteristics of upper limb reaching movements of the seated human under whole-body vibration. *Journal of Biomechanical Engineering*, vol. 29, no. 1, p. 12-22, **DOI:10.1123/jab.29.1.12**.

[5] Baig, H.A., Dorman, D.B., Bulka, B.A., Shivers, B.L., Chancey, V.C., Winkelstein, B.A. (2014). Characterization of the frequency and muscle responses of the lumbar and thoracic spines of seated volunteers during sinusoidal whole driver vibration. *Journal of Biomechanical Engineering*, vol. 136, no. 10, p. 1-7, **DOI:10.1115/1.4027998**.

[6] Griffin, M.J. (2012). Frequency-dependence of psychophysical and physiological responses to hand-transmitted vibration. Industrial Health, vol. 50, no. 5, p. 354-369, **DOI:10.2486/indhealth.MS1379**.

[7] Eger, T.R., Contratto, M.S., Dickey, J.P. (2013). Influence of driving speed, terrain, seat performance and ride control on predicted health risk based on ISO 2631-1 and EU Directive 2002/44/EC. *Journal of Low Frequency Noise, Vibration and Active Control*, vol. 30, no. 4, p. 291-312, **DOI:10.1260/0263-0923.30.4.291**.

[8] Luo, R.K., Cook, P.W., Wu, W.X., Mortel, W.J. (2003). Fatigue design of rubber springs used in rail vehicle suspensions. *Proceedings of the Institution of Mechanical Engineers Part F Journal of Rail and Rapid Transit*, vol. 217, no. 3, p. 237-240, **DOI:10.1243/095440903769012920**.

[9] Luo, R.K. (2015). Creep modelling and unloading evaluation of the rubber suspensions of rail vehicles. *Proceedings of the Institution of Mechanical Engineers Part F Journal of Rail and Rapid Transit*, vol. 230, no. 4, p. 1077-1087, **DOI:10.1177/0954409715576260**.

[10] Sebesan, I., Zaharia, N.L., Spiroiu, M.A., Fainus, L. (2015). Rubber suspension, a solution of the future for railway vehicles. *Materiale Plastice*, vol. 52, no. 1, p. 93-96.

[11] Pang, H., Li, H.Y., Fang, Z.D., Zhu, X.Y. (2012). Finite element analysis of mechanical characteristics on the composite rubber suspension of heavy vehicle. *Applied Mechanics and Materials*, vol. 121-126, p. 1702-1706, **DOI:10.4028/www.scientific.net/AMM.121-126.1702**.

[12] Thaijaroen, W., Harrison, A.J.L. (2010). Nonlinear dynamic modelling of rubber isolators using six parameters based on parabolic spring, springpot, and smooth-slip friction element. Polymer Testing, vol. 29, no. 7, p. 857-865, **DOI:10.1016/j.polymertesting.2010.07.007**.

[13] Sun, D.W., Chen, Z.G., Zhang, G.Y., Eberhard, P. (2011). Modeling and parameter identification of amplitude- and frequency-dependent rubber isolator. *Journal of Central South University of Technology*, vol. 18, p. 672-678, **DOI:10.1016/j.polymertesting.2010.07.007**.

[14] Sun, D.W., Eberhard, P., Zhang, G.Y., (2011). Parameter identification of rubber isolators using frequency-dependent spring and damper coefficients. *Journal of Donghua University*, vol. 28, no. 2 p. 134-138.

[15] Ren, L.Z., Liu, L., Ren, Z.C. (2012). Centrifuge rubber suspension spring characteristics of the experimental research, Applied Mechanics & Materials, vol. 157-158, p. 563-566, **DOI:10.4028/www.scientific.net/AMM.157-158.563**.

[16] Zhou, C.F., Sun, B.B., Chen, N., Zhang, X.Y., Sun, Q.H. (2007). Parameters identification and optimal design of vehicle seat suspension system. *Transactions of the Chinese Society for Agricultural Machinery*, vol. 38, p. 24-27. (in Chinese)

[17] Donati, P. (2002). Survey of technical preventative measures to reduce whole-driver vibration effects when designing mobile machinery. *Journal of Sound and Vibration*, vol. 253, no. 1, p. 169-183, **DOI:10.1006/jsvi.2001.4254**.

[18] Gohari, M., Tahmasebi, M. (2014). Off-road vehicle seat suspension optimisation, Part II: Comparative study between meta-heuristic optimisation algorithms. *Journal of Low Frequency Noise, Vibration and Active Control*, vol. 33, no. 4, p. 443-454, **DOI:10.1260/0263-0923.33.4.443**.

[19] Krishnasamy, D.P., Jayaraj, J,. John, D. (2013). Experimental investigation on road vehicle active suspension. *Strojniški vestnik - Journal of Mechanical Engineering*, vol. 59, no. 10, p. 620-625, **DOI:10.5545/sv-jme.2012.925**.

[20] Griffin, M. (1990). *Handbook of Human Vibrations*. Academic Press, London.

[21] Rakheja, S., Afework, Y., Sankar, S. (1994). An analytical and experimental investigation of the driver-seat-suspension system. *Vehicle System Dynamic,* vol. 23, no. 1, p. 501-524, **DOI:10.1080/00423119408969072**.

[22] Berg, M. (1998). A nonlinear rubber spring model for vehicle dynamics analysis. *Vehicle System Dynamics*, vol. 29, no. supl.1, p. 723-728, **DOI:10.1080/00423119808969599**.

[23] Shi, H.L., Wu, P.B. (2015). A nonlinear rubber spring model containing fractional derivatives for use in railroad vehicle dynamic analysis. *Proceedings of the Institution of Mechanical Engineers, Part F: Journal of Rail and Rapid Transit*, vol. 230, no. 7, p. 1745-1759, **DOI:10.1177/0954409715614871**.

[24] Silveira, M-, Pontes, J.B.R., Balthazar, J.M. (2014). Use of nonlinear asymmetrical shock absorber to improve comfort on passenger vehicles. *Journal of Sound and Vibration*, vol. 333, no. 7, p. 2114-2129, **DOI:10.1016/j.jsv.2013.12.001**.

[25] Stein, G.J., Múčka, P., Gunston, T.P. (2009). A study of locomotive driver's seat vertical suspension system with adjustable damper. *Vehicle System Dynamics*, vol. 47, no. 3, p. 363-386, **DOI:10.1080/00423110802148920**.

[26] Hu, X.Z., Chen, X.Q., Zhao, Y., Yao, W. (2014). Optimization design of satellite separation systems based on multi-island genetic algorithm. *Advances in Space Research*, vol. 53, no. 5, p. 870-876, **DOI:10.1016/j.asr.2013.12.021**.

[27] Arruda, E.M., Boyce, M.C. (1993). A three-dimensional constitutive model for the large stretch behavior of rubber elastic material. *Journal of the Mechanics & Physics of Solids*, vol. 41, no. 2, p. 389-412, **DOI:10.1016/0022-5096(93)90013-6**.

[28] ISO 2631-1 (1997). *Mechanical Vibration and Shock-Evaluation of Human Exposure to Whole-Driver Vibration-Part 1: General Requirements*. International Organization for Standardization, Geneva.

[29] Park, C., Kim, Y., Bae, D. (2009). Sensitivity analysis of suspension characteristics for Korean high speed train. *Journal of Mechanical Science and Technology*, vol. 23, no. 4, p. 938-941, **DOI:10.1007/s12206-009-0316-5**.

[30] Zhou, C.C. (2011), *Vehicle Suspension Design and Theory*. Peking University Press, Beijing, p. 40-42. (in Chinese)

Strojniški vestnik - Journal of Mechanical Engineering 63(2017)2, 138-147

DOI:10.5545/sv-jme.2016.3764 Original Scientific Paper
Received for review: 2016-05-30
Received revised form: 2016-08-02
Accepted for publication: 2016-11-18

Investigation of Mechanical Properties of Horn Powder-Filled Epoxy Composites

Duraisamy Kumar [1,*] – Sadayan Rajendra Boopathy[2] – Dharmalingam Sangeetha[2] – Govindarajan Bharathiraja[1]

[1]C. Abdul Hakeem College of Engineering and Technology, Department of Mechanical Engineering, India
[2]College of Engineering Guindy, Anna University, Department of Mechanical Engineering, India

Recent environmental concerns focus on the development of bio-composites, due to their low cost, and eco-friendly and bio-degradability characteristics. The aim of this work is to investigate the properties of particle-filled composites fabricated using bio-waste horn powder (HP) and epoxy resin. Composites were fabricated according to a Taguchi L_9 (3×3) orthogonal array. The HP particles and matrix were mixed in an appropriate ratio, compression-moulded and cured at room temperature to produce the specimens. Properties, such as ultimate tensile strength, tensile modulus, elongation percentage at break, flexural strength, flexural modulus, impact strength and microstructure of the specimens, were investigated. Scanning electron microscopy (SEM) micrographs of tensile tested specimens show good compatibility between HP particles and resin, when the HP volume is at 10 % and increases in agglomeration with increase in the HP volume percentage. Optimization of factors was done using grey relational analysis (GRA) and analysis of variance (ANOVA). The optimum factor levels were found to be the highest NaOH concentration (con.), A_3 (i.e., 0.3 N), the smallest HP size, B_1 (i.e., 125 μm) and the lowest HP volume percentage, C_1 (i.e., 10 %). The contribution of influencing factors in decreasing order were found to be, HP volume percentage with 90.87 %, HP size with 6.43 % and NaOH concentration with 0.78 %. From the R squared and R squared adjusted values of the properties, it is determined that most of the values are above 95 %, confirming a 95 % confidence level. Comparison between the optimum specimen and untreated HP specimens reveals that the optimum specimen has better properties. Hence, HP/epoxy composites can find application in various sectors.

Keywords: horn powder, epoxy resin, particulate composites, mechanical properties, optimization.

Highlights

- *HP particles are treated with NaOH to improve the compatibility between HP particles and matrix.*
- *Composites are fabricated using bio-waste HP and epoxy following the Taguchi L_9 (3×3) orthogonal array.*
- *Properties of pure horn and particulate HP/epoxy composites have been characterized.*
- *Optimization of factor levels has been done using GRA and ANOVA.*
- *Optimum factor levels are 0.3 N NaOH concentration (A_3), 125 μm HP size (B_1) and 10 % HP volume (C_1).*
- *Properties of optimum specimen composite are found to be better than untreated HP specimens.*
- *Use of HP in composites reduces environmental pollution, replaces synthetic fibres, and is cheap.*

0 INTRODUCTION

Polymeric composite materials are used in the automotive, marine, electrical, industrial, construction, house-hold appliances and sports goods fields due to their light weight, high strength, stiffness and corrosion resistance. Recently, extensive research work has been carried out on the natural fibre reinforced composite materials due to their abundant availability and low cost. Natural fibres such as kenaf, hemp, flax, jute, banana, sisal, bamboo, etc., are obtained from plants. Fibres, such as silk, feather, wool, etc., are obtained from animals. Horns are found in the heads of ox, buffalo, sheep, goat, etc. and are never branched. Horns are found in various shapes, length and curvature. These are made of a structural protein called keratin that is strong and rigid. Hard keratins have high sulphur content and are classified into two groups, α-keratin found in mammals, such as hair, horns, nails, etc. and β-keratin found in avian and reptilian tissues. Oxen horn is one of the by-products of slaughter houses. The central core of the horn turned into cylindrical form is used for manufacturing useful items. Horn chips of this process become landfill and cause environmental pollution. These chips can be used as filler for manufacturing composite materials. Epoxies are cross linked thermosetting materials, which cannot be recycled. Araldite LY 556 is medium viscosity, unmodified liquid epoxy resin based on Bisphenol-A. They are stable to chemical attacks and are excellent adherents, having slow shrinkage during curing and no emissions of volatile gases. High bonding strength and room temperature curing makes it commonly selected as a matrix material. Aradur, the hardener used with Araldite has the designation HY 951. The mixing ratio between resin and hardener is 100:10 parts by weight.

Sisson has briefly summarized the structure of horn [1]. Meyers et al. have discussed the structure and mechanical properties of biological materials [2].

*Corr. Author's Address: C. Abdul Hakeem College of Engineering and Technology, Melvisharam, Vellore, India, ilayakumard@gmail.com

Rizvi and Khan have investigated the frequency and temperature dependence of dielectric constant and loss factor in cow horn keratin [3]. Kumar and Boopathy have studied mechanical and thermal properties of defatted oxen horn fibre reinforced PP composites and observed that 15 % of horn fibre particles gave optimum results [4]. Venkateshwaran et al. have modified the fibre surface and found that 1 % NaOH-treated fibre-reinforced composites behave superior than other treated and untreated fibre composites, and high concentrations of alkali damages the fibre and decreases mechanical properties [5]. Fu et al. have reviewed the effects of particle size, particle/matrix interface adhesion and particle loading on the stiffness, strength and toughness of particulate-polymer composites [6]. Ku et al. have reviewed the tensile properties of various plant-based natural fibre reinforced polymer composites [7]. Mishra et al. have investigated the mechanical properties of alkali-treated chicken feather reinforced epoxy composites and found that the interface bonding between the matrix and the reinforcement is beneficial due to the formation of ester and amine groups [8]. Girisha et al. have investigated the effect of water absorption on the mechanical properties of sisal and coconut coir-reinforced epoxy composites and found that exposure to moisture caused a significant drop in the mechanical properties due to the degradation of the fibre-matrix interface [9]. Blau has presented a survey of compositions, functions and testing of commercial friction brake materials and their additives [10]. Deo and Acharya have studied abrasive wear behaviour of Lantana-Camara Fibre reinforced epoxy composites and observed that the optimum wear reduction was obtained when the fibre content is 40 weight % [11]. Olokode et al. have studied the synergistic effects of friction materials with cow hoof dust and bagasse and observed that friction material with 100 μm size gave better results than other sizes [12]. Antaryami has investigated the wear characteristics of teak wood dust-filled epoxy composites and found that the composite with 10 % wood dust may be more suitable for frictional applications [13]. Zhan et al. have investigated the properties of composites with epoxy, chicken feather fibre and E-glass fibres and found that the composites can be used as printed circuit boards [14]. Mishra and Nayak have investigated the dielectric properties of chicken feather-reinforced epoxy matrix composites and found that the dielectric properties are dependent on operating frequency and temperature conditions [15]. Krishnaiah and Shahabudeen have found that grey relational analysis is an accurate method for solving interrelationship among multiple responses in engineering problems. Analysis of variance is a method of dividing variation in an experiment into distinct components and the related degree of freedom. The frequency test (F-test) is employed to analyse and identify the significant effects of the parameters affecting the performance measures [16]. Fung has proposed grey relational analysis based on the Taguchi method's response table for the optimization of manufacturing processes for the wear property of fibre-reinforced polybutylene terephthalate composites [17]. Hasani et al. have used grey relational analysis to optimize the process parameters of open-end spinning system with multiple performance characteristics and found that the integration of grey relational analysis and the Taguchi method can be applicable for the optimization of process parameters and help to improve process efficiency [18]. Sui et al. have prepared cancun natural sand-filled epoxy composites and characterized thermal and mechanical properties of the composites containing up to 5 weight percentage of the sand particles and found that the highest flexural strength appears in the epoxy composite containing 1 weight percentage of sand particles [19]. Ozsoy et al. have studied the influence of micro-fillers Al_2O_3, TiO_2 and fly ash added in 10 weight percentage to 30 weight percentage; the nano-fillers Al_2O_3, TiO_2 and clay added in 2.5 weight percentage to 10 weight percentage on the mechanical properties of epoxy matrix composites. The results show that the tensile strength, flexural strength and elongation percentage at break values of composites decreased while the tensile modulus and flexural modulus increased with the increase in micro and nano-filler content [20]. Croccolo et al. have compared the mechanical properties of flax fibre/isophthalic resin composites and flax fibre/vinyl ester resin composites and found that isophthalic resin composites have better properties than vinyl ester resin composites do [21]. Valasek and Muller have described "two-body" abrasive wear on an abrasive cloth and a "three-body" abrasive wear on a machine with a rubber disc using sand abrasion and showed that there is no clear correlation between the two and three-body abrasions as far as the volume decrease is concerned [22]. Valasek and Muller have studied the abrasive wear resistance and hardness of waste corundum particle/epoxy composites with waste Al_2O_3 as filler and found that wear resistance and hardness have increased due to the inclusion of corundum [23].

The objective of this work is to develop a bio-waste HP-filled epoxy composite. Surface treatment of natural fibres using alkali (NaOH) solution overcomes

the difficulty of incompatibility between hydrophilic fibres and hydrophobic matrix. Optimization of factor levels for multiple quality responses like composite materials is very difficult. Optimum levels of parameters were obtained by fabricating the composites using Taguchi L_9 (3×3) orthogonal array and optimizing using GRA and ANOVA. GRA transforms multiple quality characteristics into grey relational grades. By comparing the grey relational grades, the arrays of respective quality characteristics are obtained in accordance with response grades to select an optimal set of process parameters. Apart from these nine compositions, specimens were also made with 20 % untreated HP and 80 % matrix and with neat epoxy. Mechanical and surface morphological properties of these composites were characterized and compared with the properties of specimens made of untreated HP and neat epoxy.

1 MATERIALS AND METHOD

1.1 Materials

HP chips used as fillers were obtained from a button-manufacturing factory near Ambur, Tamilnadu, India. Sodium Chloride Extrapure used to clean the HP particulates was obtained from S D Fine-Chem Limited, Mumbai, India. Diethyl Ether (Ether Solvent) used to de-fat the HP was obtained from Nice Chemicals (P) Ltd., Kochi, India. Sodium Hydroxide Flakes used to treat the HP surfaces was obtained from Qualikems Fine Chem Pvt. Ltd., Vadodara, India. Araldite LY 556 used as resin and Aradur HY 951 used as hardener were obtained from Huntsman Advanced Materials India Private Limited, Mumbai, India.

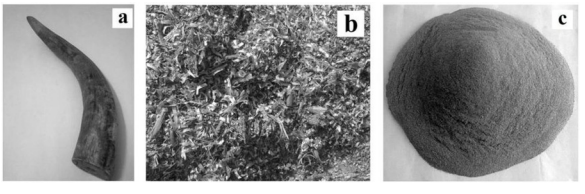

Fig. 1. *a) An ox horn, b) horn chips thrown as landfill and c) particles of HP sieved to a desired size*

1.2 HP Processing

Fig. 1a shows an ox horn. Fig. 1b shows horn chips as landfill. HP chips were washed in water thoroughly, dried, ground into particulates using double bladed electrical grinder and sieved to +125 μm, +250 μm and +425 μm sieve grades using a sieve shaker. Fig. 1c shows particles sieved to the desired size. The HP particles were washed in 0.1 Normality (N) NaCl solution for eight hours by changing the solution periodically after every two hours. They were washed in water, dried and immersed in diethyl ether for four hours to remove fat. Then they we rewashed in water thoroughly and dried. The defatted HP particles were treated with 0.1 N, 0.2 N and 0.3 N NaOH solutions for four hours, washed thoroughly in water and dried.

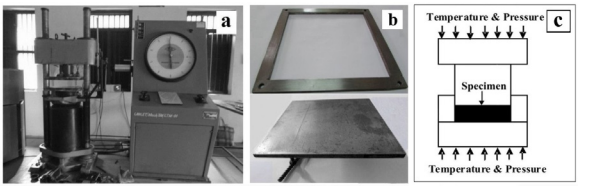

Fig. 2. *a) Hydraulic compression machine with dies fixed on table and crosshead, b) intermediate die with mould cavity and punch set, and c) manufacturing procedure of plate specimens*

1.3 Specimen Preparation

Fig. 2a shows the hydraulic compression machine with dies fixed on its table and crosshead. Fig. 2b shows the intermediate die with mould cavity and punch set. Fig. 2c shows the manufacturing procedure of plate specimens. Plates of size 290 mm × 290 mm × 4.5 mm were prepared following Taguchi L_9 orthogonal array with three factors and three levels as shown in Table 1 and with untreated HP and epoxy. The details of ingredients used are shown in Table 2. Required amount of resin and hardener were weighed using an electronic weighing balance of accuracy 0.001 g and mixed to get a homogeneous mixture of matrix. The surfaces and walls of a self-fabricated compression moulding dies were applied with release agent for easy removal of the moulded plate specimen. Required amount of HP was weighed and mixed with the matrix thoroughly. The mixture was transferred to the die and pressed at a pressure of 0.5 MPa for 30 minutes. The plates were post-cured at room temperature for 24 hours in clamped condition. The plates were allowed to rest in ambient conditions for one week. Test specimens were cut from the plate according to ASTM standards and the surfaces

Table 1. *Input factors for Taguchi L_9 orthogonal array*

Factors	Level 1	Level 2	Level3
NaOH con. (A) [N]	0.1	0.2	0.3
HP size (B) [μm]	125	250	425
HP vol. (C) [%]	10	20	30

were prepared with an emery sheet of 150 grit size. Fig. 3 shows the tensile test specimen, flexural test specimen, and impact test specimen.

Table 2. *Details of ingredients used*

Trial ID	HP			Matrix	Total Vol. [%]
	NaOH con. [N]	Particle size [μm]	Vol. [%]	Vol. [%]	
$A_1B_1C_1$	0.1	125	10	90	100
$A_1B_2C_2$	0.1	250	20	80	100
$A_1B_3C_3$	0.1	425	30	70	100
$A_2B_1C_2$	0.2	125	20	80	100
$A_2B_2C_3$	0.2	250	30	70	100
$A_2B_3C_1$	0.2	425	10	90	100
$A_3B_1C_3$	0.3	125	30	70	100
$A_3B_2C_1$	0.3	250	10	90	100
$A_3B_3C_2$	0.3	425	20	80	100
$A_0B_2C_2$	0	250	20	80	100
Epoxy	0	0	0	100	100

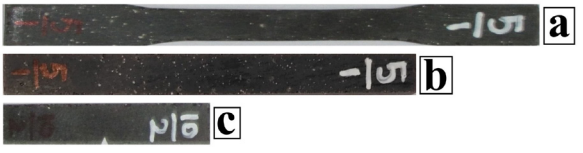

Fig. 3. *a) Tensile test specimen, b) flexural test specimen, and c) impact test specimen*

2 SPECIMEN TESTING

Specimens of dimensions 165 mm × 12.7 mm × 3 mm were subjected to tensile test as per ASTM D638 using a SHIMADZU universal testing machine. Dog-bone shaped specimens of 19 mm width at the widest section and 12.7 mm width at the narrow section, 115 mm gauge length and cross-head speed of 50 mm/min were used for this test. Specimens of dimensions 127 mm × 12.7 mm × 3 mm were subjected to three-point bend type flexural test as per ASTM D790 using an INSTRON universal testing machine. A cross-head speed of 2.6 mm/min and a span length of sixteen times the thickness of the specimen were used for this test. Specimens of dimensions 63.5 mm × 12.7 mm × 3 mm with a "V" notch depth of 2.54 mm and notch angle of 45° was used for conducting an Izod impact test as per ASTM D256 using a Tinius Olsen impact testing machine. Three replicate specimens were used for each test and the data reported are the average of these three tests. A JEOL scanning electron microscope was used for imaging the tensile tested specimens. All specimens were examined using an accelerating voltage of 3.0 kV power supply.

3 GREY RELATIONAL ANALYSIS

Grey relational analysis (GRA) was used for solving the interrelationship among the multiple responses. In this approach a grey relational grade was obtained for analysing the relational degree of the multiple responses. Original response data was obtained by conducting experiments at different levels of factors based on an orthogonal array. The responses were transformed into signal to noise (S/N) ratio. The term "signal" represents the desirable value and the term "noise" represents the undesirable value. The formulae for S/N ratio are designed such that larger factor level settings can be selected to optimize the quality characteristics of an experiment. The method of calculating the S/N ratio depends on whether the quality characteristic has smaller-the better, larger-the better and nominal-the best formulation. S/N ratios were transformed into normalized S/N ratios using appropriate formulae depending on the type of quality characteristics to avoid the effect of using different units and to reduce variability. Grey relational coefficients for the normalized S/N ratios were computed. Grey relational grades that represent the level of correlation between reference sequence and comparability sequence were determined. Using ANOVA, the contribution of influencing factors was obtained using grey relational grades.

4 RESULTS AND DISCUSSION

4.1 Properties of Pure Horn

Scanning electron microscopy (SEM) with an EDX test conducted on horn specimen reveals that the major elements present in horn are carbon, oxygen, nitrogen and molybdenum with a maximum carbon weight percentage of 59.03 [4]. Ultimate tensile strength, tensile modulus, elongation percentage at break, flexural strength, flexural modulus, impact strength, compression strength, hardness, density, extrapolated onset temperature (T_o) and first derivative peak temperature (T_p) of pure horn specimen are 41.86 MPa, 806.33 MPa, 5.04 %, 122.9 MPa, 4515.30 MPa, 136.70 J/m, 70.68 MPa, 86 HRL, 1304 kg/m^3, 225 °C and 507 °C, respectively [4]. The stress-strain diagram of pure horn specimen and the values of elongation percentage at break shows that the horn is brittle [4]. As the HP is of lower density and the mechanical and thermal properties of horn are better than polymers, use of HP particles as filler with polymers will enhance the properties.

4.2 Properties of HP/Epoxy Composites

Table 3 shows the mechanical properties of HP/epoxy composites and neat epoxy specimens. Table 4 shows the S/N ratios for mechanical properties of HP/epoxy composites. Larger-the better quality characteristics was used for ultimate tensile strength, tensile modulus, elongation percentage at break, flexural strength, flexural modulus and impact strength to withstand external forces. The formula to calculate larger-the better S/N ratio is: $S/N = -10\times\log(1/Y^2)$ where, Y is the output (response) of the experiment. Fig. 4 shows the main effects plots for S/N ratios of various properties obtained using MINITAB software. The main effects plot, graphs the S/N ratio for each factor level, connected by a line. When the line is horizontal, there is no main effect present. When the line is steeper, then different levels of the factor affect the response differently.

4.2.1 Ultimate Tensile Strength

The tensile strength of a particle-reinforced polymer matrix composite is based on effective load transfer between the matrix and the particles. Factors such as good bonding strength between fibre particles and resin, particle size and particle loading affect the strength [6]. The bonding can be enhanced by alkali treatment of fibre surfaces [5]. From Fig. 4a, it is observed that an increase in NaOH concentration (A_3) increases ultimate tensile strength because alkali treatment increases bonding strength. Smaller-sized particles have better dispersion, high surface area with the matrix, and the smallest HP size (B_1) thus gives increased strength. Powder loading decreases strength due to clustering of particles and thus the lowest HP volume percentage (C_1) gives high strength. From Fig. 4a, it is also observed that HP volume percentage influences better than HP size does, whereas NaOH concentration has no significant influence.

4.2.2 Tensile Modulus

Tensile modulus of a particle-reinforced polymer matrix composite is enhanced by adding high-stiffness particles to the polymer matrix. Tensile modulus is dependent on fibre loading but independent of particle size and interfacial adhesion [6]. Tensile modulus is

Table 3. *Mechanical properties of HP/epoxy composites and neat epoxy specimens*

Trial No.	Trial ID	Ultimate tensile strength [MPa]	Tensile modulus [MPa]	Elongation % at break [%]	Flexural strength [MPa]	Flexural modulus [MPa]	Impact strength [kJ/m²]
1	$A_1B_1C_1$	29.42	1069.83	3.41	49.39	3558.07	0.802
2	$A_1B_2C_2$	21.65	870.82	2.68	34.86	3020.28	0.771
3	$A_1B_3C_3$	16.75	605.08	1.86	23.29	2791.78	0.686
4	$A_2B_1C_2$	23.32	975.56	2.81	37.82	3258.04	0.745
5	$A_2B_2C_3$	19.56	658.5	2.18	28.93	2912.28	0.615
6	$A_2B_3C_1$	24.99	983.51	3.02	38.24	3206.05	1.168
7	$A_3B_1C_3$	20.55	778.31	2.39	32.85	2907.24	0.568
8	$A_3B_2C_1$	28.29	1052.68	3.17	44.66	3536.04	1.084
9	$A_3B_3C_2$	22.15	802.47	2.59	31.37	3108.8	0.958
10	$A_0B_2C_2$	15.51	585.38	2.65	51.25	6017.87	0.761
11	Epoxy	42.56	2076.52	3.54	56.82	3640.34	0.721

Table 4. *S/N ratios of mechanical properties of HP/epoxy composites*

Trial No.	Trial ID	Ultimate tensile strength	Tensile modulus	Elongation % at break	Flexural strength	Flexural modulus	Impact strength
1	$A_1B_1C_1$	29.37	60.59	10.66	33.87	71.02	-1.92
2	$A_1B_2C_2$	26.71	58.80	8.56	30.85	69.60	-2.26
3	$A_1B_3C_3$	24.48	55.64	5.39	27.34	68.92	-3.27
4	$A_2B_1C_2$	27.35	59.79	8.97	31.55	70.26	-2.56
5	$A_2B_2C_3$	25.83	56.37	6.77	29.23	69.28	-4.22
6	$A_2B_3C_1$	27.96	59.86	9.60	31.65	70.12	1.35
7	$A_3B_1C_3$	26.26	57.82	7.57	30.33	69.27	-4.91
8	$A_3B_2C_1$	29.03	60.45	10.02	33.00	70.97	0.70
9	$A_3B_3C_2$	26.91	58.09	8.27	29.93	69.85	-0.37

also affected by clustering of particles and de-bonding at high fibre loading. From Fig. 4b, it is observed that increase in NaOH concentration (A_3) increases tensile modulus because alkali treatment increases roughness and hardness of HP surfaces and thus offers resistance to movement of particles. Smaller particles have better dispersion, high surface area with the matrix and thus, the smallest HP size (B_1) gives increased tensile modulus. Powder loading increases clustering of particles and reduces tensile modulus. Thus, the lowest HP volume percentage (C_1) gives the highest tensile modulus. From Fig. 4b, it is also observed that NaOH concentration does not have significant influence, whereas HP volume percentage influences more than HP size does.

4.2.3 Elongation percentage at Break

From Fig. 4c, it is observed that increase in NaOH concentration (A_3) increases elongation percentage at the break because alkali treatment increases roughness and hardness of HP surfaces and thus increases bonding between the particles. Larger sized HP particles (B_3) offer more resistance to movement and thus decrease the elongation percentage at break. As HP particles are brittle, an increase in HP loading

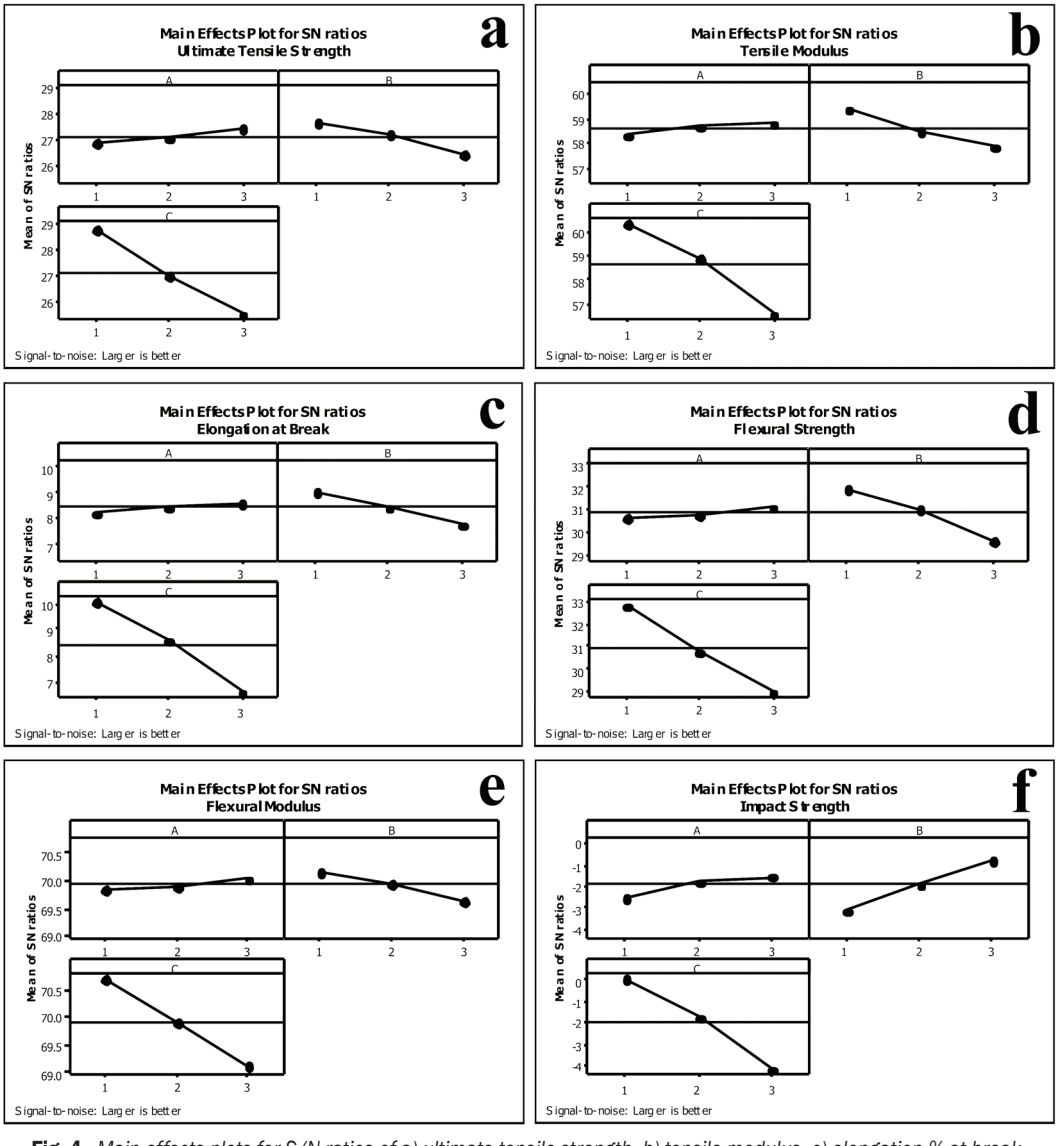

Fig. 4. *Main effects plots for S/N ratios of a) ultimate tensile strength, b) tensile modulus, c) elongation % at break, d) flexural strength, e) flexural modulus and f) impact strength*

increases the brittleness and clustering of particles and thus reduces the elongation percentage at break. Thus, the lowest HP volume percentage (C_1) gives the highest elongation percentage at break. From Fig. 4c, it is also observed that NaOH concentration and HP size do not influence greatly, whereas HP volume percentage has more influence.

4.2.4 Flexural Strength

Flexural strength of particle-reinforced polymer matrix composite is affected by factors such as the bonding strength between the particles and the matrix, size of the particles and particle loading [6]. From Fig. 4d, it is observed that increase in NaOH concentration (A_3) increases flexural strength because alkali treatment increases bonding strength. Smaller particles have better dispersion, high surface area with the matrix and thus the smallest HP size (B_1) gives better flexural strength. Powder loading increases clustering of particles and reduces flexural strength. Thus, the lowest HP volume percentage (C_1) gives the highest flexural strength. From Fig. 4d, it is also observed that NaOH concentration does not have significant influence, whereas HP volume percentage has more influence than HP size.

4.2.5 Flexural Modulus

Flexural modulus of a particle-reinforced polymer matrix composite depends on the fibre loading but is not affected by particle size and interfacial adhesion [6]. From Fig. 4e, it is observed that increase in NaOH concentration (A_3) increases flexural modulus because alkali treatment increases roughness and hardness of HP surfaces and thus offers resistance to movement of particles. Smaller particles have better dispersion, high surface area with the matrix and thus the smallest HP size (B_1) gives increased flexural modulus. Powder loading increases clustering of particles and reduces flexural modulus. Thus, the lowest HP volume percentage (C_1) gives the highest flexural modulus. From Fig. 4e, it is also observed that NaOH con. does not influence greatly, whereas HP volume percentage influences better than HP size.

4.2.6 Impact Strength

From Fig. 4f, it is observed that increase in NaOH concentration (A_3) increases impact strength because alkali treatment increases bonding strength. Larger sized particles (B_3) offer more resistance to movement and thus increase impact strength. As HP particles are brittle, any increase in HP loading increases brittleness and clustering of particles and thus reduces impact strength. Thus, the lowest HP volume percentage (C_1) gives the highest impact strength. From Fig. 4f, it is also observed that NaOH concentration does not have significant influence, whereas HP volume percentage influences better than HP size does.

From Table 3, it can be observed that the properties of HP/epoxy composites are less than the properties of virgin epoxy specimens. This is because HP particles in epoxy resin acts as stress concentration points and creates weakness in the adhesive force between HP particles and the resin. Clustering of HP problem and increase in brittleness with increase in powder loading are also the reasons for decreased mechanical properties of the composites. An agglomeration problem can also be observed from Fig. 6, the SEM images of tensile tested specimens.

Table 5. *Grey relational grades of trials*

Trials	$A_1B_1C_1$	$A_1B_2C_2$	$A_1B_3C_3$	$A_2B_1C_2$	$A_2B_2C_3$
GRG	0.915	0.504	0.345	0.587	0.389

Trials	$A_2B_3C_1$	$A_3B_1C_3$	$A_3B_2C_1$	$A_3B_3C_2$
GRG	0.709	0.427	0.866	0.515

Table 6. *Mean of grey relational grades*

Factors	Level1	Level2	Level3	Max-Min
NaOH con. (A)	0.588	0.562	0.603	0.041
HP size (B)	0.643	0.586	0.523	0.120
HP vol. % (C)	0.830	0.536	0.387	0.443

Table 5 shows the grey relational grades (GRG) of trials of L_9 orthogonal array. Table 6 shows the mean of grey relational grades. From Table 6, it can be observed that the mean of grades for the trial $A_3B_1C_1$ were found to be higher and is the optimum specimen. This is because alkali treatment makes the HP surfaces hard and rough and increases bonding strength. It is also observed that NaOH treated composites have improved properties than the untreated composites do. Therefore, NaOH concentration (A_3 i.e., 0.3 N) is found to be optimum. Smaller particles are desired for most of the mechanical properties, whereas bigger sized particles are desired for impact strength. Considering all the properties, smaller particles (B_1 i.e., 125 μm) are found to be optimal. Increase in powder loading increases clustering of the powder particles leading to surface cracks and incompatibility and thus affects the properties. This can be observed very well from SEM micrographs of tensile tested specimens. Thus, when the HP volume percentage

is the smallest (C1 i.e., 10 %) good compatibility between ingredients and epoxy resin is obtained leading to an optimal result. Fig. 5 shows the graphs of main effects plot for grey relational grades. From Fig. 5, it can also be observed that $A_3B_1C_1$ is an optimal specimen.

4.3 Scanning Electron Microscopy

Fig. 6 shows the SEM images of the tensile-tested specimens taken at a magnification of 250×, at a scale of 100 μm and at an accelerating voltage of 3.0 kV. Fig. 6a to i show the SEM images of the specimens of Taguchi L_9 orthogonal array. From Fig. 6a, d and g, which shows the SEM images of specimens with the smallest HP particle size (i.e., B_1 = 125 μm), it is found that good compatibility exists between the HP and the resin. This is because smaller particles have high surface area with the matrix and thus increases compatibility [6]. From Fig. 6c, f and i, which shows the SEM images of specimens with the highest HP volume percentage(i.e., C_3 = 30 %), it can also be observed that when the volume percentage of HP increases, clustering of particles takes place leading to incompatibility between the particles and the resin. From Fig. 6j, which shows the SEM image of the specimen $A_0B_2C_2$, the specimen with untreated HP, it can be observed that poor compatibility exists

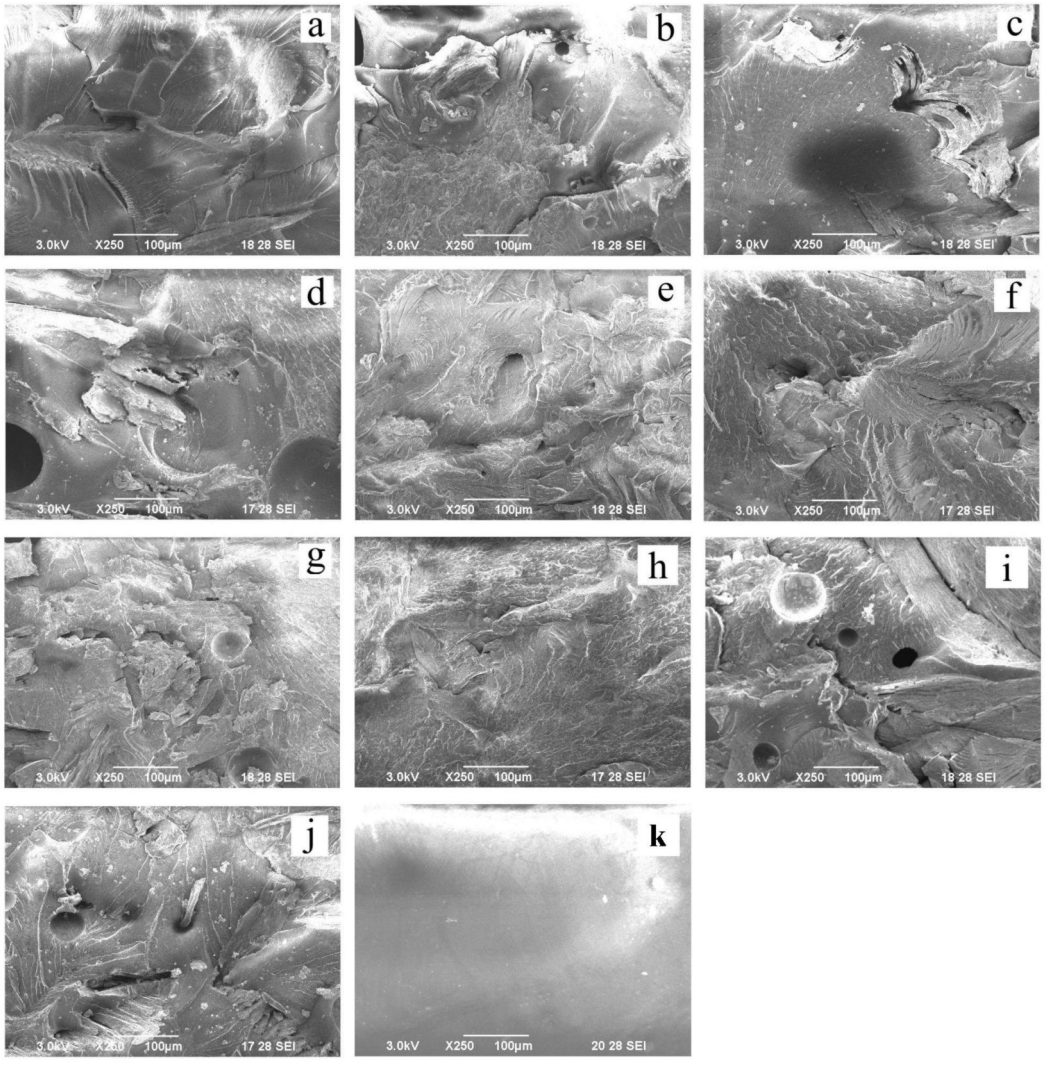

Fig. 6. *SEM micrographs of tensile tested surfaces of specimens taken at a magnification of 250×, at a scale of 100 μm and at an accelerating voltage of 3 kV; a) $A_1B_1C_1$, b) $A_1B_2C_2$, c) $A_1B_3C_3$, d) $A_2B_1C_2$, e) $A_2B_2C_3$, f) $A_2B_3C_1$, g) $A_3B_1C_3$, h) $A_3B_2C_1$, i) $A_3B_3C_2$, j) untreated HP specimen $A_0B_2C_2$ and k) neat epoxy specimen*

between the HP and the resin. From Fig. 6k, which shows the SEM image of the neat epoxy specimen, it can be observed that it is plain without any blow holes or surface cracks, due to the absence of HP particles.

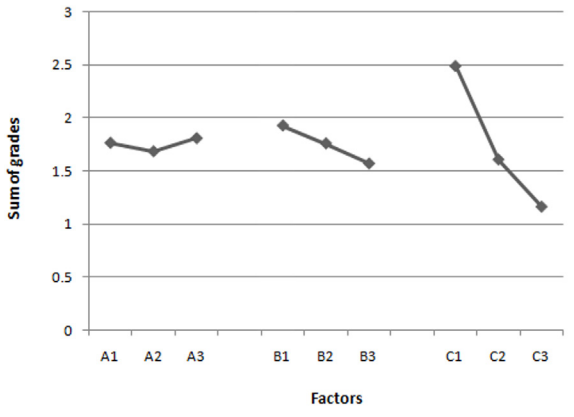

Fig. 5. *Graphs of main effects plot for grey relational grades*

Table 7. *ANOVA table for the grey relational grades of trials*

Factors	DOF	Sum of Squares	Mean Square	F Value	% Contribution
NaOH con.	2	0.003	0.001	0.41	0.78
HP size	2	0.022	0.011	3.37	6.43
HP vol. %	2	0.305	0.153	47.56	90.87
Error	2	0.006	0.003		1.91
Total	8	0.336			100.00

Table 7 shows the ANOVA table obtained for the grey relational grades of properties used to find the significant factor and percentage contribution of influencing factors. From the ANOVA table, it is observed that the major influencing factor is HP volume percentage with 90.87 %, the moderate influencing factor is HP size with 6.43 % and the least influencing factor is NaOH concentration with 0.78 %. This is due to the fact that when the HP volume percentage is increased, the compatibility between the HP particles and matrix interface is lost and this influences better than HP size and NaOH concentration. Table 8 shows the R squared and R squared adjusted values of mechanical properties of horn powder-filled epoxy composites. From Table 8, it can be observed that most of the values are above 95 %, confirming to 95 % confidence level.

5 CONCLUSION

Particle-filled composites are developed using bio-waste HP and epoxy resin. Mechanical and morphological properties, such as tensile strength, tensile modulus, elongation percentage at break, flexural strength, flexural modulus, impact strength and microstructure of the specimens were investigated.

Optimization of various factors was done using GRA and ANOVA, and the results were compared with the untreated HP specimens. From GRA, optimum factor levels were found to be 0.3 N NaOH concentration (A_3), 125 µm sized HP particles (B_1) and 10 % volume of HP particles (C_1). From ANOVA, it is observed that the major influencing factor is HP volume percentage with 90.87 %, the moderate influencing factor is HP size with 6.43 %, the least influencing factor is NaOH concentration with 0.78 % and the error percentage is found to be 1.91 %.

From SEM images of the tensile tested specimens, it can be observed that when the particle size increases, surface area with the matrix decreases and thus decrease the compatibility. Furthermore, when the HP volume percentage increases clustering of particles takes place leading to incompatibility between the particles and the resin.

From the R squared and R squared adjusted values of the properties, it can be observed that most of the values are above 95 %, confirming to 95 % confidence level. Comparing the optimum specimen $A_3B_1C_1$ with the untreated HP specimen $A_0B_2C_2$, optimum specimen has better properties and hence, HP/epoxy composites can find applications in various sectors.

As the filler is derived from bio-waste, this work is innovative. Use of bio-waste filler for composite manufacturing reduces environmental pollution and is also cost effective.

6 ACKNOWLEDGEMENTS

The authors would like to thank Anna University Chennai, Tamilnadu, India, Central Institute of Plastics Engineering and Technology, Chennai, Tamilnadu, India, Alagappa Chettiar College of Engineering and Technology, Karaikudi, Tamilnadu, India and Karunya

Table 8. *R squared and R squared adjusted values of mechanical properties*

Param.eters	Ultimate tensile strength	Tensile modulus	Elongation % at break	Flexural strength	Flexural modulus	Impact strength
R squared [%]	96.4	98.0	98.7	98.0	92.0	97.9
R squared adjusted [%]	94.2	96.8	98.0	96.7	87.2	96.7

University, Coimbatore, Tamilnadu, India for the manufacturing and testing of specimens. The authors also would like to thank the Management and the Department of Mechanical Engineering of C. Abdul Hakeem College of Engineering and Technology, Melvisharam-632509, Vellore District, Tamilnadu, India.

7 REFERENCES

[1] Sisson, S. (1930). *The Anatomy of the Domestic Animals*. W.B. Saunders Company, Philadelphia.

[2] Meyers, M.A., Chen, P.-Y., Lin, A.Y.-M., Seki, Y. (2008). Biological materials: Structure and mechanical properties. *Progress in Materials Science*, vol. 53, no. 1, p. 1-206, **DOI:10.1016/j.pmatsci.2007.05.002**.

[3] Rizvi, T.Z., Khan, M.A. (2008). Temperature-dependent dielectric properties of slightly hydrated horn keratin. *International Journal of Biological Macromolecules*, vol. 42, no. 1, p. 292-297, **DOI:10.1016/j.ijbiomac.2008.01.001**.

[4] Kumar, D., Rajendra Boopathy, S. (2014). Mechanical and thermal properties of horn fibre reinforced polypropylene composites. *Procedia Engineering*, vol. 97, p. 648-659, **DOI:10.1016/j.proeng.2014.12.294**.

[5] Venkateshwaran, N., Elaya Perumal, A., Arunsundaranayagam, D. (2013). Fibre surface treatment and its effect on mechanical and visco-elastic behaviour of banana/epoxy composite. *Materials and Design*, vol. 47, p. 151-159, **DOI:10.1016/j.matdes.2012.12.001**.

[6] Fu, S.-Y., Feng, X.-Q., Lauke, B., Mai, Y.-W. (2008). Effects of particle size, particle/matrix interface adhesion and particle loading on mechanical properties of particulate-polymer composites. *Composites: Part B: Engineering*, vol. 39, no. 6, p. 933-961, **DOI:10.1016/j.compositesb.2008.01.002**.

[7] Ku, H., Wang, H., Pattarachaiyakoop, N., Trada, M. (2011). A review on the tensile properties of natural fibre reinforced polymer composites. *Composites Part B: Engineering*, vol. 42, no. 4, p. 856-873, **DOI:10.1016/j.compositesb.2011.01.010**.

[8] Mishra, S.C., Nayak, N.B., Satapathy, A. (2010). Investigation on bio-waste reinforced epoxy composites. *Journal of Reinforced Plastics and Composites*, vol. 29, no. 19, p. 3016-3020, **DOI:10.1177/0731684408100740**.

[9] Girisha, C., Sanjeevamurthy, Srinivas, G.R. (2012). Sisal/coconut coir natural fibres-epoxy composites: Water absorption and mechanical properties. *International Journal of Engineering and Innovative Technology*, vol. 2, no. 3, p. 166-170.

[10] Blau, P.J. (2001). Compositions, functions, and testing of friction brake materials and their additives. *Oak Ridge National Laboratory Technical Report,* ORNL/TM-2001/64, Oak Ridge, **DOI:10.2172/788356**.

[11] Deo, C., Acharya, S.K. (2010). Effects of fibre content on abrasive wear of Lantana Camara fibre reinforced polymer matrix composite. *Indian Journal of Engineering and Materials Sciences*, vol. 17, p. 219-223.

[12] Olokode, O.S., Fakolujo, S.O., Aiyedun, P.O., Jaji, Z.O., Owoeye, F.T., Anyanwu, B.U. (2012). Experimental study on the morphology of keratin based material for asbestos free brake pad. *Journal of Basic & Applied Sciences*, vol. 8, no. 2, p. 302-308, **DOI:10.6000/1927-5129.2012.08.02.08**.

[13] Antaryami, M. (2014). Investigations on wear characteristics of teak wood dust filled epoxy composites. *Journal of Production Engineering*, vol. 17, no. 1, p. 75-78.

[14] Zhan, M., Wool, P.R., Xiao, J.Q. (2011). Electrical properties of chicken feather fibre reinforced epoxy composites. *Composites Part A: Applied Science and Manufacturing*, vol. 42, no. 3, p. 229-233, **DOI:10.1016/j.compositesa.2010.11.007**.

[15] Mishra, S.C., Nayak, N.B. (2010). An investigation of dielectric properties of chicken feather reinforced epoxy matrix composite. *Journal of Reinforced Plastics and Composites*, vol. 29, no. 17, p. 2691-2697, **DOI:10.1177/0731684409356610**.

[16] Krishnaiah, K., Shahabudeen, P. (2012). *Applied Design of Experiments and Taguchi Methods*, PHI Learning Private Limited, New Delhi.

[17] Fung, C.P. (2003). Manufacturing process optimization for wear property of fibre-reinforced polybutylene terephthalate composites with grey relational analysis. *Wear*, vol. 254, no. 3-4, p. 298-306, **DOI:10.1016/S0043-1648(03)00013-9**.

[18] Hasani, H., Tabatabaei, S.A., Amiri, G. (2012). Grey relational analysis to determine the optimum process parameters for open-end spinning yarns. *Journal of Engineered Fibres and Fabrics*, vol. 7, no. 2, p. 81-86.

[19] Sui, G., Jana, S., Salehi-khojin, A., Neema, S., Zhong, W.H., Chen, H.,Huo, Q. (2008). Thermal and mechanical properties of epoxy composites reinforced by natural hydrophobic sand. *Journal of Applied Polymer Science*, vol. 109, no. 1, p. 247-255, **DOI:10.1002/app.27321**.

[20] Ozsoy, I., Demirkol, A., Mimaroglu, A., Unal, H., Demir, Z. (2015).The influence of micro- and nano-filler content on the mechanical properties of epoxy composites. *Strojniški vestnik - Journal of Mechanical Engineering*, vol. 61, no. 10, p. 601-609, **DOI:10.5545/sv-jme.2015.2632**.

[21] Croccolo, D., De Agostinis, M., Fini, S., Liverani, A., Marinelli, N., Nisini, E., Olmi, G. (2015). Mechanical characteristics of two environmentally friendly resins reinforced with flax fibers. *Strojniški vestnik - Journal of Mechanical Engineering*, vol. 61, no. 4, p. 227-236, **DOI:10.5545/sv-jme.2014.2248**.

[22] Valasek, P., Muller, M. (2015). Abrasive wear in three-phase waste-based polymeric particle composites. *Tehnički vjesnik - Technical gazette*, vol. 22. 2, p. 257-262, **DOI:10.17559/TV-20130905190904**.

[23] Valasek, P., Muller, M., Hloch, S.(2015). Recycling of corundum particles-two-body abrasive wear of polymeric composites based on waste. *Tehnički vjesnik – Technical gazette*, vol. 22, no. 3, p. 567-572, **DOI:10.17559/TV-20131111140048**.

Vsebina

Strojniški vestnik - Journal of Mechanical Engineering
letnik 63, (2017), številka 2
Ljubljana, februar 2017
ISSN 0039-2480

Izhaja mesečno

Razširjeni povzetki (extended abstracts)

Strojniški vestnik - Journal of Mechanical Engineering 63(2017)2, SI 13

Prejeto v recenzijo: 2016-08-19
Prejeto popravljeno: 2016-11-28
Odobreno za objavo: 2016-12-07

Vpliv hidrodinamske kavitacije na pripravo vodne raztopine detergent za pranje tekstila

Tadej Stepišnik Perdih* – Brane Širok – Matevž Dular
Univerza v Ljubljani, Fakulteta za strojništvo, Slovenija

Pralni stroji so eni izmed največjih porabnikov energije in vode v gospodinjstvih. V zadnjih letih je znanstvena skupnost vložila veliko truda v trajnostni razvoj, tudi na področju pranja tekstila. Kljub temu pa je priprava raztopine vode in detergenta popolnoma prezrt proces s strani raziskovalcev. Priprava pralne raztopine v pralnih strojih, ki so trenutno na voljo na trgu, lahko traja do 10 minut. Avtorji raziskave menimo, da bi z izkoriščanjem hidrodinamske kavitacije lahko ta proces močno izboljšali.

Pojem kavitacija označuje nastanek parnih mehurčkov v kapljevini, njihovo aktivnost in prehod nazaj v kapljevito stanje. Pojavi se zaradi lokalnega zmanjšanja tlaka, pri čemer ostane temperatura medija približno nespremenjena. Kavitacija je vedno bolj uveljavljena metoda v procesni in kemijski industriji, saj se ob kolapsih kavitacijskih mehurčkov vzpostavijo ekstremne razmere. Te razmere omogočajo izvedbo procesov, za katere so sicer potrebne enormne količine energije

V naši raziskavi prikazujemo posebej zasnovan rotacijski generator hidrodinamske kavitacije, s katerim želimo izboljšati pripravo vodne raztopine detergenta. Delovanje generatorja kavitacije smo eksperimentalno testirali na laboratorijski postaji pralnega stroja. Kakovost priprave pralne kopeli smo ocenili glede na količine neraztopljenega pralnega praška po določenem času. Da bi lahko ustrezno določili, kakšen vpliv na izboljšanje priprave pralne kopeli ima sama kavitacija, smo v napravi vzpostavili dva obratovalna režima. V prvem režimu smo tlak v sistemu izenačili z atmosferskim tlakom (101 kPa). Pri takšnih pogojih je naša naprava generirala kavitacijo. V drugem režimu pa smo ustvarili nadtlak (253 kPa) in s tem preprečili nastanek kavitacije, kljub temu, da so bili ostali obratovalni pogoji identični (vrtilna frekvenca rotorja, pretok skozi napravo, temperatura). Prisotnost in agresivnost kavitacije smo merili z računalniško podprto vizualizacijo s hitro kamero in zajemom pulzacij dinamičnega tlaka s hidrofonom. Količino neraztopljenega detergenta smo določevali s preciznim tehtanjem filtra, preko katerega smo pretočili raztopino. Razlika v masi filtra pred in po eksperimentu predstavlja količino neraztopljenega detergenta. Izvedli smo 24 eksperimentov, pri nespremenjeni vrtilni frekvenci rotorja 7000 vrtljajev na minuto in pri petih različnih časih obratovanja.

Rezultati kažejo na to, da lahko z uporabo kavitacije občutno izboljšamo priprav pralne raztopine. Pri obratovanju generatorja kavitacije v kavitacijskem režimu se je več kot 80 % detergenta raztopilo v pičlih 10 sekundah. Enaka količina detergenta se je v režimu brez kavitacije raztopila šele po 150 sekundah. Izboljšanje procesa gre pripisati mehanskim efektom ob implozijah kavitacijskih mehurčkov in izboljšanem mešanju. Na diagramu tlačnih pulzacij je razvidno, da so tlačne amplitude v kavitacijskem režimu za faktor 2 večje, v primerjavi z amplitudami v ne-kavitacijskem režimu. Posledično se ob generaciji kavitacije znotraj komore močno poveča stopnja turbulence in interakcija med detergentom in vodo. Učinkovitost raztapljanja se za oba obratovalna režima eksponentno zmanjšuje s časom. Do tega pride, ker se verjetnost interakcije med topljencem in topilom postopoma zmanjšuje.

Predstavljena raziskava prikazuje, kako lahko učinkovito skrajšamo čas pralnih programov z izrabo kavitacije. Ob enem avtorji predvidevajo, da vgradnja podobne naprave v pralni stroj ne bi povečala porabe energije, saj se izgube pri generaciji kavitacije pojavljajo v obliki toplote. V primeru pralnih strojev pa je ta toplota v osnovi koristna energija, saj razbremenjuje električne grelce.

Načrtovane so tudi dodatne raziskave za možnosti uporabe takšne naprave v pralnih strojih. Tehnologija pranja tekstila se nenehno izboljšuje, področja uporabe kavitacije pa se hitro širijo. Raziskovalci že iščejo možnosti izrabe kavitacije za čiščenje tekstila, dezinfekcijo, odstranjevanje in preprečevanje nastanka vodnega kamna.

Ključne besede: hidrodinamska kavitacija, rotacijski generator kavitacije, agresivnost kavitacije, pralni stroj, raztapljanje

*Naslov avtorja za dopisovanje: Univerza v Ljubljani, Fakulteta za strojništvo, Aškerčeva 6, 1000 Ljubljana, Slovenija, tadej.stepisnik@fs.uni-lj.si

Strojniški vestnik - Journal of Mechanical Engineering 63(2017)2, SI 14

Prejeto v recenzijo: 2016-03-10
Prejeto popravljeno: 2016-11-21
Odobreno za objavo: 2016-12-16

Vpliv hrapavosti notranje površine šobe na delovanje samoresonančnih kavitacijskih vodnih curkov pri različnih tlakih okolice

Deng Li[1,2,3] – Yong Kang[1,2,*] – Xiaolong Ding[1,2] – Xiaochuan Wang[1,2] – Zhenlong Fang[1,2]

[1] Univerza Wuhan, Šola za energetiko in strojništvo, Kitajska
[2] Univerza Wuhan, Državni laboratorij Hubei za teorijo in nove tehnologije vodnega curka, Kitajska
[3] Illinoiška univerza v Urbani-Champaignu, Oddelek za mehaniko in inženiring, Združene države

Samoresonančni kavitacijski vodni curek (SRCW) z velikimi koherentnimi strukturami in vrtinčnimi obroči v strižni plasti je z ozirom na udarni tlak in kavitacijsko sposobnost bistveno boljši od konvencionalnega kavitacijskega vodnega curka. Danes je razširjen v raznih praktičnih in industrijskih aplikacijah, še posebej pri vrtanju globokih lukenj, kjer je tlak okolice razmeroma visok. Velja, da je začetno kavitacijsko število pri SRCW v splošnem od dva- do šestkrat večje kot pri konvencionalnem kavitacijskem vodnem curku.

Večina dosedanjih raziskav SRCW je bila usmerjenih v mehanizme oblikovanja curka in aplikacije, le malo pozornosti pa je bilo posvečene vplivu hrapavosti notranje površine šobe. Pričakovano je, da hrapavost notranje površine šobe vpliva na pojav kavitacije in s tem na delovanje SRCW.

Za dodatno izboljšanje delovanja SRCW pri tlaku okolice je bil eksperimentalno preučen vpliv hrapavosti notranje površine šobe tako, da je curek deloval na vzorce iz čistega aluminija (1070A) pri različnih razdaljah šobe in tlakih okolice. Tipični makroskopski videz in izguba mase obdelanih preizkušancev sta bila uporabljena za vrednotenje delovanja curkov iz šestih orgelskih šob z različnimi vrednostmi hrapavosti notranje površine (0,8 μm, 1,6 μm, 3,2 μm, 6,3 μm, 12,5 μm in 25 μm).

Rezultati kažejo, da hrapavost notranje površine šobe pomembno vpliva na optimalno razdaljo šobe in na intenziteto kavitacije. Vpliv je močno odvisen od tlaka okolice, iz česar tudi sledi, da je z ustreznim tlakom okolice mogoče izboljšati kavitacijsko sposobnost SRCW. Videti je, da ta lastnost ni odvisna od notranje hrapavosti šobe. Ugotovljeno je bilo tudi, da pri vsakem tlaku okolice obstaja optimalna hrapavost površine, pri kateri se občutno izboljša kavitacijska erozijska sposobnost. Natančneje, pri tlaku okolice 2 MPa oz. 4 MPa povzroči površinska hrapavost 6,3 μm največjo intenziteto kavitacije pri oddaljenosti šobe 42 oz. 50 mm. Pri tlakih okolice 6 MPa, 8 MPa in 10 MPa je vrednost površinske hrapavosti 12,5 μm tista, pri kateri se intenziteta najbolj poveča pri oddaljenosti šobe 45 mm, 40 mm in 35 mm.

Iz rezultatov eksperimentov med drugim sledi, da povečana intenziteta kavitacije izboljša udarno moč visokohitrostnega vodnega curka. Na podlagi Reynoldsovega števila je bila izračunana debelina viskozne podplasti v komori šobe in na izhodu za različne pogoje. Opravljena je bila tudi preliminarna analiza vpliva hrapavosti notranje površine šobe v smislu primerjave debeline viskozne podplasti in srednje višine elementov hrapavosti.

Predstavljena študija podaja smernice za določanje potrebne kakovosti obdelave notranje površine orgelskih šob. Žal je trenutno na voljo le malo literature o vplivih hrapavosti notranje površine šob na delovanje SRCW in zato bi bile nujne dodatne teoretične in matematične raziskave.

Ključne besede: samoresonančni kavitacijski vodni curek, površinska hrapavost, debelina viskoznega podsloja, kavitacijska erozija, izguba mase, tlak okolice, orgelska šoba

*Naslov avtorja za dopisovanje:: Univerza Wuhan, Šola za energetiko in strojništvo, Wuhan, Kitajska, kangyong@whu.edu.cn

Strojniški vestnik - Journal of Mechanical Engineering 63(2017)2, SI 15

Prejeto v recenzijo: 2016-06-15
Prejeto popravljeno: 2016-11-21
Odobreno za objavo: 2016-11-29

Inverzna metoda za vodenje strjevanja čistega materiala v sferični geometriji

Mohamed Charifi* – Rabah Zegadi
Univerza v Setifu, Inštitut za optiko in finomehaniko, Alžirija

Namen predstavljene študije je vodenje procesa strjevanja čistega materiala, popisanega z enodimenzijsko sferično geometrijo. Glavni dejavniki, upoštevani pri določanju strukture in lastnosti končnega stanja, so kinetika spremembe stanja, geometrija stika med fazami in njen razvoj.

Vodenje stika trdne in tekoče faze v procesu strjevanja je bilo simulirano po inverzni metodi v enodimenzijski sferični geometriji z ravninsko fronto. Kontrolna spremenljivka je bila temperatura na fiksni meji trdne domene. Znani podatki so začetno stanje, želeni razvoj ravninske fronte in temperatura fazne spremembe. Inverzni problem je mogoče razrešiti z dodatnimi informacijami o toplotnem toku na fronti, izpeljanem iz toplotne bilance. Vodilne enačbe toplotnega sistema popisujejo prevod toplote.

Za razrešitev problema je bila uporabljena inverzna metoda globalnega spusta, pri čemer sta bili gradientna in adjungirana enačba konstruirani s spremenljivkami, zveznimi v prostoru in času. Za karakterizacijo razlike med dinamičnim vedenjem sistema in razvitim matematičnim modelom je bil vpeljan kriterij najmanjših kvadratov. Nato je bila pridobljena adjungirana enačba za točno ocenitev kriterijskega gradienta. Optimalna rešitev je bila poiskana z iterativnim algoritmom na osnovi konjugiranega gradienta. Enačbe so bila formulirane po postopku za iskanje kriterijskega gradienta z ustrezno adjungirano enačbo. Za numerično reševanje je bila uporabljena klasična metoda končnih razlik s premično mrežo, povezano z obravnavano fizično domeno. Časovna spremenljivka je bila nato diskretizirana po brezpogojno stabilni shemi Crank-Nicolson. Zanesljivost algoritma je bila zagotovljena s posebno točno rešitvijo. Predstavljeni rezultati pokrivajo točno zgrajeno rešitev in točne podatke s šumom. Za dobro definicijo problema in stabilno rešitev za primer podatkov s šumom je bila uporabljena metoda regularizacije po Tikhonovu.

Za primer točnih podatkov brez šuma je bil uporabljen optimizacijski algoritem za določitev optimalnega vodenja, ki zagotavlja želeni razvoj fronte z utežno funkcijo in brez nje. Utežna funkcija vpliva na računski čas in na število iteracij. Izboljšani rezultati za obravnavani interval toplotnega procesa so odvisni od začetne ocene in upoštevanja zakonov prenosa toplote. Po nekaj iteracijah sta bila z visoko natančnostjo zagotovljena vodenje in toplotni tok na fiksni meji za 95 % časovnega horizonta. V preostalem času pa se pojavijo večje napake, kot je tudi pričakovano pri tovrstnih globalnih optimizacijskih metodah.

Za točne podatke s šumom je bil podatkom dodan beli šum s 5-odstotno največjo amplitudo, kar dobro ustreza realnemu stanju. Dodani šum je povzročil občutna nihanja rezultatov. Relativna napaka je bila približno 20 %. Napake so povezane s slabo definiranim inverznim problemom.

Da bi izboljšali rezultate pri dodanem belem šumu, je bila uporabljena priporočena metoda regularizacije po Tikhonovu. Pri tej metodi se doda kazenski člen, ki ohranja funkcijo U(t) v funkcijskem podprostoru in nadzoruje njeno stopnjo spreminjanja. Ta metoda izboljša točnost vodenja, ko so podatki obremenjeni s šumom. Amplitude nihanj pri regulariziranem problemu so bile občutno manjše, vodenje in toplotni tok sta se s časom stabilizirala.

Čeprav rezultati v tem članku oblikujejo koherentno celoto, bi si bilo treba v nadaljnjih raziskavah pobližje ogledati še nekatere druge vidike:

- Strjevanje čistega materiala v dvo- in tridimenzionalni geometriji.
- Uporaba eksperimentalnih podatkov za validacijo algoritma.
- Preučitev strjevanja zlitin.
- Upoštevanje konvekcije pri reševanju problema strjevanja.

Predstavljeni pristop omogoča vodenje strjevanja čistega materiala v enodimenzijski sferični geometriji. Simulacija vodenja v takšni geometriji po inverzni metodi je razmeroma novo raziskovalno področje.

Ključne besede: fazna sprememba, stik med trdno/tekočo fazo, inverzni problem, sferična geometrija

*Naslov avtorja za dopisovanje: Univerza v Setifu, Inštitut za optiko in finomehaniko, 19000 Sétif, Alžirija, charifi_mohamed@yahoo.fr

Strojniški vestnik - Journal of Mechanical Engineering 63(2017)2, SI 16

Prejeto v recenzijo: 2016-03-17
Prejeto popravljeno: 2016-08-15
Odobreno za objavo: 2016-12-16

Študija utrjanja pri osno nesimetričnem rotacijskem preoblikovanju brez trna

Zhen Jia[1] – Zhiren Han[1,*] – Baoming Liu[1] – Yong Xiao[2]

[1] Univerza za letalske in vesoljske tehnologije v Shenyangu, Državni laboratorij za temeljne znanosti in digitalne proizvodne procese v letalski industriji, Kitajska
[2] Severozahodna politehnična univerza, Šola za strojništvo, Kitajska

Osno nesimetrične lupine se pogosto uporabljajo v letalski, vesoljski in avtomobilski industriji. Rotacijsko preoblikovanje brez trna je primerno za izdelavo tovrstnih delov zaradi dobre fleksibilnosti, kratke priprave proizvodnje in nizkih stroškov.

Polje sil med procesom pa je drugačno kot pri preoblikovanju s trnom, saj surovec ni podprt. Posebna osno nesimetrična oblika povzroči značilno porazdelitev utrjanja pri rotacijskem preoblikovanju brez trna, s tem pa vpliva na lastnosti stožčastih delov. V eksperimentih rotacijskega preoblikovanja so bili uporabljeni trije različni nabori delovnih pogojev za različna polovična kota stožca HCA (45–30°, 60–30° in 60–45°).

Preizkusi površinske hrapavosti obdelovancev so pokazali, da je manjši kot polovičnega stožca HCA povezan z večjo stopnjo preoblikovalnega utrjanja. Za razkrivanje omenjenih odvisnosti so bile uporabljene preiskave mikrostrukture in teoretična analiza. Po izločitvi možnosti uporabe metalografskih metod je bila za študijo preoblikovalnega utrjanja osno nesimetričnega dela izbrana analiza napetostno-deformacijskega stanja. Porazdelitev preoblikovalnega utrjanja je bila preučena eksperimentalno in po metodi končnih elementov (MKE). Na podlagi izpeljane poti valja je bil oblikovan model po MKE za osno nesimetrično rotacijsko preoblikovanje brez trna.

Ugotovljeno je bilo dobro ujemanje med morfologijo in porazdelitvijo debeline sten, določeno s simulacijo in eksperimentalno. Določeno in analizirano je bilo ekvivalentno deformacijsko polje v obdelovancu po 24, 48 in 74 sekundah obdelave. Deformacije med procesom so enakomerne, stopnja neenakomernosti pa se povečuje s trajanjem procesa. Manjši kot polovičnega stožca je povezan z večjo stopnjo preoblikovalnega utrjanja zato, ker valj pri manjšem kotu HCA povzroča bolj nehomogene plastične deformacije. Neenakomernost plastičnih deformacij neposredno vpliva na orientacijo gibanja dislokacij ter spodbuja oblikovanje deformacijskega pasu, ki končno privede do preoblikovalnega utrjanja materiala. Le-to je zato večje na mestih z manjšim kotom HCA. V delovnem položaju z največjo razliko v kotih HCA je bila ugotovljena tudi največja razlika v preoblikovalnem utrjanju, največja razlika v trdoti pa lahko znaša 15 %. Trenutna natančnost modela po MKE je majhna in bi jo bilo treba izboljšati. Razlika v debelini sten, določeni s simulacijo in eksperimentom, bo še dodatno zmanjšana z visokonatančnimi simulacijami.

V prihodnje bo tako možna širša uporaba MKE za analizo in reševanje problemov toka kovine pri osno nesimetričnem rotacijskem preoblikovanju brez trna. Visokonatančne simulacije po MKE lahko npr. v veliki meri olajšajo preiskave mehanizma oblikovanja prirobničnih zgibov in njegovega vpliva na omejitve globine aksialnega preoblikovanja.

Članek najprej podaja študijo utrjanja pri osno nesimetričnem rotacijskem preoblikovanju brez trna. Analizirane so lastnosti porazdelitve in mehanizmi površinskega utrjanja pri različnih kotih HCA. Študija dopolnjuje osnovno teorijo tega postopka preoblikovanja in zagotavlja teoretično osnovo za izkoriščanje (npr. za povečanje trdnosti delov) ali za zmanjšanje (npr. za ohranitev plastičnosti kovine) pojava utrjanja.

Ključne besede: osno nesimetrično rotacijsko preoblikovanje, stanje preoblikovalnega utrjanja, rotacijsko preoblikovanje brez trna, HCA, MKE, napetosti

*Naslov avtorja: Univerza za letalske in vesoljske tehnol. v Shenyangu, 38 Daoyi South Avenue, Daoyi Developentt. District, Shenyang, Kitajska, Hanren888@163.com

Strojniški vestnik - Journal of Mechanical Engineering 63(2017)2, SI 17

Prejeto v recenzijo: 2016-08-30
Prejeto popravljeno: 2016-10-20
Odobreno za objavo: 2016-11-22

Vedenje MHD-mejne plasti nanofluida nad premikajočo se površino pod vplivom konvektivnih robnih pogojev

Mohamed Abdel-wahed[1,*] – Tarek Emam[2,3]

[1] Univerza v Benhi, Oddelek za temeljne znanosti, Tehniška fakulteta, Egipt
[2] Univerza Ain Shams, Znanstvena fakulteta, Oddelek za matematiko, Egipt
[3] Univerza v Dždedi, Znanstveno-umetnostna fakulteta Khulais, Oddelek za matematiko, Saudova Arabija

Članek predstavlja analizo hidromagnetne mejne plasti nad premikajočo se ravno površino v konvektivnih robnih pogojih ob upoštevanju Brownovega gibanja in termoforeze nanodelcev. Privzeto je, da je mejna plast izpostavljena nelinearnemu Rosselandovemu toplotnemu sevanju. Problem je pomemben pri modeliranju v različnih tehniških panogah, npr. pri hladilnih površinah, proizvodnji papirja, pihanju stekla, ekstrudiranju plastike in vlečenju žice.

Problem, ki je modeliran s sistemom parcialnih diferencialnih enačb za ohranitev zveznosti, gibalne količine in energije, je bil s tehniko podobnostne transformacije pretvorjen v sistem navadnih diferencialnih enačb. Sistem je bil nato numerično razrešen s kombinacijo metode streljanja in metode Runge-Kutta četrtega reda.

Izrisane in podrobno preučene so hitrost, temperatura in koncentracija nanodelcev v mejni plasti. Izpeljani in podobno obrazloženi so trenje na površini ter toplotni in masni tok.

Iz rezultatov je jasno razviden vpliv nelinearnega Rosselandovega toplotnega sevanja na toplotno stanje in koncentracijo v mejni plasti. Površinske strižne napetosti pri konveksni zunanji obliki ($n<1$) so večje kot pri konkavni zunanji obliki ($n>1$), prisotnost konvektivnih pogojev pa zmanjšuje tako površinski toplotni tok kakor tudi masni tok.

Rezultati potrjujejo neposreden in jasen vpliv oblike površine in konvektivnih robnih pogojev na vedenje mejne plasti, enako pa velja tudi za mehanske lastnosti.

Ključne besede: nanofluidi, MHD tok, konvektivni pogoji, nelinearno toplotno sevanje

*Naslov avtorja za dopisovanje: Univerza v Benhi, Cairo, Egypt, eng_moh_sayed@live.com

Strojniški vestnik - Journal of Mechanical Engineering 63(2017)2, SI 18

Prejeto v recenzijo: 2016-05-08
Prejeto popravljeno: 2016-07-29
Odobreno za objavo: 2016-12-05

Izboljšanje udobja pri uporabi novega sistema nelinearnega vzmetenja sedežev na podlagi terenskih meritev

Leilei Zhao – Changcheng Zhou* – Yuewei Yu
Tehniška univerza v Shandongu, Šola za transport in avtomobilsko tehniko, Kitajska

Cilj predstavljene študije je izboljšanje udobja pri vožnji z novim sistemom nelinearnega vzmetenja sedežev na podlagi terenskih meritev. Analiziran je bil nov voznikov sedež, razvit za uporabo v težkih tovornjakih. Vzmetenje je zasnovano kot običajen škarjasti sistem, vanj pa sta vgrajena votla gumijasta vzmet in hidravlični blažilnik. Elementa sta pritrjena na školjko in na ogrodje sedeža med škarjasto konstrukcijo. Gumijasta vzmet deluje kot elastičen element z visokonelinearno karakteristiko, ki omogoča prilagajanje različnim delovnim pogojem, asimetričen blažilnik pa zagotavlja asimetrično karakteristiko dušenja. Obstoječi modeli sedežev niso bili primerni za ta sistem, zato je bil za boljši opis razvit nov nelinearen matematični model.

Točni vhodni signali za identifikacijo parametrov so bili pridobljeni s terenskimi meritvami. Za testni objekt je bil izbran tovornjak z novim sedežem, na ogrodje katerega je bil pritrjen pospeškomer. Podatki o pospeških so bili nato zajeti pri do konca naloženem tovornjaku na cesti za motorna vozila pri hitrostih 65 km/h, 75 km/h in 85 km/h ter na makadamu pri hitrostih 40 km/h, 50 km/h in 60 km/h. Tako cesta za motorna vozila kot makadamska cesta sta bili razmeroma ravni, vozišče pa je bilo zelo suho. Dolžina vzorcev je bila vsakokrat 40 s, frekvenca vzorčenja pa 200 Hz. Na podlagi terenskih meritev so bili nato identificirani parametri modela. Da bi preverili pravilnost identificiranih parametrov, je bila nato opravljena analiza sile stiskanja gumijaste vzmeti po metodi končnih elementov. Za simulacijo mehanskih lastnosti gumijaste vzmeti v programskem paketu ANSYS je bil privzet znani model Moony-Rivlin. Krivulja deformacij, ki je bila izračunana v paketu ANSYS, se dobro ujema z identificirano krivuljo deformacij in potrjuje njeno sprejemljivost. Koeficient linearne togosti vzmeti K_{s1} ima v analizi občutljivosti največji vpliv na po vertikalni frekvenci uteženi RMS-pospešek sedeža, temu pa sledita ekvivalentna koeficienta dušenja C_1 in C_2 pri vračanju vzmeti. Vpliv velikosti Coulombovega trenja F_0 je minimalen. Koeficienta dušenja vzmetenja sta bila uglašena za kar se da udobno vožnjo ob upoštevanju praktičnih omejitev. Rezultati optimizacije kažejo, da oba koeficienta dušenja in razmerje med koeficientoma dušenja pri vračanju pomembno vplivajo na udobje pri vožnji.

Končno je bil opravljen še test na preizkuševališču, kjer se je po uglaševanju koeficientov izkazalo, da so se vrednosti po vertikalni frekvenci uteženega RMS-pospeška sedeža med vožnjo po cesti za motorna vozila in po makadamski cesti zmanjšale za približno 10,0 in 8 %. Testi na preizkuševališču dokazujejo tudi zanesljivost modela sistema sedeža in predlagane metode določanja blaženja. Izbrana koeficienta blaženja sta uporabna v praksi in učinkovita. Novo nelinearno vzmetenje in metoda uglaševanja koeficientov blaženja predstavljata dobro izhodišče za nadaljnje izboljšave udobja pri vožnji in za zaščito voznikovega zdravja.

V prihodnjih študijah bodo raziskani kompleksnejši modeli novega tipa vzmetenja, pripravljene pa bodo tudi simulacije kompletnega vozila s primernim modelom sedeža in človeškega telesa. Opravljeni bodo tudi testi udobja pri vožnji z vozilom pri naključnih in impulznih vhodih po standardu ISO 2631-1:1997.

Ključne besede: kakovost vožnje, stanje cest, nelinearno vzmetenje, uglaševanje koeficientov, terenske meritve, sistem sedeža

*Naslov avtorja za dopisovanje: Tehniška univerza v Shandongu, Šola za transport in avtomobilsko tehniko, Kitajska, greatwall@sdut.edu.cn

Strojniški vestnik - Journal of Mechanical Engineering 63(2017)2, SI 19

Prejeto v recenzijo: 2016-05-30
Prejeto popravljeno: 2016-08-02
Odobreno za objavo: 2016-11-18

Raziskava mehanskih lastnosti epoksi kompozitov s polnilom iz roževine v prahu

Duraisamy Kumar [1,*] – Sadayan Rajendra Boopathy[2] – Dharmalingam Sangeetha[2] – Govindarajan Bharathiraja[1]

[1] Kolidž za inženiring in tehnologijo C. Abdul Hakeem, Oddelek za strojništvo, Indija
[2]Univerza Anna, Tehniški kolidž, Guindy, Oddelek za strojništvo, Indija

Namen raziskave je opredelitev možnosti izkoriščanja bioloških odpadkov pri razvoju biokompozitov zaradi njihove nizke cene, prijaznosti do okolja in biološke razgradljivosti; zmanjšanje onesnaženja okolja, iskanje zamenjave za sintetična vlakna in pocenitev izdelave kompozitov; izdelava biokompozitov iz epoksi smole in odpadne roževine v prahu (HP); kakor tudi optimizacija parametrov procesa izdelave kompozita epoksi/HP.

Cilji raziskave so obdelava delcev HP z NaOH za izboljšanje združljivosti med delci HP in epoksijem, izdelava biokompozitov z delci odpadne HP kot polnilom in epoksijem kot matriksom, izvedba mehanskih in površinskih morfoloških preizkusov na kompozitih HP/epoksi, optimizacija dejavnikov, ki vplivajo na kompozite HP/epoksi, izdelava vzorcev na podlagi optimiziranih parametrov ter preverjanje njihovih lastnosti, in končno analiza lastnosti pripravljenih kompozitov HP/epoksi.

Delci odpadne roževine so bili zmleti in presejani na različne velikosti s pomočjo sit. Delci HP so bili očiščeni z raztopino NaCl, razmaščeni z dietiletrom in obdelani z raztopino NaOH. Kompozitni vzorci so bili izdelani na osnovi Taguchijevega ortogonalnega polja L9 (3×3) (koncentracija NaOH, A_1 = 0,1 N, A_2 = 0,2 N in A_3 = 0,3 N, velikost delcev HP, B_1 = 125 μm, B_2 = 250 μm in B_3 = 425 μm, in volumski delež HP C_1 = 10 %, C_2 = 20 %, C_3 = 30 %) ter z neobdelanim HP in epoksijem. Delci HP in epoksi smola so bili zmešani v ustreznem razmerju, preneseni v orodje ter 30 minut prešani v hidravličnem stroju pri tlaku 0,5 MPa. Stisnjene plošče so se 24 ur utrjevale pri sobni temperaturi in iz kompozitne plošče so bili nato izrezani preizkušanci po standardih ASTM. Lastnosti preizkušancev so bile nato testirane po istih standardih. Z vrstičnim elektronskim mikroskopom so bile narejene mikrografske preiskave preizkušancev po nateznem preizkusu. Optimizacija faktorjev je bila opravljena po metodah GRA in ANOVA. Izvedena je bila primerjava lastnosti optimalnih preizkušancev ter neobdelanih kompozitnih preizkušancev in preizkušancev iz čistega epoksija.

Rezultati raziskav kažejo, da je čista roževina vlaknene konsistence, ima manjšo gostoto in boljše lastnosti kot polimeri. SEM-mikrograf vzorcev po nateznem preizkusu kaže dobro združljivost med delci HP in smolo pri volumskem deležu HP 10 % ter povečano nastajanje gruč z rastjo volumskega deleža HP. Ugotovljeni so bili naslednji optimalni faktorji: največja koncentracija NaOH A_3 (t. j. 0,3 N), najmanjša velikost HP B_1 (t. j. 125 μm) in najmanjši volumski delež HP C_1 (t. j. 10 %). Z alkalno obdelavo postanejo površine HP bolj trde in grobe, poveča pa se tudi moč spajanja. Kompoziti, obdelani z NaOH, imajo boljše lastnosti kot neobdelani kompoziti, optimalna koncentracija NaOH je tako A_3 (t. j. 0,3 N). Za večino mehanskih lastnosti so zaželeni manjši delci, le za udarno trdnost so zaželeni večji delci. Ob upoštevanju vseh lastnosti so optimalni manjši delci (B_1 oz. 125 μm). Z rastjo deleža prahu se povečujejo gruče delcev prahu, to pa privede do površinskih razpok in nezdružljivosti, kar vpliva na lastnosti. Ko je volumski delež HP najmanjši (C_1, 10 %), je torej dosežena dobra združljivost med sestavinami in epoksi smolo za optimalen rezultat. Analiza ANOVA je razkrila prispevek posameznih faktorjev: za volumski delež HP 90,87 %, za velikost HP 6,43 % in za koncentracijo NaOH 0,78 %. Vrednosti R^2 in prilagojene vrednosti R^2 presegajo 95 %, s čimer je potrjena stopnja zaupanja 95 %. Primerjava med optimalnim preizkušancem in neobdelanimi preizkušanci HP je pokazala, da ima optimalni preizkušanec boljše lastnosti. Sledi, da so kompoziti HP/epoksi potencialno uporabni v različnih panogah.

Ta prispevek postavlja nove smernice za raziskave uporabe živalskih odpadkov. Funkcionalni kompoziti z delci HP kot zamenjavo za neobnovljive sestavine lahko občutno zmanjšajo onesnaženje okolja, obenem pa so cenovno ugodni.

Ključne besede: roževina v prahu, epoksi smola, kompoziti z delci, mehanske lastnosti, optimizacija

*Corr. Author's Address: C. Abdul Hakeem College of Engineering and Technology, Melvisharam, Vellore, India, ilayakumard@gmail.com

Na Fakulteti za strojništvo Univerze v Ljubljani sta obranila svojo doktorsko disertacijo:

- dne *5. januarja 2017* **Matevž ZUPANČIČ** z naslovom: »Razvoj bifilnih strukturiranih površin za izboljšan prenos toplote pri vrenju« (mentor: prof. dr. Iztok Golobič);

Mehurčkasto vrenje je najbolj učinkovit in hkrati tehnično obvladljiv mehanizem prenosa toplote. Izboljšati prenos toplote pri vrenju pomeni zmanjšati pregretje vrelne površine pri danem sproščanju gostote toplotnega toka in povečati kritično gostoto toplotnega toka, kar je možno doseči z spremembo mikro- in nanostrukture ter omočljivosti vrelne površine. V disertaciji predstavljamo razvoj dveh tipov površin: bifilnih strukturiranih površin na osnovi premaza iz polidimetilsiloksana in silike ter lasersko strukturiranih hidrofilnih površin. Zasnovan eksperimentalni sistem nam omogoča spremljanje procesa vrenja na tankih kovinskih folijah, kjer s pomočjo hitrotekoče infrardeče kamere merimo nestacionarna temperaturna polja in z video kamero opazujemo rast in gibanje mehurčkov. Pri vrenju na bifilnih površinah smo pokazali, da hidrofobna mesta promovirajo nastop vrenja, velikosti hidrofobnih področji pa vplivajo na velikosti mehurčkov in frekvence nukleacij. Z ustreznim bifilnim vzorcem smo definirali področja aktivnih nukleacijskih mest in zakasnili pojav horizontalnih koalescenc, s čimer smo dosegli boljšo stabilnost vrelnega procesa. Izboljšave se pokažejo tudi v zmanjšanju pregretja ter in povečanju kritične gostote toplotnega toka. Ugotavljamo, da je optimalna razporeditev hidrofobnih mest na bifilnih površinah odvisna od točke obratovanja, torej od gostote toplotnega toka. Pri vrenju na lasersko strukturiranih površinah so bili najboljši rezultati doseženi na heterogeno omočljivi površini s prisotnimi mikro jamicami. Največje število aktivnih nukleacijskih mest sovpada z lokacijami mikro jamic, kar pojasnjujemo tudi s pomočjo obstoječih nukleacijskih kriterijev. Na tem vzorcu je bilo doseženo celo nižje pregretje kot na vseh ostalih bifilnih površinah. V sklopu analize eksperimentalnih podatkov smo s statistično obdelavo nestacionarnih temperaturnih polj določili porazdelitve gostot verjetnosti temperatur na vrelnih površinah. Na podlagi značilnosti teh porazdelitev je možno ovrednotiti stabilnost procesa vrenja, česar nam do sedaj uveljavljene vrelne krivulje niso omogočale. S tem odpiramo novo področje na poti boljšega razumevanja procesa vrenja in razvoja tehnologij za izboljšan prenos toplote;

- dne *6. januarja 2017* **Tine SELJAK** z naslovom: »Uporaba inovativnega lignocelulloznega biogoriva za pogon plinskih turbin« (mentor: prof. dr. Tomaž Katrašnik, somentor: izr. prof. dr. Matjaž Kunaver);

V delu je predstavljena prva celovita analiza uporabe inovativnega lignocelulloznega biogoriva druge generacije za pogon plinskih turbin. Utekočinjen les pridobljen s postopkom solvolize izkazuje za tri velikostne razrede višjo viskoznost kot dizelsko gorivo, dvakrat nižjo kurilno vrednost in dvakrat nižjo stehiometrijsko razmerje, kar predstavlja poseben izziv za uporabo goriva v toplotnih motorjih. Poleg podrobne analize zgorevanja z določitvijo krovnih mehanizmov za nastanek emisij CO, THC, NO_x in PM je v delu vzporedno vrednoten tudi vpliv primarnih in sekundarnih obratovalnih parametrov plinske turbine na zgorevanje ter vpliv inovativnega goriva na materiale ter komponente turbinskega motorja. Široka eksperimentalna matrika razkriva številne soodvisne parametre med vsemi preučevanimi veličinami, ki po poglobljeni analizi podajo omejitve razvojnega prostora za komercialne sisteme za soproizvodnjo toplote in elektrike, ki so osnovani na plinskih turbinah. Med parametrizacijo odzivov so prvič razkriti tudi številni mehanizmi, ki pripomorejo k razumevanju obnašanja inovativnega goriva v širšem spektru energetskih sistemov, razvite pa so tudi posamezne inovativne rešitve na področju vbrizgovalnega sistema in krmilne strategije, ključne za uspešno implementacijo inovativnega goriva v serijskih plinskih turbinah. Smiselnost širše uporabe goriva je podprta z analizo rentabilnosti.

Information for Authors

All manuscripts must be in English. Pages should be numbered sequentially. The manuscript should be composed in accordance with the Article Template given above. The maximum length of contributions is 10 pages. Longer contributions will only be accepted if authors provide juastification in a cover letter. For full instructions see the Information for Authors section on the journal's website: http://en.sv-jme.eu .

SUBMISSION:

Submission to SV-JME is made with the implicit understanding that neither the manuscript nor the essence of its content has been published previously either in whole or in part and that it is not being considered for publication elsewhere. All the listed authors should have agreed on the content and the corresponding (submitting) author is responsible for having ensured that this agreement has been reached. The acceptance of an article is based entirely on its scientific merit, as judged by peer review. Scientific articles comprising simulations only will not be accepted for publication; simulations must be accompanied by experimental results carried out to confirm or deny the accuracy of the simulation. Every manuscript submitted to the SV-JME undergoes a peer-review process.

The authors are kindly invited to submit the paper through our web site: http://ojs.sv-jme.eu. The Author is able to track the submission through the editorial process - as well as participate in the copyediting and proofreading of submissions accepted for publication - by logging in, and using the username and password provided.

SUBMISSION CONTENT:

The typical submission material consists of:

- A **manuscript** (A PDF file, with title, all authors with affiliations, abstract, keywords, highlights, inserted figures and tables and references),
- Supplementary files:
  - a **manuscript** in a WORD file format
  - a **cover letter** (please see instructions for composing the cover letter)
  - a ZIP file containing **figures** in high resolution in one of the graphical formats (please see instructions for preparing the figure files)
  - possible **appendicies** (optional), cover materials, video materials, etc.

Incomplete or improperly prepared submissions will be rejected with explanatory comments provided. In this case we will kindly ask the authors to carefully read the Information for Authors and to resubmit their manuscripts taking into consideration our comments.

COVER LETTER INSTRUCTIONS:

Please add a **cover letter** stating the following information about the submitted paper:

1. Paper **title**, list of **authors** and their **affiliations**.
2. **Type of paper**: original scientific paper (1.01), review scientific paper (1.02) or short scientific paper (1.03).
3. A **declaration** that neither the manuscript nor the essence of its content has been published in whole or in part previously and that it is not being considered for publication elsewhere.
4. State the **value of the paper** or its practical, theoretical and scientific implications. What is new in the paper with respect to the state-of-the-art in the published papers? Do not repeat the content of your abstract for this purpose.
5. We kindly ask you to suggest at least two **reviewers** for your paper and give us their names, their full affiliation and contact information, and their scientific research interest. The suggested reviewers should have at least two relevant references (with an impact factor) to the scientific field concerned; they should not be from the same country as the authors and should have no close connection with the authors.

FORMAT OF THE MANUSCRIPT:

The manuscript should be composed in accordance with the Article Template. The manuscript should be written in the following format:

- A **Title** that adequately describes the content of the manuscript.
- A list of **Authors** and their **affiliations**.
- An **Abstract** that should not exceed 250 words. The Abstract should state the principal objectives and the scope of the investigation, as well as the methodology employed. It should summarize the results and state the principal conclusions.
- 4 to 6 significant **key words** should follow the abstract to aid indexing.
- 4 to 6 **highlights;** a short collection of bullet points that convey the core findings and provide readers with a quick textual overview of the article. These four to six bullet points should describe the essence of the research (e.g. results or conclusions) and highlight what is distinctive about it.
- An **Introduction** that should provide a review of recent literature and sufficient background information to allow the results of the article to be understood and evaluated.
- A **Methods** section detailing the theoretical or experimental methods used.
- An **Experimental section** that should provide details of the experimental set-up and the methods used to obtain the results.
- A **Results** section that should clearly and concisely present the data, using figures and tables where appropriate.
- A **Discussion** section that should describe the relationships and generalizations shown by the results and discuss the significance of the results, making comparisons with previously published work. (It may be appropriate to combine the Results and Discussion sections into a single section to improve clarity.)
- A **Conclusions** section that should present one or more conclusions drawn from the results and subsequent discussion and should not duplicate the Abstract.
- **Acknowledgement** (optional) of collaboration or preparation assistance may be included. Please note the source of funding for the research.
- **Nomenclature** (optional). Papers with many symbols should have a nomenclature that defines all symbols with units, inserted above the references. If one is used, it must contain all the symbols used in the manuscript and the definitions should not be repeated in the text. In all cases, identify the symbols used if they are not widely recognized in the profession. Define acronyms in the text, not in the nomenclature.
- **References** must be cited consecutively in the text using square brackets [1] and collected together in a reference list at the end of the manuscript.
- **Appendix(-icies)** if any.

SPECIAL NOTES

Units: The SI system of units for nomenclature, symbols and abbreviations should be followed closely. Symbols for physical quantities in the text should be written in italics (e.g. *v*, *T*, *n*, etc.). Symbols for units that consist of letters should be in plain text (e.g. ms^{-1}, K, min, mm, etc.). Please also see: http://physics.nist.gov/cuu/pdf/sp811.pdf .

Abbreviations should be spelt out in full on first appearance followed by the abbreviation in parentheses, e.g. variable time geometry (VTG). The meaning of symbols and units belonging to symbols should be explained in each case or cited in a **nomenclature** section at the end of the manuscript before the References.

Figures (figures, graphs, illustrations digital images, photographs) must be cited in consecutive numerical order in the text and referred to in both the text and the captions as Fig. 1, Fig. 2, etc. Figures should be prepared without borders and on white grounding and should be sent separately in their original formats. If a figure is composed of several parts, please mark each part with a), b), c), etc. and provide an explanation for each part in Figure caption. The caption should be self-explanatory. Letters and numbers should be readable (Arial or Times New Roman, min 6 pt with equal sizes and fonts in all figures). Graphics (submitted as supplementary files) may be exported in resolution good enough for printing (min. 300 dpi) in any common format, e.g. TIFF, BMP or JPG, PDF and should be named Fig1.jpg, Fig2.tif, etc. However, graphs and line drawings should be prepared as vector images, e.g. CDR, AI. Multi-curve graphs should have individual curves marked with a symbol or otherwise provide distinguishing differences using, for example, different thicknesses or dashing.

Tables should carry separate titles and must be numbered in consecutive numerical order in the text and referred to in both the text and the captions as Table 1, Table 2, etc. In addition to the physical quantities, such as *t* (in italics), the units [s] (normal text) should be added in square brackets. Tables should not duplicate data found elsewhere in the manuscript. Tables should be prepared using a table editor and not inserted as a graphic.

REFERENCES:

A reference list must be included using the following information as a guide. Only cited text references are to be included. Each reference is to be referred to in the text by a number enclosed in a square bracket (i.e. [3] or [2] to [4] for more references; do not combine more than 3 references, explain each). No reference to the author is necessary.

References must be numbered and ordered according to where they are first mentioned in the paper, not alphabetically. All references must be complete and accurate. Please add DOI code when available. Examples follow.

Journal Papers:

Surname 1, Initials, Surname 2, Initials (year). Title. Journal, volume, number, pages, DOI code.

[1] Hackenschmidt, R., Alber-Laukant, B., Rieg, F. (2010). Simulating nonlinear materials under centrifugal forces by using intelligent cross-linked simulations. *Strojniški vestnik - Journal of Mechanical Engineering,* vol. 57, no. 7-8, p. 531-538, DOI:10.5545/sv-jme.2011.013.

Journal titles should not be abbreviated. Note that journal title is set in italics.

Books:

Surname 1, Initials, Surname 2, Initials (year). Title. Publisher, place of publication.

[2] Groover, M.P. (2007). *Fundamentals of Modern Manufacturing*. John Wiley & Sons, Hoboken.

Note that the title of the book is italicized.

Chapters in Books:

Surname 1, Initials, Surname 2, Initials (year). Chapter title. Editor(s) of book, book title. Publisher, place of publication, pages.

[3] Carbone, G., Ceccarelli, M. (2005). Legged robotic systems. Kordić, V., Lazinica, A., Merdan, M. (Eds.), Cutting Edge Robotics. Pro literatur Verlag, Mammendorf, p. 553-576.

Proceedings Papers:

Surname 1, Initials, Surname 2, Initials (year). Paper title. Proceedings title, pages.

[4] Štefanić, N., Martinčević-Mikić, S., Tošanović, N. (2009). Applied lean system in process industry. *MOTSP Conference Proceedings*, p. 422-427.

Standards:

Standard-Code (year). Title. Organisation. Place.

[5] ISO/DIS 16000-6.2:2002. *Indoor Air – Part 6: Determination of Volatile Organic Compounds in Indoor and Chamber Air by Active Sampling on TENAX TA Sorbent, Thermal Desorption and Gas Chromatography using MSD/FID.* International Organization for Standardization. Geneva.

WWW pages:

Surname, Initials or Company name. Title, from http://address, date of access.

[6] Rockwell Automation. Arena, from *http://www.arenasimulation.com,* accessed on 2009-09-07.

EXTENDED ABSTRACT:

When the paper is accepted for publishing, the authors will be requested to send an **extended abstract** (approx. one A4 page or 3500 to 4000 characters). The instruction for composing the extended abstract are published on-line: http://www.sv-jme.eu/information-for-authors/ .

COPYRIGHT:

Authors submitting a manuscript do so on the understanding that the work has not been published before, is not being considered for publication elsewhere and has been read and approved by all authors. The submission of the manuscript by the authors means that the authors automatically agree to transfer copyright to SV-JME when the manuscript is accepted for publication. All accepted manuscripts must be accompanied by a Copyright Transfer Agreement, which should be sent to the editor. The work should be original work by the authors and not be published elsewhere in any language without the written consent of the publisher. The proof will be sent to the author showing the final layout of the article. Proof correction must be minimal and executed quickly. Thus it is essential that manuscripts are accurate when submitted. Authors can track the status of their accepted articles on http://en.sv-jme.eu/.

PUBLICATION FEE:

Authors will be asked to pay a publication fee for each article prior to the article appearing in the journal. However, this fee only needs to be paid after the article has been accepted for publishing. The fee is 240.00 EUR (for articles with maximum of 6 pages), 300.00 EUR (for articles with maximum of 10 pages), plus 30.00 EUR for each additional page. The additional cost for a color page is 90.00 EUR. These fees do not include tax.

Strojniški vestnik -Journal of Mechanical Engineering
Aškerčeva 6, 1000 Ljubljana, Slovenia,
e-mail: info@sv-jme.eu

9 770039 248001
ISSN 0039-2480

http://www.sv-jme.eu

Contents

Papers